Spatiotemporal Analysis of Metazoan Cell Morphological Dynamics on Micropatterned Substrates

by

John C. Ahn

A dissertation submitted in partial fulfillment of

the requirements for the degree of

Doctor of Philosophy

(Biochemistry)

at the

UNIVERSITY OF WISCONSIN-MADISON

2023

Date of final oral examination: 11/06/2023

The dissertation is approved by the following members of the Final Oral Committee:

Scott M. Coyle, Assistant Professor, Biochemistry
Judith A. Simcox, Assistant Professor, Biochemistry
Jason R. Cantor, Assistant Professor, Biochemistry
Krishanu Saha, Associate Professor, Biomedical Engineering

Abstract

Crucial biological processes in mammalian organisms, ranging from morphogenesis and motility to dysregulated phenomena such as cancer metastasis, demand highly specified cellular morphologies for a wide variety of different functions. Yet, few studies have provided a framework for systematically quantifying the dynamics of cellular morphology, oftentimes resorting to qualitative statements that do not enable easy comparisons between different experimental conditions. My PhD research has yielded such a method for quantitatively assessing morphological dynamics of mammalian cells, as well as insights on how substrate spatial complexity and size can guide characteristic cell shape formation.

Spatial patterns of adhesive substrates can dictate cell motility trajectories. Mammalian cells demonstrate idiosyncratic trajectories when subjected to barbell-shaped micropatterns with thin constrictions. However, the morphologies of these cells over time remained uncharacterized. We subjected 3T3 mouse fibroblast cells to an array of micropatterns, an assay refined in **Appendix A**, and compared their shape dynamics to a panel of triple-negative breast cancer cells in **Chapter 2**. When exposed to a gradient of size, we found that the morphological dynamics of 3T3 cells display trends analogous to the potential energy curve of a molecule, where energy is high at small micropattern sizes, drops off at a minimum point, and rises again at large micropattern sizes. We also found the breast cancer cell panel exhibited a gradient of morphological activity and could be classified using principal component analysis. This fundamental work provides a quantitative framework for comparing dynamics shapes of cells over time and crucial insights on mammalian cell processing of substrate spatial patterns. **Chapter 3** is an

extension of the micropatterning technique in a different application, regarding how the shape of the cell can influence spatiotemporal patterns of the bacterial MinDE system in mammalian cells. Finally, **Chapter 4** summarizes the findings and implications of the work herein and guides the reader towards future directions.

Acknowledgments

I can hardly believe it.

Am I really going to be done? I suppose this musing is premature because there remains the very real possibility of my committee failing me. However, if they end up passing me, fingers crossed, then I'll finally be done with my PhD. I've spent my entire conscious life in school, so the thought of being outside of it evokes a strange mixture of joy and fear. What am I going to do next in life? Or with my life, for that matter. Hopefully I'll figure it out.

Setting existential thoughts aside, approaching the end of the tunnel brings me immense pleasure, and the gratitude I feel towards the people who have helped bring me here is indescribable. But, since I owe them everything, I must give it, at least, my best shot.

First, I'd like to thank the members of my thesis committee for their encouragement and advice for these past three years. Judith Simcox, Jason Cantor, Krishanu Saha, what I would have done without your guidance, I shudder to think. When entertaining the horrifying thought for a second or two, floundering in my project for a couple more years or mastering out come to mind. All of your kind words, patience, and scientific expertise were most appreciated. Many thanks.

To the bedrock of the IPiB community, Kate Ryan, I am eternally grateful. Your compassion and bureaucratic expertise helped me during my lowest moments in my

PhD, correcting my course, setting me along on successful paths, and giving me hope. The program would be nothing without you.

I would like to thank my peers and mentors in lab who inspired me in so many ways. To Sonali, one of the coolest human beings I've ever met in terms of your love for discovery and fierce desire for justice, as well as one of the worst people in terms of responding to texts. To Ryan, whose grandfatherly demeanor made going into lab such a treat. To Bryce, a chill and quietly brilliant scientist who always asked the best questions during lab meeting. To Tyler, a modern day da Vinci whose deft touch brought molecular and mechanical engines to life. To Yu-yu, who possessed an innovative mind that thought of the most creative projects. To Jun, a relentless workhorse who I hope can spend more time with his family one day. To Eden, whose beautiful microscopy images looked like galaxies. To Maggie, whose little freshwater pincushion creatures were such a delight to witness. To Rohith who was always a source of entertaining conversations during the dullest of days. To Cassidy, who I hope benefitted from my mentorship and will take the scientific world by storm someday with, of course, her cat in tow. To Dennis, my classical music Shazam, it was an honor working with you on the micropatterns and a delight hearing Mongolian throat singing during the most unexpected moments. To Tommy, I hope you get a better landlord and finish One Piece one day. To Casey, Nithesh, and Elliott, whose day-to-day conversations in lab I always treasured, despite my antisocial tendencies, which I hope you can forgive.

Thank you to Scott Coyle, my wonderfully ginger mentor. You took me in, in the midst of a swirling global pandemic and fresh off of my departure from my previous lab. Your kindness and infectious excitement towards science were most greatly

appreciated. You're a delightful mentor and professor, and I'm certain when your son has the ability to form complete sentences, he will be eager to say he is proud to call you his father.

Friends! Oh friends. My beautiful, lovely friends. What would I do without you? Jack, Arielle, Leah, David, Sarah, Lloyd, Jing, Nichole, Phenix, Emma, Jaffna, Mira, Cole, Bijan, and Isaiah. And more recently, the dawgs Preston and Ellie. I love you all so dearly. My warmest memories from the past five years are mostly with all of you.

Finally, I thank my family (and basically family). Tony, Soo, Mory, Marc, my closest thing to extended family growing up in Appleton. Thanks for your constant, musical love. My brother Tim and my sister Christie, thanks for the love only siblings can understand. My mom and my dad, thanks for your unwavering support, your prayers, and your unconditional love. Love you all, so, so much.

.

Table of Contents

Contents

Chapter 1: Introduction

Mammalian cells process complex information from extracellular environments

Synthetic biologists often draw comparisons between biological cells and processing units, noting similarities in how they process various inputs to result in directed outputs. To serve a wide diversity of biological functions, the cell must process chemical gradients, biological signals, physical space, light, heat, and countless other sensory inputs. Through complicated decision-making genetic and regulatory networks, these arrays of inputs result in changes in cell life cycle, shape, motility, metabolism, and more.

The extracellular environment surrounding the cell contains a diverse range of molecules. As a form of intercellular communication, cells release signaling molecules that can take the forms of glycoproteins, peptides, growth factors, hormones, and glycans (Hynes & Naba, 2012). Chemical signaling provides several advantages for controlling the strength of signal, including diffusivity of the molecules for specified ranges of distance as well as concentration gradients for cells to respond to according to stratified thresholds (Muller & Schier, 2011), (Nair et al., 2019), (Lakhani & Elston, 2017). Another advantage to signaling molecules is the degree of specificity conferred by a pathway relying on complementary pairing between receptors and their corresponding ligands. Signaling receptors activate specified biological pathways upon binding to their partner ligands, such as growth factors like vascular endothelial growth factor that will result in angiogenesis, the formation of blood vessels (Freed et al.,

2017), (Domanskyi et al., 2022). Pairing provides another degree of control to ensure regulated execution of specific pathways depending on the biological timing and context. In addition to membrane-bound receptors designed for specific ligands, many membrane-bound protein channels enable the entry of other molecules or ions. For example, GABA, a major neurotransmitter receptor, is responsible for conducting chloride ions to polarize the cell membrane and inhibit the depolarization of neurons (S. Li et al., 2014). Potassium channels are another example, located in cell membranes and acting as gatekeepers for the efflux and influx of K^+ ions from and into cells, which is crucial for regulating electrical voltage across the membrane for processes as varied as proliferation, regulating osmotic flow, hormone secretion, and more (Miller, 2000).

Although signaling molecules and ions make up a substantial portion of the sensory input for cell decision making processes, many other sensory inputs play vital roles. Temperature sensors such as the temperature-activated TRP channels directly convert temperature shifts into gate channel conformation changes (Sánchez-Moreno et al., 2018). Channelrhoopsin-2, isolated from green algae *Chlamydomonas reinhardtii*, was demonstrated to modulate polarization of cells in response to light (Hoffmann et al., 2018). Mechanical forces such as shear stress can act as stimuli for cells such as endothelial cells, affecting functions such as migration, apoptosis, permeability, and proliferation (Y. S. J. Li et al., 2005). While a vast body of research has explored chemical signaling, more recent efforts have been taken to understand how mammalian cells process their physical environment.

Cell morphology is influenced by cues from their physical environment

One of the cell's many potential outputs is its shape, a vast parameter space of physical contortions frequently sampled to serve specified biological functions such as morphogenesis, directed motility, and, with dysregulation of homeostatic processes, even metastasis (Vardhan et al., 2013). A complex coordination between substrate, cell-matrix contacts, and the cytoskeleton is required in order for the cell to determine its overall orientation, polarity, and potential direction of movement.

Cell adhesion to the extracellular matrix (ECM), comprised of networks of sugars and proteins, is mediated through focal adhesions (FAs), the outer cell membrane protein complexes connecting the extracellular matrix to the cytoskeleton(Legerstee & Houtsmuller, 2021). The cytoskeleton, a network of protein fibers, provides physical structure and organization to the cell, as well as scaffolding for intracellular transport. FAs are macromolecular multiprotein assemblies comprised of roughly 150 different proteins located at the distal ends of actin fiber bundles facilitating dynamic interactions between the actin cytoskeleton and the ECM (Zaidel-bar et al., 2007),(Burridge et al., 2016).

Oftentimes, FAs act in concert with structured protrusions from the cell, including lamellipodia and filopodia, extending micron-scale distances from the cell out into the surrounding environment to survey environmental cues or participate in cell migration. Lamellipodia, veil-shaped cell protrusions driven by Arp2/3 complex nucleation of highly branched actin filament networks, form along wide swaths of the leading edge of migrating cells, usually extending 1-5um out into the ECM(Innocenti, 2018). Through integrin receptors in nascent FAs, they engage with the underlying matrix, as well as

providing information about the substrate, such as ECM composition or substrate stiffness (Innocenti, 2018). The maturation of these nascent FAs into mature FAs results in the creation of molecular clutches that couple force generated from actin filament rearward movement with the cell membrane to push forward the leading edge of the cell (Vallotton et al., 2005). Filopodia are another commonly observed structure that provides for protruded contacts in areas surrounding the main bulk of the cell. In contrast to lamellipodia, filopodia are thin, finger-like protrusions with a range of 60-200nm in diameter filled with tight parallel bundles of filamentous actin and an extension range spanning from a few microns long to even hundreds (Gallop, 2020). Some cell types, such as neuronal growth cones or dendritic cells, express filopodia almost exclusively due to their ability to rapidly promote neuronal arborization and the connection between synapses (Gallop, 2020; Mejillano et al., 2004).

These protrusions and their associated FAs possess the ability to sense crucial information in the surrounding environment. For example, macrophages deploy multiple filopodia at a time to sample nearby spaces, and upon making physical contact with antigens present on foreign pathogens, the filopodia bind to the prey and retract it towards the cell body for phagocytosis (Niedergang & Chavrier, 2004). Filopodia in neuronal cells have been observed to detect chemical gradients and subsequently orient the neurite towards the chemoattractants for eventual synapse connections (Gallo & Letourneau, 2004). Lamellipodia are largely responsible for mechanosensation, the detection of substrate stiffness, with implications for spreading, differentiation, migration, proliferation. Computational modeling suggests the bonds between integrin, an integral component of FAs, and fibronectin, a common component of ECM, exhibit catch-bond

biophysical properties, meaning the lifetime of the bonds increase as a function of load (Oakes et al., 2018). Traditional studies have implicated the interplay between the physical stresses caused by tension built between the matrix-cytoskeleton interface that causes changes in the kinetics of composition of proteins within the FA to serve as a sensor for substrate stiffness (Hu et al., 2007). Assessing substrate stiffness of the surrounding environment through these extensions aids the cell in important biological decision making processes.

Substrate stiffness has been implicated in a wide array of crucial biological processes including development, inflammation, wound contraction, tissue maintenance, angiogenesis, and development (Bischofs & Schwarz, 2003). Facilitating these processes requires navigating a complex 3D environment within the body, which presents a number of challenges for the cell, such as polarizations and directional motility towards specific sites. However, due to the wide landscape of tissues, organs, and extracellular spaces throughout the body, there are plenty of varied sensory cues, including substrate stiffness, unique to different kinds of environments to drawn from that cells can take advantage of to elicit processes tailored for the appropriate biological process. Tissues within the human body are composed of ECMs and cells that have well-characterized elastic moduli that span a wide range, with the higher numbers reported for cartilage and bone, >10,000 Pa for muscle and roughly 100 Pa for soft tissues such as fat or brain tissue (Levental et al., 2007). During inflammation, cells must orient themselves and travel towards the wound site, which requires the ability to polarize the nucleus and cytoskeleton. It has been reported that fibroblasts tend to locomote in favor of ECMs with high tensile strain and larger rigidity, which is thought to

represent in vivo environments where the wound site tends to have substrate with higher substrate stiffness (Solon et al., 2007),(Evans et al., 2013).

Locomotion requires reorganization of the cell cytoskeleton, as well as polarization of the nucleus and various other organelles present within the cell, which is an example of how certain biological functions dictate specified cell morphologies. However, it has also been extensively observed that cell morphology itself can largely influence biological functions, showing the bidirectional relationship between shape and function.

Cell morphology plays a large role in various biological processes

A growing body of evidence suggests that the shape of the cell can influence and dictate the outcomes of different biological processes including differentiation, genetic expression, proliferation, and apoptosis. These phenomena demonstrate the importance of considering how the outside environment may shape the fate of the cell through the manipulation of the physical shape of the cell, illustrating the importance of observing cell shape morphology as an area of significant study. These studies hold implications for human health and understanding of fundamental biological processes.

Gene expression profiles of cells have been shown to be altered depending on geometrical constraints of the substrate. One particular study varied the size, shape, and aspect ratio of micropatterned fibronectin substrates to modulate cellular geometry of 3T3 mouse fibroblast cells. Rectangular aspect ratios ranging from 1:1 to 1:5, circles, triangles, and squares with surface areas ranging from 500-2,000um^2, comparable to

the roughly 1,300 um^2 average physiological spreading area of 3T3 cells (N. Jain et al., 2013). Cells largely adopted the shape of the underlying micropatterns, demonstrating micropatterning as an effective technique for modulating cell morphology. Whole genome transcriptome analysis using microarray was performed on cells grown on these different geometries. Different sizes appeared to differentially regulate genes to a greater extent than different types of shapes with roughly equal area, with >250 genes shifting expression when exposed to different sized micropatterns compared to the ~70-150 genes changing expression due to different cell shapes. The main groups of genes changing expression levels were involved with regulating apoptosis, cell division, cell migration, and cell-substrate adhesion (N. Jain et al., 2013).

Regulation of cell life cycle stages, including proliferation and apoptosis, has also been shown to be influenced by cell shape. Using a micropatterning approach, researchers confined MC3T3-E1 osteoblastic cells into rectangle, circle, square, and triangle shapes, resulting in shifted cell proliferation rates due to the downregulation of IP3R1 and SERVA2 calcium cycling proteins(Tong et al., 2017). It has been noted in *Xenopus* development studies that the cell shape of cells within the egg largely guides the orientation of the mitotic spindle, and the subsequent direction of division (Théry & Bornens, 2006). In order to progressively restrict cell extension, human and bovine capillary endothelial cells were subjected to decreasing sizes of matrix-coated adhesive islands, ranging from 5 to 50um, which induced the switch from growth modes to apoptosis (Chen et al., 1997). Regardless of the matrix protein type or antibody to integrin used as the substrate for their adhesion islands, size was the dominating determinant factor for whether the cells would grow or undergo apoptosis.

Cell shape also influences differentiation of stem cells and can even bias the stochastic fate decisions of daughter cells even after rounding of the progenitor cells during mitosis, suggesting that the memory of cell shape can have impacts for future generations of cells from an ancestor. Somatic epidermal stem cells, specifically neonatal human keratinocytes, were subjected to either large (1,024 um^2) or small ($300um^2$) square microprinted fibronectin islands (Totaro et al., 2017). Using a marker for terminal differentiation, expression of involucrin, the number of involucrin-positive cells were substantially increased on the small islands, whereas on the large islands, cells were mostly shielded from differentiation. To probe the molecular mechanism behind this phenomenon, researchers subjected cells spread on large islands to short interfering RNAs (siRNAs) targeting YAP/TAZ. As a result, these spread cells were depleted of YAP/TAZ and differentiated en-masse, suggesting these proteins were involved as biomechanical intermediaries between substrate size detection and cell differentiation.

In order to test memory effects of cell shape on daughter cells, researchers injected V2 neural progenitor cells into a developing zebrafish nervous system and observed the progenitor cells and their respective daughter cells over time (Akanuma et al., 2016). Depending on the degree of elongation and the orientation of the progenitor cell, the fate of the daughter cells change due to the formation of intracellular spatially localized concentrations of upstream signaling proteins such as the Delta family of proteins from the Delta-Notch signaling mediated lateral inhibition system (Akanuma et al., 2016). Due to the substantial effect of cell morphologies on such a vast array of biological processes, many studies have investigated the biomechanical mechanisms

through which physical alterations of cell shape could impact regulation of gene expression.

Traditionally, the cytoskeleton, along with focal adhesion proteins such as vinculin, zyxin, filamin A, and talin, have been implicated as mediators between integrin and actin filaments for mechanosensitive gene regulation (Riveline et al., 2001). Zyxin and paxillin travel between the nucleus and the cytoplasm depending on actomyosin contractility, serving as transcriptional regulators of gene expression(Yuan Wang & Gilmore, 2003). Rho activity has been observed to increase in rounded cell phenotypes, attributed to the inhibition of p190RhoGAP upon binding to filamin A and the reduction of GTPase activation. On the other hand, spread cells cleave filaminA binding from p190RhoGAP, resulting in the inactivation of Rho (Mammoto et al., 2007). Transcriptional attenuation was observed when skin stem cells were subjected to stretching forces, leading to the redistribution of emerin to the outer nuclear membrane and the detachment of heterochromatin from the nuclear lamina and resulting reduction of nuclear actin(Le et al., 2016). Although substantial numbers of molecular agents have been identified as mediators in the ECM-focal adhesion-nucleus interface, an additional element of the spatial reorganization of the nucleus itself during morphological rearrangement of the entire cell has also been observed to play a role in changes of gene expression.

It has been observed that the modulation of gene expression via shape changes appears to be substantially facilitated through to the mechanosensitive reorganization of the nucleus. During processes, such as cell migration, the shape changes required for different functions result in physical forces applied to the nucleus, forcing it into different

configurations. As a result of these different mechanical stresses, the inner contents of the nucleus are rearranged, resulting in differential expression. For example, in fibroblasts, as they flatten and extend, forming focal adhesions to attach to the ECM to survey their surrounding environment, the nucleus is flattened during the process as well (N. Jain et al., 2013; Q. Li et al., 2014). Conversely, with fewer matrix attachments, the sphericity of the nucleus increases.

The consequences are significant, especially when taking into consideration the importance of how the spatial dimension of DNA packing into nonrandom 3D chromosome territories has been shown to a critical intermediate for genome regulatory processes (Lanctôt et al., 2007). The co-expression of clustered genes has been suggested to be reliant on the spatial positionings of chromosomes relative to each other (Bickmore & Van Steensel, 2013). The nuclear lamina has been observed to be an anchoring interface for chromosomal domains, providing for relatively fixed positions of 3D nuclear structures and a method of spatially regulating levels of accessibility of the chromosome for transcriptional expression (Pickersgill et al., 2006). Although many associations between clusters tend to be *cis*, located on the same arm of the chromosome, large-scale studies have also captured robust intrachromosomal contrats between territories of opposite arms on the same chromosome and interchromosomal contacts between different chromosomes(Simonis et al., 2006). Custom fluorescence in situ hybridization (FISH) probes utilizing exonic regions of entire chromosomes have been used to reveal how gene-dense chromosomal regions extend contacts beyond their own territories and outside of core territories traditionally defined by earlier studies using FISH probes with more simplistic oligonucleotide pools (Boyle et al., 2011).

The spatial context has been observed to play a large role in the extent of intra- and interchromosomal contacts between chromosomal regions despite similarities in nucleic sequence. One study replaced endogenous mouse α-globin locus with the human 120 kb α-globin locus from human primary erythroid cells in mouse erythroid cells. The nuclear organization properties of the 'humanized' α-globin locus in context of the mouse erythroid cells were characteristic of the mouse α-globin locus, with a more condensed local chromatin environment and fewer *trans* associations with other highly expressed erythroid gene loci (Brown et al., 2008).

Modulating cellular geometries via micropatterning has been shown to shift the radial position of CTs, the degree of CT pair intermingling, and ultimately alter gene expression. Cell geometries of 3T3 mouse fibroblast cells were modulated using micropatterns that were either isotropic circular substrates (area 500 μm^2) substrates or anisotropic rectangular substrates (aspect ratio 1:5, area 1800 μm^2) (Yejun Wang et al., 2017). The anisotropic substrates imposed more physical spreading stress and resulted in flattened, elongated nuclei with long actin stress fibers in contrast with the more spherical nuclei and shorter actin filaments associated with cells grown on the isotropic substrates. The spatial organizations of 12 representative CTs were visualized using FISH, and their associated volumes, radial distances, radial positions, chromosome decompaction factor, and transcriptional activities were compared between the two conditions. Different CT pairs demonstrated varying responses of chromosome intermingling depending on the cell geometries. For example, CTs 2/6 and 11/15 exhibited increased intermingling in isotropic substrates compared to anisotropic substrates while CT pair 5/9 showed significantly decreased intermingling when

comparing isotropic to anisotropic conditions. When subjected to cell geometric changes, several CTs increased their decompaction factors, which resulted in higher transcription as assessed by immunofluorescence of Pol II S5P, an active transcription marker. Microarray data derived from isolated RNA from the cultured 3T3 cells revealed lower expression of SRF/MRTF-A–regulated genes and higher expression of NF-κB–regulated genes for rounded cells in isotropic substrates compared to the cells on anisotropic cells (Yejun Wang et al., 2017).

The effect of cell shape on genetic expression involves a complicated interplay between the ECM, cytoskeleton, and nucleus, which has led to computational efforts to integrate all three domains in a model. One such study used an active 3D chemomechanical model to elucidate the interplay between the nucleus, cytoskeleton, and focal adhesions (Alisafaei et al., 2019). The model took into account formation of focal adhesions and ECM tension to represent the effect of substrates on the shape and organization of the cell. To describe the cytoskeletal architecture, parameters were included to describe the force exerted by myosin motors, cytoskeletal tension and stiffening, and actomyosin contractility. Finally, the nuclear envelope tension, lamin AC levels, nuclear stiffness, and epigenetic and chromatin condensation were included to assess transcriptional expression and describe the nuclear environment. It was found that subjecting the cell to geometric constraints in the form of low isotropic cytoskeletal tension in circular substrates versus high and polarized cytoskeletal tension in high aspect ratio rectangular substrates resulted in increases in local tensile stresses formed at mature focal adhesions, inducing alterations in the cytoskeleton and its associated

actors and resulting in softening of the nuclear lamina, stiffening of chromatin, and decreased nuclear volume (Alisafaei et al., 2019).

Important biological processes, including differentiation, genetic expression, proliferation, and apoptosis, have all been shown to be substantially influenced by the shape of the cell, which in turn relies heavily on the ECM and the focal adhesions associated with the extracellular substrate. Computational models and FISH analyses have suggested that these changes are largely mediated through the mechanosensitivity of the nucleus, with its malleable shape affecting the orientation, position, and packing of chromosomes that ultimately determine the extent of genetic expression. Further studies have unpacked how the dysregulation of natural processes, namely proliferation in the context of cancerous cells, can be influenced by, and in turn influence, the shape of the cell.

Morphological and invasive properties of cancerous cells

Cancer cells are notable for their ability for their ability to navigate complicated 3D environments in organisms, exhibiting unchecked growth, a parasitic invasiveness throughout the host system, and a high chance of proving fatal for the host. It is projected that in the United States alone, the year 2023 will end with 1,958,310 new cases of cancer and 609,820 deaths as a result of cancer (Siegel et al., 2023). Advances in treatments have created progress over the past few decades as the cancer death rate has declined by roughly 33% since 1991, averting an estimated 3.8 million potential deaths. However, rising incidences for uterine corpus, prostate, and breast cancers pose a threat to these gains, along with racial disparities in mortality. For men,

the majority of new cases are the result of prostate, lung & bronchus, colon & rectum, and urinary bladder cancers. As for women, breast cancer alone is projected to comprise 31% of new cases with an absolute number of 297,790 cases. Along with breast cancer, lung & bronchus and colon & rectum make up the majority of new cancer cases for women (Siegel et al., 2023). Due to the enormous fatalities and burden upon the nation's healthcare systems, an enormous amount of research has been dedicated towards characterizing cancer biology to identify potential drug targets or therapeutic interventions that could attenuate the substantial toll this class of diseases takes upon society.

While the severity and prognosis of cancers differ depending on the organ of origin, there are some commonalities that unite the subclasses of cancer diseases. There exist six hallmarks of cancer that enable tumor growth and metastatic dissemination that spreads tumors to secondary sites: sustained proliferative signaling, evading growth suppressors, activating invasion and metastasis, enabling replicative immortality, inducing angiogenesis, and resisting cell death (Hanahan & Weinberg, 2011).

Perhaps the most fundamental trait of cancer cells is their ability to chronically sustain unchecked proliferation. Normal tissues tightly regulate progression throughout growth-and-division cycles. Through dysregulation of these regulated checkpoints, cancer cells enable unchecked growth. Cancer cells utilize various methods to sustain proliferative signaling. The production of growth factor ligands, stimulating neighboring normal cells to supply the cancer cells with an abundance of growth factors, deregulating receptor signaling by elevating cell surface receptor ligand expression so

as to be hyperresponsive to growth factor ligands, or structural alterations in the growth factor ligands themselves to boost receptor response. Downstream pathways may also be subjected to somatic mutations. For example, roughly 40% of human melanomas exhibit characteristic mutations in B-Raf protein structure, which results in constitutive signaling to mitogen-activated protein (MAP)-kinase pathway (Hanahan & Weinberg, 2011). Disruptions to negative-feedback loops necessary for attenuating proliferative growth or the disabling of apoptosis-inducing or senescence circuitry are also common strategies employed by cancer cells to achieve unchecked growth (Hanahan & Weinberg, 2011).

The circumvention of tumor suppressor circuitry allows the cancer cells to avoid limitations of cell growth and proliferation. Retinoblastoma-associated (RB) and TP53 proteins, prototypical tumor suppressors, are critical regulatory nodes that govern the choice between proliferation or apoptosis and senescence (Hanahan & Weinberg, 2011). The RB serves as a crucial gatekeeper of cell-cycle progression, integrating signals from a myriad of intracellular and extracellular sources. Defects in RB pathway function thus prevents that critical signal processing step and permits chronic cell proliferation. The role of TP53 typically involves assessing the degree of damage to intracellular operating systems such as genome damage or if levels of glucose, oxygenation, growth-promoting signals, or nucleotide pools are suboptimal, which would trigger an abrogation of the cell-cycle progression until the conditions were restored to optimal levels (Hanahan & Weinberg, 2011). Cell-to-cell contact also serves as a powerful inhibitor of cell proliferation, with normal cells suppressing cell proliferation when reaching dense population sizes in two-dimensional culture conditions. A

cytoplasmic *NF2* gene product named Merlin is responsible for strengthening adhesivity of cadherin-mediated attachments between cells, as well as sequestering growth factor receptors, which limits mitogenic signaling (Hanahan & Weinberg, 2011).

A natural barrier to cancer proliferation is apoptosis, programmed cell death. During tumorigenesis, cells typically trigger signaling circuitry responsible for apoptotic programs responding to physiological stress signals in order to stymie cancer development (Hanahan & Weinberg, 2011). After sensing and integrating intracellular and extracellular death-inducing signals, such as levels of oncogene signaling or DNA damage, proteases caspases 8 and 9 initiate a cascade of downstream effector caspases that progressively disassemble the cell through proteolysis, which is then consumed by phagocytic cells or even its neighbors. Increased expression of regulators that inhibit apoptosis, such as Bcl-2 or Bcl-x_L or downregulating factors promoting apoptosis, such as Bax, Puma or Bim, can achieve circumvention or limiting of apoptosis (Hanahan & Weinberg, 2011).

Immortalization is the ability for cancerous cells to exhibit unlimited proliferative potential. Spontaneously immortalized cells such as cancer cells express substantial levels of telomerase, a DNA polymerase adding repeat segments to the ends of telomeric DNA, protecting the ends of chromosomal DNAs from generating unstable fused chromosomes that threaten the viability of the cell. The telomerase activity results in a resistance to apoptotic and senescent programs and enables immortalization of cancerous cell lines (Hanahan & Weinberg, 2011).

The acquisition of oxygen and nutrients to sustain the proliferation of tumors requires an extensive neovasculature, involving angiogenesis of vessels as supply

conduits. Angiogenesis inducers such as vascular endothelial growth factor-A (VEGF-A) encode ligands responsible for generating blood vessel growth (Ferrara, 2009). Oncogene signaling and hypoxic conditions have been noted to upregulated gene expression of VEGF (Feilim Mac Gabhann and Aleksander S. Popel, 2009). While normal vasculature is arrayed in well-differentiated, evenly-spaced hierarchies, tumor vasculature is characterized by its chaotic mixture of disorganized vessels with irregular structure, organization, and function compared to normal tissues (Nagy et al., 2010).

Eventually tumors reach a certain stage where they metastasize, invading throughout the body from their primary sight. Local invasions begin with the loss of E-cadherin expression in carcinoma cells, disrupting their adhesion to neighboring cells, and the upregulation of matrix attachment proteins so cancer cells can being navigating their surrounding environment (Hanahan & Weinberg, 2011). This transition is a co-opting of the developmental regulatory program epithelial-mesenchymal transition (EMT) that is normally used for wound healing or embryonic morphogenesis (Klymkowsky & Savagner, 2009). Transcriptional factors, such as Zeb1/2, Slug, Snail, and Twist, express in malignant tumor types, orchestrating the EMT (Micalizzi et al., 2010). EMT involves loss of cell-cell adhesion, modulation of cytoskeletal system organization, polarity changes, and increased motility (Klymkowsky & Savagner, 2009). Additionally, the morphology of the cell changes from a polygonal shape suited for epithelial sheet packing to instead a spindly morphology similar to fibroblasts, along with expression of enzymes degrading the ECM (Hanahan & Weinberg, 2011). Cancer cells then invade nearby lymphatic and blood vessels, transiting through these blood

systems, exiting these vessels via extravasation and colonizing of small cancer cell nodules into macroscopic tumors (Talmadge & Fidler, 2010).

The invasion process involves navigating a complicated 3D physical environment, with wide ranges of properties including fiber alignment, molecular composition, ECM pore size, and stiffness (Spill et al., 2016). One such property is the stiffness of the substrate, defined as the extent to which a material is able to resist against deformation upon application of mechanical force (Janmey et al., 2020). Cancer cells preferentially travel along gradients of substrate stiffness, in a process called durotaxis where cells go from softer to stiffer environments (Spill et al., 2016). Additionally, some cases revealed that cells can undergo “reverse durotaxis,” where they migrate from stiff to soft substrates (Spill et al., 2016).

Along with substrate stiffness, the 3D topologies and spaces of the ECM in the tumor microenvironment are widely varied. Longitudinal tunnel-like tracks, pores, and pro-migratory niches are crafted by cancer-associated fibroblasts and mast cells that release proteinases and crosslink collagen fibers together (Paul et al., 2017). Even healthy tissues exhibit ordered matrix environments with tracks of ECM fibers in vasculature, along blood vessels, and in the interstitial space between nerves and muscles (Paul et al., 2017). Whether in normal or cancerous tissues, these tracks have been observed to be crucial for metastatic migration from the primary site to secondary sites throughout the body. In a rat xenograft model with MTLn3 cells, an especially invasive breast adenoacarcinoma cell line, the tumor cells demonstrated a high preference for migration along collagen fiber tracks radiating throughout the primary tumor site (Sahai et al., 2005). An *in vivo* mouse brain model revealed melanoma cells

using blood vessel outer surfaces as scaffolding guides for proliferation and migration throughout the brain (Kienast et al., 2010). In a therapeutic approach harnessing the propensity for tumor cells to migrate along the direction of topographical tracks, aggressive brain tumor glioblastoma multiforme cells migrated along inserted nanofiber xenograft tracks that resulted in significantly lower tumor volume in the brains of rats (A. Jain et al., 2014). The topography of the environment surrounding the tumor has a substantial influence on the direction and extent of cancerous cell migration and invasion to other parts of the host organism.

Due to the importance of the topological landscape of the substrate, more studies have investigated how spatial parameters of the substrate can be processed by the cell and influence cellular functions. The effect of the physical environment on cells can have substantial biological implications, informing future efforts for uncovering underling crucial biological processes as well as providing foundational knowledge for therapeutic interventions.

Micropatterning isolates and subjects adhesive cells to specified geometric constraints

Micropatterning is a well-established technique for reflecting spatial complexities observed throughout *in vivo* microenvironments of cells. It allows for printing biomolecules of interest in highly specified geometries on the micrometer scale (Strale et al., 2016). Micropatterning can even be used for patterning gradients of molecules of interest and even multi-protein combinations of substrates, providing several knobs of

control to probe the effects of different elements of the physical extracellular environment on cellular functions.

Micropatterning harnesses advancements in projection lithography systems, antifouling backgrounds, photoinitiators, and UV illumination to create highly specialized geometric patterns. Digital micromirror devices (DMD) are spatial light modulators that operate extensive arrays of micromirrors operating as binary light switches that can either turn off or on (Ren et al., 2015). For switching between on or off states, typical DMDs operate with micromirrors that have the ability to rotate either +12º or -12º relative to the surface normal. Intensity modulation is achieved by uploading grayscale versions of the desired patterns to the device, encoding for sequential pulse width of the light signal shining (Ren et al., 2015). This is particularly useful for generating gradients along micropatterns to test questions regarding threshold signal detection for substrates or how gradients can guide directionality for cell motility.

Antifouling backgrounds are grafted onto a glass surface so as to prevent cells or proteins from adhering to areas outside of the patterned substrates. Polycationic poly(L-lysine)-g-poly(ethylene glycol) (PLL-g-PEG) is a commonly used antifouling system for modifying negatively charged surfaces (Falconnet et al., 2006). PLL-g-PEGs provide polymeric brushes on the PEG sides of the molecule while providing a charged anchor with the PLL side that will bind with glass surfaces treated with plasma.

After binding of the antifouling coating agent, a water-soluble photoinitiator is used to tune the polymer brush antifouling properties through a photoscission mechanism (Strale et al., 2016). Upon shining through UV light, the photoinitator degrades into reactive oxygen species (Hong et al., 2019). These reactive species have

the ability to cleave bonds between the PLL-g-PEGs and the glass surface, thus ablating the antifouling coating agent in locations wherever the UV light is shined upon (Ninomiya et al., 1998). Within the micrometer-scale spaces exposed to UV light, the antifouling coating agent is either eliminated or relieved of its antifouling abilities due to photoinitiator activity, creating a negative space within the antifouling coat layer where proteins have the ability to bind to the glass underneath.

Within the negative space, the protein of interest can be added and incubated until they strongly adhere. After the incubation step, the media can be flushed with solvent to eliminate excess substrate protein. What is left are the micropatterns with the substrate of interest in specified geometries, surrounded by antifouling coating agents that will prevent either cells or molecules of interest from binding to areas outside of the micropatterns. The other areas with antifouling coating agent can still be subjected to further photoinitiator and UV exposure to create other micropatterns with different proteins of interest. In one example, researchers patterned three different fluorescent markers, using GFP, Pll-g-PEG-TRITC, and Neutravidin-Ato647, to paint a striking micrometer-scale recreation of the Birth of Venus by Boticelli (Strale et al., 2016). Depending on the strength of the UV light and the concentration of photoinitiator, the adsorbed protein density can be tailored according to the desired parameters of the experiment (Strale et al., 2016). In one step, the pattern sizes can range from as small as 500nm to as large as 1mm (Strale et al., 2016). Larger pattern compositions can easily be printed and simply require however number of steps are required to overcome the limit of the DMD size range and accommodate the size of the desired micropattern. The versatility of micropatterning, with its ability to print different concentrations of

proteins of interest, multiple proteins, and precise geometries on the nanometer and micrometer scale, makes it an attractive method for probing how cells respond to different physical aspects of their extracellular environment.

Several studies have used micropatterning to reveal how the underlying cytoskeletal machinery arranges itself in response to different spatial inputs. Fibronectin is a commonly used substrate for these types of micropatterning experiments both because of its ubiquitous presence in ECM environments and because it is a ligand for dozens of integrin receptors, cell-surface heterodimers responsible for linking the intracellular cytoskeleton to the ECM (Pankov & Yamada, 2002). Therefore, it is a natural choice to be the substrate protein of choice to recapitulate *in vivo* ECM environments and to ensure the cell will grip the surface through focal adhesion machinery and influence cytoskeletal architectures inside of the cell. Minimal integrin-recognition sequences have been identified, including the best known sequence of RGD (Pankov & Yamada, 2002). In one study using fibronectin micropatterns, the investigators cultured pulmonary vascular smooth muscle (VSM) cells on increasing fibronectin densities versus 30 x 30μm islands (Polte et al., 2004). VSM cells constricted on the islands were unable to spread and also exhibited decreased myosin light chain phosphorylation, suggesting that cell spreading is necessary for biochemical signal transduction during smooth muscle cell contractility (Polte et al., 2004). Dynamic actin structures arise with non-migrating cells on micropatterns, with vasodilator-stimulated phosphoprotein and zyxin demonstrating preferential localization to actin filament bundles at the apices and exhibited higher traction forces (Guo & Wang, 2007).

Several studies have investigated how specific cytoskeletal structures arise depending on the idiosyncrasies of geometric micropatterns. HeLa cells were adhered to micropatterned rectangles, triangles, circles, and L shapes (Théry et al., 2005). Cortactin, involved in membrane ruffling through actin polymerization and ezrin, a key player in cell polarity, were found to be enriched in adhesive areas of the cell cortex (Théry et al., 2005).

In another study, cells were grown on circles of varying size, triangles, and a V shape (Théry, 2010). Depending on the shape, size, and number of adhesive edges, the cytoskeletal structures, visualized through fluorescent antibodies for vinculin and F-actin, differed. Smaller circles resulted in low spreading cells characterized by branched meshworks of actin. Larger circles exhibited actin branched meshworks evenly throughout the edge of the circumference, along with adject actin filament bundles and stress fibers stretching across the diameter of the circle. Triangles with all three edges having adhesive properties exhibited concentrations of vinculin and branched meshworks at the apices of the triangle, actin filament bundles stretched out across the body of the triangle, and stress lying mostly along the edges of the shape. V shapes that were the same height and base as the triangle shapes, but missing an adhesive edge and some of the central body of the triangle, also demonstrated concentrations of branched actin meshworks and vinculin at the apices. In contrast to the triangle micropattern cells, cells adhered to the V shape exhibited stress fibers stretching across the central part of the micropattern along with the adhesive edges. Filament bundles were not observed. Additionally, the filament bundles along the non-adhesive edge were

noted to have a distinctly concave shape, buckling inwards and connected by the two apices along the non-adhesive edge (Théry, 2010).

Similar studies were conducted to assess how the cell adhesive microenvironment determines the internal organization of the cell as well as its polarity orientation. Human retinal pigment epithelial (RPE) cells were cultured on anisotropic fibronectin micropatterns to assess the effect of anisotropic environments on the cell internal organization (Théry et al., 2006). The researchers quantified the spatial organization of the nucleus, Golgi apparatus, centrosome, distribution of microtubules, actin network organization, and associated proteins. Cell polarity was defined by spatial asymmetries of cellular compartments relative to a polar axis. After observing the inhibition of stress fiber development along curves of adhesive borders, the authors used a crossbow-shaped micropattern to polarize the cell, imposing a curved adhesive border to one of the cell and creating two non-adhesive edges to the other half. Vinculin, actin, and cortactin were fluorescently labeled with antibodies, and images of multiple cells on the same micropattern were averaged to analyze the localization of these cytoskeletal-associated structures relative to the crossbow micropatterns. Vinculin structures exhibited asymmetric distributions, accumulating at adhesive zone extremities but regularly localizing at lower levels across the curve of the bow. Stress fibers spread across the non-adhesive edges, but they were nearly absent from the curved adhesive border. Cortactin expression was limited to the adhesive sides. Combining the fluorescent results, the authors concluded that the crossbow shapes consistently polarized the organization of the cell, resulting in a reproducible

polymerizing meshwork at the adhesive border and stress fibers stretched across non-adhesive edges (Théry et al., 2006).

As a proxy for cell protrusions, the researchers visualized the localization of APC, an actin-binding protein characterized for its affinity for cell protrusion zones, as well as its connection between microtubule and actin networks. By assessing where APC accumulated relative to the micropattern, they were able to surmise how the micropattern would influence where potential lamellipodia or filopodia would extent. On the crossbow micropatterns, APC accumulated all along the adhesive peripheries and was notable missing from non-adhesive edges (Théry et al., 2006). What this suggests is that the adhesive substrate underneath a cell can mediate the directionality of cell protrusions and extensions.

To evaluate how polarity of the cell was influenced by geometries of the ECM, RPE1 cells were plated on micropatterns with arrow shapes, X, K, and C. These particular geometries were selected due to the resulting shared phenotype of a squared envelope for the overall shape of the cell, but presumably with varying internal cellular architectures underneath the cell membrane due to the difference in non-adhesive edge and adhesive edge numbers. Cells plated on the X micropattern exhibited an even distribution of polarizations across 360º of possible orientations as determined by the centrosome-Golgi-nucleus axis pointing from the nucleus out towards the centrosome. There was no preference for cellular orientation, presumably because there were four non-adhesive edges, so the cell had no adhesive guide to consistently orient its internal architecture. By contrast, cells plated on the C shape reproducibly oriented opposite the non-adhesive edge and towards the adhesive edge in the middle, flanked by the two

perpendicular adhesive edges. The K shape micropatterns had similar results, with the cell polarizing opposite the largest non-adhesive edge and towards the adhesive edge attached by the two legs mirrored 180º from each other. When cells were plated on arrow shaped micropatterns, there was a strong preference for the orientation pointed towards the arrowhead, which was opposite of two non-adhesive edges (Théry et al., 2006). Taken together, these results suggest that adhesive substrate spatial geometries can largely influence the internal polarity of cells, notably with the presence of adhesive apices guiding cell architecture along the distal end of those geometries.

Micropatterning studies have shown that micropatterning can isolate single cells and reveal their morphological, cytoskeletal, and internal polarity preferences based on the underlying geometries of the adhesive substrates. Micropatterning provides for various knobs of control, such as protein concentration, precision in printing micrometer scale shapes, gradients, and multiple proteins within the same pattern. This versatility enables researchers to tackle numerous kinds of questions. By using fibronectin as the substrate protein of choice, the ECM-integrin-cytoskeletal interface as observed *in vivo* is preserved, or at least approximated to an extent, *in vitro*. While these studies mostly focused on nonmigrating cells, other researchers have used micropatterning as a tool to evaluate migration patterns compared between different kinds of conditions and cell lines.

Micropatterning reveals characteristic cancer cell migratory trajectories

Due to the numerous studies that have shown decision making processes involved with metastasis substantially rely on substrate topology and spatial geometries

within the ECM, many researchers have turned to micropatterning to probe how tuning substrate spatial patterns can reveal migratory habits for cancer cells.

In one particular study, researchers subjected breast cancer cell line MDA-MB-231 cells and model normal human breast MCF-10A cells to two-state micropatterns to compare their migratory dynamics (Brückner et al., 2019). The authors sought to search for emergent dynamical laws when migratory cells were confined to well-defined geometries. To that end, the researchers designed a two-state system for confined cell migration, printing a fibronectin micropattern with a dumbbell-like shape with two square lobes connected by a thin bridge. PLL-PEG was passivated onto the surrounding area to repel cell adhesion. MDA-MB-231 cells demonstrated a stochastic cellular 'hopping' behavior, migrating back and forth between the two square islands and across the thin bridge multiple times across the span of observation time, over 40 hours (Brückner et al., 2019). Crossing the bridge required development of a lamellipodium, formed along the cell periphery, which would extend and sometimes grow into a sustained protrusion. During a successful migration, the protrusion would broaden, growing into a fan-like shape.

Within that same study, researchers developed a mathematical model to describe the nonlinear oscillations between the two adhesive islands. For MDA-MB-231 cells subjected to the islands connected by the thin constriction, the trajectories always approached a stable limit cycle, indicating that no matter the initial conditions in position or velocity, the cells would always travel back and forth between the two islands. To assess the effect of spatial constraints on the deterministic dynamics, the authors also compared the trajectories of the breast cancer cells on micropatterns without a thin

constriction, essentially a full rectangle of space available for the cell to adhere to. For the same cancer cells presented to micropatterns without the constriction, the deterministic dynamics inevitably resulted in a trajectory with a velocity of zero, indicating that no matter the initial position or velocity, the cells would always end up stationary and stop migrating. The final location of the cells after they reached a velocity of zero was evenly distributed along the rectangle, with no strong preference along the micropattern. To contrast with cancerous cells on the two-island adhesive micropatterns, non-cancerous breast tissue MCF10A cells were plated onto the same geometries. Instead of the limit cycle demonstrated by the MDA-MB-231 cells, the MCF10A exhibited two stable fixed points, representing the two islands sitting on either side of the thin constriction bridge. Within the phase diagram measuring relative position against velocity, the authors noted that basins of attraction extended from one side of the system to the other, suggesting that a small perturbation, even induced by noise, could excite the cell from one side of the system to the other (Brückner et al., 2019).

A few critical conclusions relating cellular morphology and substrate spatial complexity can be drawn from these results. One is that the types of geometries within the ECM can have a large influence on the same cell type in determining cellular morphology and migration trajectories. Two islands with a thin constriction induce stable limit cycles of shuttling back and forth, while a solid rectangle with similar dimensions all ended with a velocity of zero and random endpoint localizations. Another conclusion is that the cell type on the same geometries can result in different morphologies and trajectories. While the invasive MDA-MB-231 cells on the two-island adhesive patterns

exhibited limit-cycle oscillations, the less invasive MCF10A cells demonstrated bistable dynamics, eventually settling in to either of the two islands with a velocity of zero.

Although measuring the dynamics of position and velocity over time can yield useful insights, as demonstrated in the previous sections of the introduction, it is also important to characterize the morphology of the cell over time because of how cellular shape has such an influential role in critical biological processes. Various efforts to quantify the morphology of cellular shapes have been undertaken in order to draw more rigorous conclusions in contrast to qualitative statements that oftentimes dominate conversations about cellular morphologies.

Quantifying cellular morphology

Cellular shape determines and is determined by important biological processes, which necessitates its quantification in order to better understand those processes. Various efforts have been undertaken to describe cell shape in a way that allows for easy comparison between different experimental conditions, can be analyzed with large scale statistical tools, and recapitulates the essential and relevant biological features in question. Oftentimes, a trade-off between accuracy of recapitulating the shape and malleability of the data used to encode the shape is required.

Earliest efforts relied on landmarks to identify and compare shapes. On the scale of organisms, animal anatomical features are oftentimes used as biological landmarks. One example of a geometric morphometrics is Procrustes analysis for fish, which relies on twelve landmarks to quantify fish specimens shape variation, such as *Cyprinodon bovinus* (Black et al., 2017). These landmarks include the coordinate positions of

features such as the snout tip, center of the eye, caudal peduncle upper and lower margins, dorsal elevation, predorsal elevation, and much more. While these features may work well with higher level organisms, in the case of individual cells, it is more difficult to identify unequivocal landmark points that could be matched and compared across entire cell populations due to their high variability and general smoothness that precludes the identification of idiosyncratic features.

Instead of landmarks, other quantitative efforts have focused on measurements or features of the cell as a geometric object. These measurements include parameters such as area, circularity, length of the minor or major axes of an object. In the case of 3D microscopy, the volume and internal slices of the object can also be measured. This approach overcomes the shortcomings of the geometric morphometrics in that these measurements can be compared across entire cell populations. However, the extent of the shape information is limited to the features selected *a priori* for analysis, running the risk of excluding potentially significant or interesting shape features (Pincus & Theriot, 2007).

Outline encoding allows for the entire shape to be captured. The simplest way involves a parametric plane curve, with the cartesian x and y coordinates collected as lists of points. Alternatively, a signed distance map is an array of each pixel within the image, with their intensities calculated as the distance between their position and the distance from the nearest edge of the cell. The interior of the cell is negative, the cell edge values are all zero, and the values outside of the cell are position, thus creating a sort of topological map where the cell edge, cell interior, and extracellular environment are all encoded depending on their value signs and presence or absence of values

(Pincus & Theriot, 2007). However, outline encoding still poses challenges in comparison to different experimental conditions because each numerical component of the encoded shape corresponds to a singular point as opposed to the shape as a whole.

Dimensionality reduction techniques circumvent this issue by breaking down high-dimensional data into a smaller number of parameters with biological significance and an interpretability for data analysis. Classical Fourier decomposition can be imposed upon cell outlines, using sines and cosines of increasing frequency as an orthogonal basis set (Lestrel, 1989). Both the x-values and the y-values of the points can be decomposed separately, yielding two sets of coefficients that can be combined to create a single vector of description. These coefficients represent the frequencies of the sines or cosines that can be summed to approximate the overall outline shape of the cell in 2D. Zernike polynomials have also been used to provide orthogonal 2D basis sets to describe images (Pincus & Theriot, 2007). Although originally designed as shape modes that could be weighted and combined to describe aberrations in optical lenses, they can be used to decompose any kind of digital image. The predetermined orthogonal basis sets either with Fourier decomposition or Zernike polynomials provide a common set for comparison between experimental conditions, as well as providing a reduced set of dimensions to describe the overall shape.

The drawback to these approaches is that the shape is decomposed in a pre-specified way. Thus, specific features unique to the orthogonal basis set, such as the smoothness of the curves of the sine or cosine waves or the blurred patchiness from the Zernike polynomials, are the only sorts of features that can be extracted from the

biological images of cells. It's not guaranteed that the biologically meaningful variation in the data will be retained with these approaches. To address this shortcoming, many researchers turn to principal component analysis (PCA).

Principal component analysis as dimensionality reduction enables time series dynamics analysis

While qualitative observations prevail for describing cellular morphologies, more recent studies with model organisms as varied as protists to worms have quantified the shapes of cells in a more statistically rigorous manner using principal component analysis. This linear algebra technique provides eigenvectors that can be ordered by their eigenvalue, showing how much they can describe the statistical deviation from the mean of the sample data set, allowing for a ranking and ultimate selection of a few eigenvectors that can be assigned scalar weights to describe the dynamics of the raw data over time.

Unicellular predator *Lacrymaria olor* is a single-celled protist, with fast hunting behaviors utilizing a slender neck that broadly samples the surrounding area of the cell (Coyle et al., 2019). In order to analyze the dynamics of the protist morphology over time during its hunting behavior, the researchers used nearly 200,000 cell shapes to derive principal components to explain the variance in the data. The top four shape modes that fell out from the analysis explained over 98% of the shape variance, resembling harmonic modes that easily resembled the shapes of the hunting cells (Coyle et al., 2019). Dynamic shape patterns were identifiable by analyzing the time

series data of shape mode scalar weights assigned to the linear encoded neck position values. Whipping, steering, reorienting, and sampling behaviors were all analyzed.

In a paper analyzing the locomotion dynamics of *Caenorhabditis elegans*, they also took a principal component analysis approach to describe the shape of the worm and capture its locomotory behavior (Gyenes & Brown, 2016). With just four principal components, derived from a collection of 12,600 shapes, more than 90% of the variance in the data was explained. The two-dimensional movement of propagating bending waves along the nematode worm body was amenable for encoding the overall shape of the body. The time series data of the principal components revealed characteristic wave patterns revealing behaviors such as head oscillation, turning, and sinusoidal crawling.

The goal of my thesis was to digitize and encode shape descriptions of breast cancer cells to detect morphological events such as extensions, and to leverage principal component analysis to capture global statistics of morphological behaviors between different experimental conditions. Due to the wide body of literature suggesting the significant impact of substrate spatial complexity on cell morphology and trajectories, I sought to systematically assess how changing the size and spatial complexity of micropatterns would change the dynamics of metazoan cell morphologies. Additionally, I compared different cell types in a breast cancer cell panel, along with the model cell line for morphological and motility studies, 3T3 mouse fibroblasts, to evaluate how different cell lines would respond to the same types of geometric substrates.

References

Akanuma, T., Chen, C., Sato, T., Merks, R. M. H., & Sato, T. N. (2016). Memory of cell shape biases stochastic fate decision-making despite mitotic rounding. *Nature Communications*, *7*(May). https://doi.org/10.1038/ncomms11963

Alisafaei, F., Jokhun, D. S., Shivashankar, G. V., & Shenoy, V. B. (2019). Regulation of nuclear architecture, mechanics, and nucleocytoplasmic shuttling of epigenetic factors by cell geometric constraints. *Proceedings of the National Academy of Sciences of the United States of America*, *116*(27), 13200–13209. https://doi.org/10.1073/pnas.1902035116

Bickmore, W. A., & Van Steensel, B. (2013). Genome architecture: Domain organization of interphase chromosomes. *Cell*, *152*(6), 1270–1284. https://doi.org/10.1016/j.cell.2013.02.001

Bischofs, I. B., & Schwarz, U. S. (2003). Cell organization in soft media due to active mechanosensing. *Proceedings of the National Academy of Sciences of the United States of America*, *100*(16), 9274–9279. https://doi.org/10.1073/pnas.1233544100

Black, A. N., Seears, H. A., Hollenbeck, C. M., & Samollow, P. B. (2017). Rapid genetic and morphologic divergence between captive and wild populations of the endangered Leon Springs pupfish, Cyprinodon bovinus. *Molecular Ecology*, *26*(8), 2237–2256. https://doi.org/10.1111/mec.14028

Boyle, S., Rodesch, M. J., Halvensleben, H. A., Jeddeloh, J. A., & Bickmore, W. A. (2011). Fluorescence in situ hybridization with high-complexity repeat-free oligonucleotide probes generated by massively parallel synthesis. *Chromosome*

Research, *19*(7), 901–909. https://doi.org/10.1007/s10577-011-9245-0

Brown, J. M., Green, J., Neves, R. P. Das, Wallace, H. A. C., Smith, A. J. H., Hughes, J., Gray, N., Taylor, S., Wood, W. G., Higgs, D. R., Iborra, F. J., & Buckle, V. J. (2008). Association between active genes occurs at nuclear speckles and is modulated by chromatin environment. *Journal of Cell Biology*, *182*(6), 1083–1097. https://doi.org/10.1083/jcb.200803174

Brückner, D. B., Fink, A., Schreiber, C., Röttgermann, P. J. F., Rädler, J. O., & Broedersz, C. P. (2019). Stochastic nonlinear dynamics of confined cell migration in two-state systems. *Nature Physics*, *15*(6), 595–601. https://doi.org/10.1038/s41567-019-0445-4

Burridge, K., Guilluy, C., Burridge, K., & Guilluy, C. (2016). Focal adhesions , stress fibers and mechanical tension. *Exp Cell Res*, *343*(1), 14–20. https://doi.org/10.1016/j.yexcr.2015.10.029.Focal

Chen, C. S., Mrksich, M., Huang, S., Whitesides, G. M., & Ingber, D. E. (1997). Geometric control of cell life and death. *Science*, *276*(5317), 1425–1428. https://doi.org/10.1126/science.276.5317.1425

Coyle, S. M., Flaum, E. M., Li, H., Krishnamurthy, D., & Prakash, M. (2019). Coupled Active Systems Encode an Emergent Hunting Behavior in the Unicellular Predator Lacrymaria olor. *Current Biology*, *29*(22), 3838-3850.e3. https://doi.org/10.1016/j.cub.2019.09.034

Domanskyi, S., Hakansson, A., Meng, M., Pham, B. K., Graff Zivin, J. S., Piermarocchi, C., Paternostro, G., & Ferrara, N. (2022). Naturally occurring combinations of

receptors from single cell transcriptomics in endothelial cells. *Scientific Reports*, *12*(1), 1–17. https://doi.org/10.1038/s41598-022-09616-9

Evans, N. D., Oreffo, R. O. C., Healy, E., Thurner, P. J., & Man, Y. H. (2013). Epithelial mechanobiology, skin wound healing, and the stem cell niche. *Journal of the Mechanical Behavior of Biomedical Materials*, *28*, 397–409. https://doi.org/10.1016/j.jmbbm.2013.04.023

Falconnet, D., Csucs, G., Michelle Grandin, H., & Textor, M. (2006). Surface engineering approaches to micropattern surfaces for cell-based assays. *Biomaterials*, *27*(16), 3044–3063. https://doi.org/10.1016/j.biomaterials.2005.12.024

Feilim Mac Gabhann and Aleksander S. Popel. (2009). Systems biology of VEGF. *Microcirculation*, *15*(8), 715–738. https://doi.org/10.1080/10739680802095964.Systems

Ferrara, N. (2009). Vascular endothelial growth factor. *Arteriosclerosis, Thrombosis, and Vascular Biology*, *29*(6), 789–791. https://doi.org/10.1161/ATVBAHA.108.179663

Freed, D. M., Bessman, N. J., Kiyatkin, A., Leahy, D. J., Lidke, D. S., Lemmon, M. A., Freed, D. M., Bessman, N. J., Kiyatkin, A., Salazar-cavazos, E., & Byrne, P. O. (2017). EGFR Ligands Differentially Stabilize Receptor Dimers to Specify Signaling Kinetics EGFR Ligands Differentially Stabilize Receptor Dimers to Specify Signaling Kinetics. *Cell*, *171*(3), 683-685.e18. https://doi.org/10.1016/j.cell.2017.09.017

Gallo, G., & Letourneau, P. C. (2004). Regulation of Growth Cone Actin Filaments by Guidance Cues. *Journal of Neurobiology*, *58*(1), 92–102. https://doi.org/10.1002/neu.10282

Gallop, J. L. (2020). Filopodia and their links with membrane traffic and cell adhesion. *Seminars in Cell and Developmental Biology*, *102*(November 2019), 81–89. https://doi.org/10.1016/j.semcdb.2019.11.017

Guo, W., & Wang, Y. (2007). Retrograde Fluxes of Focal Adhesion Proteins in Response to Cell Migration and Mechanical Signals. *Molecular Biology of the Cell*, *18*(November), 4519–4527. https://doi.org/10.1091/mbc.E07

Gyenes, B., & Brown, A. E. X. (2016). Deriving shape-based features for C. elegans locomotion using dimensionality reduction methods. *Frontiers in Behavioral Neuroscience*, *10*(AUG), 1–9. https://doi.org/10.3389/fnbeh.2016.00159

Hanahan, D., & Weinberg, R. A. (2011). Hallmarks of cancer: The next generation. *Cell*, *144*(5), 646–674. https://doi.org/10.1016/j.cell.2011.02.013

Hoffmann, M. D., Bubeck, F., Eils, R., & Niopek, D. (2018). Controlling Cells with Light and LOV. *Advanced Biosystems*, *2*(9), 1–13. https://doi.org/10.1002/adbi.201800098

Hong, B. M., Park, S. A., & Park, W. H. (2019). Effect of photoinitiator on chain degradation of hyaluronic acid. *Biomaterials Research*, *23*(1), 19–26. https://doi.org/10.1186/s40824-019-0170-1

Hu, K., Ji, L., Applegate, K. T., Danuser, G., & Waterman-Storer, C. M. (2007).

Differential Transmission of Actin Motion Within Focal Adhesions. *Science*, *315*(January), 111–116.

Hynes, R. O., & Naba, A. (2012). Overview of the matrisome-An inventory of extracellular matrix constituents and functions. *Cold Spring Harbor Perspectives in Biology*, *4*(1). https://doi.org/10.1101/cshperspect.a004903

Innocenti, M. (2018). New insights into the formation and the function of lamellipodia and ruffles in mesenchymal cell migration. *Cell Adhesion and Migration*, *12*(5), 401–416. https://doi.org/10.1080/19336918.2018.1448352

Jain, A., Betancur, M., Patel, G. D., Valmikinathan, C. M., Mukhatyar, V. J., Vakharia, A., Pai, S. B., Brahma, B., MacDonald, T. J., & Bellamkonda, R. V. (2014). Guiding intracortical brain tumour cells to an extracortical cytotoxic hydrogel using aligned polymeric nanofibres. *Nature Materials*, *13*(3), 308–316. https://doi.org/10.1038/nmat3878

Jain, N., Iyer, K. V., Kumar, A., & Shivashankar, G. V. (2013). Cell geometric constraints induce modular gene-expression patterns via redistribution of HDAC3 regulated by actomyosin contractility. *Proceedings of the National Academy of Sciences of the United States of America*, *110*(28), 11349–11354. https://doi.org/10.1073/pnas.1300801110

Janmey, P. A., Fletcher, D. A., & Reinhart-King, C. A. (2020). Stiffness sensing by cells. *Physiological Reviews*, *100*(2), 695–724. https://doi.org/10.1152/physrev.00013.2019

Kienast, Y., Von Baumgarten, L., Fuhrmann, M., Klinkert, W. E. F., Goldbrunner, R.,

Herms, J., & Winkler, F. (2010). Real-time imaging reveals the single steps of brain metastasis formation. *Nature Medicine*, *16*(1), 116–122. https://doi.org/10.1038/nm.2072

Klymkowsky, M. W., & Savagner, P. (2009). Epithelial-mesenchymal transition: A cancer researcher's conceptual friend and foe. *American Journal of Pathology*, *174*(5), 1588–1593. https://doi.org/10.2353/ajpath.2009.080545

Lakhani, V., & Elston, T. C. (2017). Testing the limits of gradient sensing. *PLoS Computational Biology*, *13*(2), 1–30. https://doi.org/10.1371/journal.pcbi.1005386

Lanctôt, C., Cheutin, T., Cremer, M., Cavalli, G., & Cremer, T. (2007). Dynamic genome architecture in the nuclear space: Regulation of gene expression in three dimensions. *Nature Reviews Genetics*, *8*(2), 104–115. https://doi.org/10.1038/nrg2041

Le, H. Q., Ghatak, S., Yeung, C. Y. C., Tellkamp, F., Günschmann, C., Dieterich, C., Yeroslaviz, A., Habermann, B., Pombo, A., Niessen, C. M., & Wickström, S. A. (2016). Mechanical regulation of transcription controls Polycomb-mediated gene silencing during lineage commitment. *Nature Cell Biology*, *18*(8), 864–875. https://doi.org/10.1038/ncb3387

Legerstee, K., & Houtsmuller, A. B. (2021). A layered view on focal adhesions. *Biology*, *10*(11). https://doi.org/10.3390/biology10111189

Lestrel, P. E. (1989). Method for analyzing complex two-dimensional forms Elliptical Fourier functions. *American Journal of Human Biology*, *1*, 149–164.

Levental, I., Georges, P. C., & Janmey, P. A. (2007). Soft biological materials and their impact on cell function. *Soft Matter*, *3*(3), 299–306. https://doi.org/10.1039/b610522j

Li, Q., Kumar, A., Makhija, E., & Shivashankar, G. V. (2014). The regulation of dynamic mechanical coupling between actin cytoskeleton and nucleus by matrix geometry. *Biomaterials*, *35*(3), 961–969. https://doi.org/10.1016/j.biomaterials.2013.10.037

Li, S., Wong, A. H. C., & Liu, F. (2014). Ligand-gated ion channel interacting proteins and their role in neuroprotection. *Frontiers in Cellular Neuroscience*, *8*(May), 3–7. https://doi.org/10.3389/fncel.2014.00125

Li, Y. S. J., Haga, J. H., & Chien, S. (2005). Molecular basis of the effects of shear stress on vascular endothelial cells. *Journal of Biomechanics*, *38*(10), 1949–1971. https://doi.org/10.1016/j.jbiomech.2004.09.030

Mammoto, A., Huang, S., & Ingber, D. E. (2007). Filamin links cell shape and cytoskeletal structure to Rho regulation by controlling accumulation of p190RhoGAP in lipid rafts. *Journal of Cell Science*, *120*(3), 456–467. https://doi.org/10.1242/jcs.03353

Mejillano, M. R., Kojima, S., Applewhite, D. A., Gertler, F. B., Svitkina, T. M., & Borisy, G. G. (2004). Lamellipodial Versus Filopodial Mode of the Actin Nanomachinery. *Cell*, *118*(3), 363–373. https://doi.org/10.1016/j.cell.2004.07.019

Micalizzi, D. S., Farabaugh, S. M., & Ford, H. L. (2010). Epithelial-mesenchymal transition in cancer: Parallels between normal development and tumor progression. *Journal of Mammary Gland Biology and Neoplasia*, *15*(2), 117–134.

https://doi.org/10.1007/s10911-010-9178-9

Miller, C. (2000). An overview of the potassium channel family. *Genome Biology*, *1*(4), 1–5. https://doi.org/10.1186/gb-2000-1-4-reviews0004

Muller, P., & Schier, A. (2011). Extracellular Movement of Signaling Molecules. *Developmental Cell*, *21*, 145–158. https://doi.org/10.1016/j.devcel.2011.06.001

Nagy, J. A., Chang, S. H., Shih, S. C., Dvorak, A. M., & Dvorak, H. F. (2010). Heterogeneity of the tumor vasculature. *Seminars in Thrombosis and Hemostasis*, *36*(3), 321–331. https://doi.org/10.1055/s-0030-1253454

Nair, A., Chauhan, P., Saha, B., & Kubatzky, K. F. (2019). Conceptual evolution of cell signaling. *International Journal of Molecular Sciences*, *20*(13), 1–44. https://doi.org/10.3390/ijms20133292

Niedergang, F., & Chavrier, P. (2004). Signaling and membrane dynamics during phagocytosis: Many roads lead to the phagos(R)ome. *Current Opinion in Cell Biology*, *16*(4), 422–428. https://doi.org/10.1016/j.ceb.2004.06.006

Ninomiya, S., Ashihara, Y., Nakayama, Y., Oka, K., & West, R. (1998). Reduction of photoscission of σ bonds in polysilanes by fullerene doping. *Journal of Applied Physics*, *83*(7), 3652–3655. https://doi.org/10.1063/1.366584

Oakes, P. W., Bidone, T. C., Beckham, Y., Skeeters, A. V., Ramirez-San Juan, G. R., Winter, S. P., Voth, G. A., & Gardel, M. L. (2018). Lamellipodium is a myosin-independent mechanosensor. *Proceedings of the National Academy of Sciences of the United States of America*, *115*(11), 2646–2651.

https://doi.org/10.1073/pnas.1715869115

Pankov, R., & Yamada, K. M. (2002). Fibronectin at a glance. *Journal of Cell Science*, *115*(20), 3861–3863. https://doi.org/10.1242/jcs.00059

Paul, C. D., Mistriotis, P., & Konstantopoulos, K. (2017). Cancer cell motility: Lessons from migration in confined spaces. *Nature Reviews Cancer*, *17*(2), 131–140. https://doi.org/10.1038/nrc.2016.123

Pickersgill, H., Kalverda, B., De Wit, E., Talhout, W., Fornerod, M., & Van Steensel, B. (2006). Characterization of the Drosophila melanogaster genome at the nuclear lamina. *Nature Genetics*, *38*(9), 1005–1014. https://doi.org/10.1038/ng1852

Pincus, Z., & Theriot, J. A. (2007). Comparison of quantitative methods for cell-shape analysis. *Journal of Microscopy*, *227*(2), 140–156. https://doi.org/10.1111/j.1365-2818.2007.01799.x

Polte, T. R., Eichler, G. S., Wang, N., & Ingber, D. E. (2004). Extracellular matrix controls myosin light chain phosphorylation and cell contractility through modulation of cell shape and cytoskeletal prestress. *American Journal of Physiology - Cell Physiology*, *286*(3 55-3), 518–528. https://doi.org/10.1152/ajpcell.00280.2003

Ren, Y. X., Lu, R. De, & Gong, L. (2015). Tailoring light with a digital micromirror device. *Annalen Der Physik*, *527*(7–8), 447–470. https://doi.org/10.1002/andp.201500111

Riveline, D., Zamir, E., Balaban, N. Q., Schwarz, U. S., Ishizaki, T., Narumiya, S., Kam, Z., Geiger, B., & Bershadsky, A. D. (2001). Focal contacts as mechanosensors: Externally applied local mechanical force induces growth of focal contacts by an

mDia1-dependent and ROCK-independent mechanism. *Journal of Cell Biology*, *153*(6), 1175–1185. https://doi.org/10.1083/jcb.153.6.1175

Sahai, E., Wyckoff, J., Philippar, U., Segall, J. E., Gertler, F., & Condeelis, J. (2005). Simultaneous imaging of GFP, CFP and collagen in tumors in vivo using multiphoton microscopy. *BMC Biotechnology*, *5*, 1–9. https://doi.org/10.1186/1472-6750-5-14

Sánchez-Moreno, A., Guevara-Hernández, E., Contreras-Cervera, R., Rangel-Yescas, G., Ladrón-De-Guevara, E., Rosenbaum, T., & Islas, L. D. (2018). Irreversible temperature gating in trpv1 sheds light on channel activation. *ELife*, *7*, 1–11. https://doi.org/10.7554/eLife.36372

Siegel, R. L., Miller, K. D., Wagle, N. S., & Jemal, A. (2023). Cancer statistics, 2023. *CA: A Cancer Journal for Clinicians*, *73*(1), 17–48. https://doi.org/10.3322/caac.21763

Simonis, M., Klous, P., Splinter, E., Moshkin, Y., Willemsen, R., De Wit, E., Van Steensel, B., & De Laat, W. (2006). Nuclear organization of active and inactive chromatin domains uncovered by chromosome conformation capture-on-chip (4C). *Nature Genetics*, *38*(11), 1348–1354. https://doi.org/10.1038/ng1896

Solon, J., Levental, I., Sengupta, K., Georges, P. C., & Janmey, P. A. (2007). Fibroblast adaptation and stiffness matching to soft elastic substrates. *Biophysical Journal*, *93*(12), 4453–4461. https://doi.org/10.1529/biophysj.106.101386

Spill, F., Reynolds, D. S., Kamm, R. D. ., & Zaman, M. H. (2016). Impact of the Physical Microenvironment on Tumor Progression and Metastasis. *Curr Opin Biotechnol*,

40(1), 41–48. https://doi.org/10.1177/0022146515594631.Marriage

Strale, P. O., Azioune, A., Bugnicourt, G., Lecomte, Y., Chahid, M., & Studer, V. (2016). Multiprotein Printing by Light-Induced Molecular Adsorption. *Advanced Materials*, *28*(10), 2024–2029. https://doi.org/10.1002/adma.201504154

Talmadge, J. E., & Fidler, I. J. (2010). The Biology of Cancer Metastasis: Historical Perspective. *Cancer Res*, *70*(14), 5649–5669. https://doi.org/10.1158/0008-5472.CAN-10-1040.AACR

Théry, M. (2010). Micropatterning as a tool to decipher cell morphogenesis and functions. *Journal of Cell Science*, *123*(24), 4201–4213. https://doi.org/10.1242/jcs.075150

Théry, M., & Bornens, M. (2006). Cell shape and cell division. *Current Opinion in Cell Biology*, *18*(6), 648–657. https://doi.org/10.1016/j.ceb.2006.10.001

Théry, M., Racine, V., Pépin, A., Piel, M., Chen, Y., Sibarita, J. B., & Bornens, M. (2005). The extracellular matrix guides the orientation of the cell division axis. *Nature Cell Biology*, *7*(10), 947–953. https://doi.org/10.1038/ncb1307

Théry, M., Racine, V., Piel, M., Pépin, A., Dimitrov, A., Chen, Y., Sibarita, J. B., & Bornens, M. (2006). Anisotropy of cell adhesive microenvironment governs cell internal organization and orientation of polarity. *Proceedings of the National Academy of Sciences of the United States of America*, *103*(52), 19771–19776. https://doi.org/10.1073/pnas.0609267103

Tong, J., Qi, Y., Wang, X., Yu, L., Su, C., Xie, W., & Zhang, J. (2017). Cell

micropatterning reveals the modulatory effect of cell shape on proliferation through intracellular calcium transients. *Biochimica et Biophysica Acta - Molecular Cell Research*, *1864*(12), 2389–2401. https://doi.org/10.1016/j.bbamcr.2017.09.015

Totaro, A., Castellan, M., Battilana, G., Zanconato, F., Azzolin, L., Giulitti, S., Cordenonsi, M., & Piccolo, S. (2017). YAP/TAZ link cell mechanics to Notch signalling to control epidermal stem cell fate. *Nature Communications*, *8*(May), 1–13. https://doi.org/10.1038/ncomms15206

Vallotton, P., Danuser, G., Bohnet, S., Meister, J.-J., & Verhovsky, A. (2005). Tracking Retrograde Flow in Keratocytes: News from the Front. *Mol Biol Cell*, *16*(March), 1223–1231. https://doi.org/10.1091/mbc.E04

Vardhan, S., Yadav, A. K., Pandey, A. K., & Arora, D. K. (2013). Diversity analysis of biocontrol Bacillus isolated from rhizospheric soil of rice-wheat (Oryza sativa-Triticum aestivum L.) at India. *Journal of Antibiotics*, *66*(8), 485–490. https://doi.org/10.1038/ja.2013.10

Wang, Yejun, Nagarajan, M., Uhler, C., & Shivashankar, G. V. (2017). Orientation and repositioning of chromosomes correlate with cell geometry-dependent gene expression. *Molecular Biology of the Cell*, *28*(14), 1997–2009. https://doi.org/10.1091/mbc.E16-12-0825

Wang, Yuan, & Gilmore, T. D. (2003). Zyxin and paxillin proteins: Focal adhesion plaque LIM domain proteins go nuclear. *Biochimica et Biophysica Acta - Molecular Cell Research*, *1593*(2–3), 115–120. https://doi.org/10.1016/S0167-4889(02)00349-X

Zaidel-bar, R., Itzkovitz, S., Ma, A., Iyengar, R., & Geiger, B. (2007). *Functional atlas of the integrin adhesome*. *9*(8).

Chapter 2: Comparative profiling of cellular gait on adhesive micropatterns defines statistical patterns of activity that underlie native and cancerous cell dynamics.

John C. Ahn[1,2], Scott M. Coyle[1,*]

Affiliations:

[1]Department of Biochemistry

[2]Integrated Program in Biochemistry Graduate Program

University of Wisconsin-Madison, Madison, Wisconsin 53706, USA.

*Correspondence to: smcoyle@wisc.edu

Abstract

Cell dynamics are powered by patterns of activity, but it is not straightforward to quantify these patterns or compare them across different environmental conditions or cell-types. Here we digitize the long-term shape fluctuations of metazoan cells grown on micropatterned fibronectin islands to define and extract statistical features of cell dynamics without the need for genetic modification or fluorescence imaging. These shape fluctuations generate single-cell morphological signals that can be decomposed into two major components: a continuous, slow-timescale meandering of morphology about an average steady-state shape; and short-lived "events" of rapid morphology change that sporadically occur throughout the timecourse. By developing statistical metrics for each of these components, we used thousands of hours of single-cell data to quantitatively define how each axis of cell dynamics was impacted by environmental conditions or cell-type. We found the size and spatial complexity of the micropattern island modulated the statistics of morphological events—lifetime, frequency, and orientation—but not its baseline shape fluctuations. Extending this approach to profile a panel of triple negative breast cancer cell-lines, we found that different cell-types could be distinguished from one another along specific and unique statistical axes of their behavior. Our results suggest that micropatterned substrates provide a generalizable method to build statistical profiles of cell dynamics to classify and compare emergent cell behaviors.

Introduction

Dynamic behaviors of living systems, from the macroscale to the microscale, are powered through patterns of activity. For a walking human, alternating right-left sequences of pedal contact, arm swinging, and joint articulation produce an emergent walking gait that enables efficient locomotion(Cicirelli et al., 2022; Roberts et al., 2017). Similarly, at the single-cell level, patterns of actin polymerization, filament sliding, and other active processes can coordinate and collaborate to manipulate cell shape to orchestrate complex cell behavior such as phagocytosis or motility(Castellano et al., 2001; Cooper, 1991; Zemel & Mogilner, 2009).

At the molecular scale, metazoan cell migration and adhesion are regulated by signaling through *integrin receptors* that physically couple the binding of extracellular matrix ligands from the environment to the internal cytoskeleton(Bachmann et al., 2019; Holly et al., 2000). At the cellular scale, multiple integrin contact sites interface with the specific configuration of signaling networks, cytoskeletal structures and other molecular systems present in the cell to influence the migratory and adhesive behaviors that emerge(Juliano et al., 2004). This complex interplay between sensory inputs and the biological pathways that process them can cause different cells placed in identical environments to behave in distinct ways; and identical cells in different environments to respond with markedly different behaviors(Yu & Bagheri, 2020).

However, a quantitative or statistical understanding of the patterns of morphological activity—or “gait” — that occur within a given cell type and how those patterns are modulated by the environment are generally unclear. While mathematical and statistical treatments of gait are commonplace tools to explore such patterns in macroscale biology, where they have great utility in quantifying animal behavior and in

diagnosing orthopedic and ergonomic pathologies, these powerful methods are less often applied to single cells(Hofman et al., 2020). One reason for this has been an emphasis on first identifying the specific molecular components and biochemical mechanisms that give rise to motility in these systems. A second reason is that the morphology of many cells, in particular adherent metazoan cells, lacks the stereotyped anatomy that is commonly used to perform such analyses(Marcon et al., 2011). That is, while the arms, legs, feet and joints of a human provide concrete and trackable points to build up a description of gait, an adherent metazoan cell's geometry and sub-cellular anatomy can be vague or rapidly reconfigurable **(Fig. 1A)**.

Indeed, the most successful instances of applying gait analysis to single cells so far have either been done on protozoan cell-types with easily scored sub-cellular anatomy and structure; or cells undergoing such highly stereotyped and reproducible migration that the cell geometry is stable enough for such treatment, such as in migrating fish keratocytes(Coyle et al., 2019; Hums et al., 2016; Keren et al., 2008; Larson et al., 2022; Marques et al., 2018). Given the utility of gait analysis for macroscopic biological systems, a general method for performing gait analysis on morphologically plastic metazoan cells would be valuable, as the dynamic behaviors of such single cells provide the foundation of multicellular processes like development, wound healing, and immune responses, and aberrant migration and adhesion contribute to developmental disorders, metastasis, bleeding pathologies, and autoimmunity(Bravo-Cordero et al., 2012; Grada et al., 2017; Luster et al., 2005; McManus & Golden, 2005; Scarpa & Mayor, 2016; Trepat et al., 2012; Vesperini et al., 2021).

Here we develop a general strategy for comparative profiling of cellular gait across different metazoan cell-types and environmental INPUTs. Our strategy is based on quantifying the long-term morphology dynamics of cells grown on different cell-sized micropattern islands of the adhesive ligand fibronectin **(Fig. 1B)**(Brückner et al., 2019). We find that cells grown on such adhesive micropatterns adopt a steady-state cell geometry in the time-average, but also display shape fluctuations over time about that mean geometry. We develop a computational strategy to digitize these cell morphology dynamics and map them to a polar coordinate (**r,**θ) system to produce morphological signals for quantitative analysis. Inspection of these signals suggests a natural decomposition into short timescale "events"–bursts of highly dynamic activity–and slower timescale meandering in shape variation. We develop specific quantitative and statistical metrics to describe these features and use these to build statistical profiles for specific cell types based on hundreds of thousands of unique measurements in response to a wide range of pattern INPUTs. This allowed us to classify behavior modulation induced by the environment in specific cell lines and identify specific axes of cell behavior that distinguish different cancer cell lines from one another. Because our approach relies only on non-fluorescent imaging of single cells and does not require genetic modification, we anticipate our method may be particularly well-suited to build statistical profiles of cellular gait in rare cell populations or patient-derived samples. Long term, the extension of gait-analysis to metazoan single-cell biology could open up new avenues for clinical diagnostics and guide behavior-informed therapeutic intervention.

Results

Cells grown on adhesive micropatterned islands exhibit fluctuations about a steady-state geometry that generates a dynamic morphology signal

Because cells are active systems, they continue to generate dynamics even when biased towards a particular steady-state geometry. To explore the kinds of morphology signals individual cells generate under such conditions, we used DIC microscopy to continuously image individual 3T3 fibroblasts adhered to cell-sized micropatterned islands of fibronectin **(Fig. 1C-E and Fig. S1)**. This approach allowed cell morphology to be easily scored at high temporal resolution (2 frames per minute) without the need for phototoxic fluorescence imaging to be used, enabling timelapse recordings greater than 12 hours to be readily collected for individual cells.

The time average of the image stack for an individual cell's time series revealed an overall shape resembling the convex hull of the underlying micropattern **(Fig. 1D)**. These time-average shapes resemble the population-average shapes seen when one aligns and averages thousands of different cells grown on separate patterns together(Théry, 2010; Théry, Pépin, et al., 2006; Théry, Racine, et al., 2006). However, at any moment in time, a cell was often found to be adopting a geometry that deviated substantially from this time-average shape. For example, while a cell grown on a four-leaf clover island had a diamond-like time average that contacted all four lobes of the pattern, that same cell was observed in shapes with 3-points of contact, shapes that appeared to be polarized between lobes, as well as shapes nearly identical to the time average itself (**Fig. 1E**). Similar phenomena were observed for other micropatterned islands that varied in size or spatial complexity **(Fig. S1)**. These data indicate that while an adhesive

micropattern biases the cell to a specific cell geometry, spontaneous cellular activity leads to excursions that drive the cell away from this attractive basin.

Digitization of morphological signals reveals short and fast timescales underlying cell behavior and defines statistical metrics for analysis

The shape fluctuations we observed for individual cells adhered to micropatterns invite a more detailed and quantitative analysis. Because micropatterned islands are on the order of the size of the cell itself, both the cell geometry and the pattern are well suited to a description in polar coordinates. Thus, we adopted an approach wherein we digitized cell shape for every frame in the recording by calculating the distance **r** from the center of the pattern to the edge of the cell for every angle θ between 0 and 360 degrees **(Fig. 2A)**. This maps the time-dynamics of the cell shape from an inconvenient cartesian (**x**, **y**) form into an (**r**,θ) "morphological signal". This (**r**,θ) version of the signal is particularly convenient as it is easy to align across individual cells and facilitates the application of many visualization and statistical techniques to interrogate the content of the signal.

Close inspection of a representative morphological signal from a 3T3 cell grown on a 30μm wide k2 micropattern suggests several axes to quantify and unpack in our analysis. First, the cell's morphology signal can be unwrapped and displayed as a kymograph, providing an intuitive visualization of how a cell's shape fluctuations are distributed in both space and time during the experiment **(Fig. 2A)**. For the representative 3T3 signal, we observe a structure in which discrete "events"–bursts of localized spatiotemporal activity–occur periodically throughout the signal. In between events, the cell's shape continues to fluctuate but with much lower amplitude and without obvious

biases in its spatiotemporal character. This suggested that a cell's morphology signal can be at least partially decomposed into two different components: 1) a description of the statistical properties of the 'events'; and 2) a description of the global and inter-event shape fluctuations.

To create metrics for characterizing the "events" within a cell's morphological signal, we directly mined features of the kymograph itself **(Fig. 2B)**. For any individual event, we defined an associated duration, amplitude, orientation, and width for that event **(Figure 2C-D)**. Moreover, because multiple events are observed within a single morphological signal, individual events and their appearance over time can be used to define an event density (events/hour) and associated average inter-event time as well.

To quantitatively characterize the morphological dynamics between events, we also inspected and analyzed the distribution of variation about the cell's mean shape. For any observed shape vector, the difference between that shape and the time-average shape defines a residual shape **(Fig S2)**. By aggregating these residuals across all timepoints and inspecting their distribution across θ values, we observed that the bulk of observations generally fell within an envelope of values about the mean shape **(Fig. 2E)**. To determine what sorts of shape vectors best described these fluctuations, we used principal component analysis (PCA) to identify a set of 8 shape modes that could explain >70% of the variance **(Fig. S2)**. Mapping these shapes from ($\mathbf{r}$,θ) back to the lab reference-frame revealed that the modes we recovered appeared to naturally correspond to conjugate pairs of Fourier shape modes **(Fig. 2F)**. Generally, the lowest frequency modes explained the greatest proportion of the variance, describing simple polarization of the mean shape, with higher frequency modes playing a minor role that allows for more

complex geometries **(Fig. 2G)**. This universal collection of shape modes can be used to describe the shape fluctuations about a cell's steady-state geometry on any pattern or for any cell type **(Fig. S2)**.

Using these two descriptors, we can begin to see how an individual cell's morphological signal emerges as an interplay between these fast events and slower timescale shape fluctuations. For the representative 3T3 cell, plotting the magnitude of the first conjugate pair of shape modes (here termed α) over time provides a 1-dimensional timeseries approximating the cell's morphology dynamics **(Fig. 2H)**. Large spikes in the magnitude of the α parameter coincided with events seen in a cell's morphology kymograph **(Fig. 2H and Fig. S2)**. This suggested that the discrete events are a large contributor to the overall shape variation observed during the timecourse. Thus, we compared the distribution of α values during burst events to the distribution of α values occurring outside the events. Indeed, this partitioning revealed a low-magnitude α distribution outside of events, and a higher right-shifted magnitude for the α distribution within events **(Fig. 2I and Fig. S2)**. As such, the relative contribution of the two α distributions to the overall variation provides another useful metric for describing the underlying structure of a cell's morphological signal.

Having developed a strategy for digitization of a cell's morphology signal and having defined metrics to classify different discrete (structure of events) and continuous (α distributions) elements of its behavior, we will now begin to apply these quantitative tools to ask how a cell's morphological signal is affected by environmental inputs or underlying cell-type.

The spatial structure of a micropattern island modulates the statistics underlying a cell's morphological signal and emergent behavior

The preceding section developed a pipeline for digitizing cell dynamics on micropatterned islands and associating quantitative metrics and statistics with the resulting emergent morphological signal. A natural question that arises is how the morphological signal that we observe is affected by the underlying structure of the micropattern island itself. Because micropatterning allows manipulation of the spatial structure of the fibronectin INPUT to the cell at micron length-scales, it is straightforward to construct patterns that emulate different environmental features a cell might experience naturally, such as the overall availability of ligand or the number of polarization directions available. Thus, we mathematically generated a family of micropatterned fibronectin island INPUTs using the polar equation for the harmonics of a circle ($r = d + a \cdot cos(k\theta)$), which systematically allowed us to sample different size (radius parameters, defined by *a* and *d*) or spatial complexities (*k*, number of petals). This family of patterns was well suited to our analysis as the structure of the pattern is defined in the same polar coordinate system that we use to describe the cell shape itself, allowing us to look for correlations between pattern structure and cell behavior **(Fig. 3A)**.

We prepared adhesive fibronectin micropatterns based on a matrix of 4 different radii (30,40,50,60 μm) and 4 different spatial complexities (k-values 2, 3, 4 and 5), performed extended timelapse imaging of 3T3 cells grown on each pattern, and digitized their morphological signals for analysis. Our 3T3 dataset contained a total of 238 cells, spanning 107,382 minutes, for a total number of 196,949 unique observations across the matrix. Because we acquired signals for multiple cells grown on each micropatterned

INPUT, the statistical features of their resulting signals could be pooled to generate high credence descriptors of the observed behaviors.

Using the pipeline developed in the previous section, we first asked how the nature of fast-timescale morphological “events” were affected by the geometry of the pattern INPUT. We immediately noticed that the overall event density (number of events/hour) differed dramatically across the panel of INPUTs. For example, cells grown on 40 micron patterns had a very low event density–less than 1 event per hour in some cases; while in contrast, cells grown on larger, more-spatially complex patterns (e.g. 60 um k4 and k5) had much larger event densities, greater than 10 per hour in some cases **(Fig. 3B-C and Fig. S3)**. Thus, the geometry of the adhesive micropattern appeared to be giving rise to markedly different behaviors in the 3T3 cells.

To unpack these observations further, we more closely inspected how specific statistical features of these morphological events changed as a function of size and spatial complexity. To help compare the changes we observed, we used the statistics we collected from cells grown on 30 um k2 patterns as a reference point. The associated raw data and raw metrics, which provide a complementary view into this analysis, are included in Fig. S3. With respect to “event density”, we observed an initial small dip in density as cells moved from 30 um to 40 um patterns (k2,3,4,5 Welch p-values = <0.01, 0.20, 0.01, 0.03), before increasing as the radius increased to 50 (k2,3,4,5 Welch p-values = 0.39, 0.04, 0.25, 0.13) and then 60 um (k2,3,4,5 Welch p-values = 0.16, 0.32, <0.01, 0.11) **(Fig. 3C-D)**. This trend held regardless of the underlying spatial complexity (k-value) of the pattern, although the increase was more pronounced for patterns with high k-value compared to those with lower k-value. This check-mark shaped response to pattern

radius we observed appears to qualitatively agree with the extent to which 3T3 cells were able to fully spread across the micropattern: on 30 micron patterns most cells were incompletely spread; on 40 micron patterns most cells were fully spread with little remaining micropattern available to adhere to; and on 50- and 60-micron patterns, cells were fully spread but with additional adhesive surface available to explore or sample.

In addition to event density, we observed that the nature of the pattern (radius and spatial complexity) modulated statistical features of individual events themselves. With respect to radius, the average lifetime of events was longest for 50 micron patterns (k2,3,4,5 Welch p-values = <0.01, <0.01, <0.01, <0.01; compared to the 30 um k2 distribution), followed by 40 micron (k2,3,4,5 Welch p-values = 0.32, <0.01, 0.08, <0.01; compared to the 30 um k2 distribution), 60 (Welch p-values = <0.01, 0.09, <0.01, 0.10; compared to the 30 um k2 distribution) micron and finally the shortest-lived events for 30 microns (k2,3,4,5 Welch p-values = n.a., 0.55, 0.37, 0.50 compared to 30 um k2) **(Fig. 3E-F)**. The span parameter of these events—how wide the morphological extension was—varied substantially across the different patterns, with 40 micron patterns inducing significantly narrower event excursions (k2,3,4,5 Welch p-values = <0.01, <0.01, <0.01, <0.01; compared to the 30 um k2 distribution) compared to 30,50, or 60 micron patterns **(Fig. 3G-H)**. These results mirror our earlier observation that 3T3 cells are more event-dense when incompletely spread (30 micron) or have excess adhesive ligand available (50 and 60 microns). Effects of a pattern's spatial complexity on these event statistics were less obvious, but still detectable in some cases. For example, higher k-value patterns (more petals) were generally associated with shorter lived events. However other

parameters like the “span” of the pattern were not obviously influenced by the k-parameter.

Given these observations, we wondered whether the spatial structure of the pattern might have stronger influence on the spatial orientation of events as opposed to their general features. To explore this, we projected the orientation of an event (defined as the θ values associated with the span of an event) onto the underlying structure of the micropattern to create a histogram for visualizing event alignment **(Fig. 3I-J)**. Inspection of these histograms qualitatively suggested that, for cells with high event densities, the events were more spatially aligned with the micropattern as the size of the pattern increased and the spatial complexity decreased.

To analyze this quantitatively, we computed an alignment score based on event centroid angular overlap with the underlying micropattern and binned the scores for each pattern together **(Fig. 3I-J)**. Because the 40 micron patterns induced very few events, their alignment scores were too low confidence and were excluded from detailed analysis. Nonetheless, a clear trend towards better event/pattern alignment was observed for increasing pattern radius (k2 at 50μm, k3 at 50μm, k2 at 60μm, k3 at 60μm Welch p-values = <0.01, <0.01, 0.05, 0.09; compared to the 30 um k2 distribution). Moreover, a decrease in alignment score was observed as the spatial complexity of the pattern increased. An intuitive hypothesis for the interpretation of these data is that a cell’s ability to effectively orient along a micropattern reflects a sort of spatial resolution inherent to the cell. That is, events become better oriented if an open area of adhesive ligands is large enough to polarize along, and the combination of spatial complexity and pattern radius determines whether or not that area requirement is being satisfied. By probing both radius

and spatial complexity independently, our micropatterning assay was able to identify this inflection point for the 3T3 cells, which could be different depending on cell-type or cell physiology.

Finally, we examined how the statistics describing cell behavior *between* events—that is slow-timescale meandering—was affected by the micropattern. Using our universal collection of PCA shape modes **(Fig. 2F and Fig. S2)**, we fit our observations and decomposed the global α parameter distribution associated with each micropattern INPUT into its associated event and non-event distributions **(Fig. 3K-3L)**. We found that although the event α distribution differed considerably across different pattern INPUTs—which makes sense given the differences in event statistics we described above—we observed only very minor differences to the inter-event α distribution. That is, for the 3T3 cells we inspected, the statistics describing the slow timescale meandering behavior between events were generally similar regardless of the pattern tested.

Taking together, our query of 3T3 behavior across a range of different micropatterned INPUTs suggests that the structure of the micropattern INPUT largely modulates the event, but not inter-event, statistics underlying the cell's emergent morphology signal. Properties such as event lifetime, frequency, span, and orientation are affected by the nature of the pattern, with size (pattern radius) appearing to play a larger role than spatial complexity (petal number). In contrast, the overall morphological fluctuations and shape meandering occurring between these events was not strongly affected. Thus, using adhesive micropatterns, we can build a statistical profile that captures a given cell-type's response to a range of different environmental INPUTs.

Profiling cancer-cell lines on micropatterned islands identifies different statistical axes associated with divergent morphological signals and cell dynamics

The preceding section demonstrated that a single cell-type can display a complex set of morphological responses to a defined set of structured micropattern INPUTs, and that these differences can be used to build a statistical profile for how pattern INPUTs are mapped into morphological signal OUTPUTs. Given this, we next wondered whether our assay could be used to profile different cell-types for comparison, and whether we could identify specific statistical axes defining the key differences underlying divergent behaviors between cell-types. To this end, we selected four cell lines—Hs578t, BT549, MDA-MB-436, and MDA-MB-231—from an established panel of triple negative breast cancer cell lines with mesenchymal or luminal morphology for investigation(Lehmann et al., 2011). Some of these lines, such as MDA-MB-231, have been previously noted for their high levels of aberrant motility and are frequently termed “hyper-metastatic” in the literature(Sun et al., 2016).

We performed extended timelapse imaging for each cell line grown on adhesive fibronectin micropatterns with a radius of 50 microns and 4 different k values (petal numbers 2, 3, 4 and 5) **(Fig. 4A)**. This subset showed a good range of statistical diversity in the 3T3 experiments, making it a natural starting point for comparison across different cell lines. Single-cell morphology signals were digitized as before, and signals from pattern-matched cells and cell-lines were binned for statistical analysis **(Fig. 4B)**. In parallel we analyzed 3T3 cells grown on identical conditions to use as a non-cancerous “out-group” reference cell-line for comparison. Our cell panel dataset contained a total of 396 cells, spanning >218,000 minutes, for a total number of >247,000 unique

observations across the matrix. The associated raw data and statistics have been included in Fig. S4. Different cancer-cell lines from the panel exhibited obvious qualitative differences in behavior **(Fig. 4B)**. For example, the morphology signal kymographs for MDA-MB-231 had high levels of fast timescale activity, while MDA-MB-436s often exhibited extended periods of slow activity.

Similar to our earlier analysis of the 3T3s, we used our quantitative statistical metrics for describing events and global shape variation to unpack the differences in morphological behavior for the different cancer-cell lines across specific parameters. We found that although all of these cell lines were associated with metastatic breast cancer, they could be distinguished from one another on the basis of specific statistical metrics that were uniquely affected within each line. For some cell lines, these differences manifested specifically in the nature of the statistics of fast timescale events. For example, MDA-MD-436 cells had unusually long events (k2,3,4,5 Welch p-values = 0.021, <0.01, <0.01, 0.186; compared to 3T3 30 um k2 distribution) and high inter-event waiting times (k2,3,4,5 Welch p-values = <0.01, <0.01, <0.01, <0.01; compared to 3T3 30 um k2 distribution), meaning that events occurred less frequently but each event was markedly longer in duration **(Fig. 4C-F)**. In another example, we found that while some cell-lines produced larger “span” events for certain k-value patterns, BT549 cell lines were unique in that they produced events with significantly larger “span” than the other cell lines across all k-values tested (k2,3,4,5 Welch p-values = <0.01, <0.01, <0.01, <0.01; compared to 3T3 30 um k2 distribution) **(Fig. 4G-H)**. This means that the nature of the BT549 events makes them statistically wider and bulkier on average than any of the other cell-lines we examined.

In other cases, global and inter-event statistical descriptors, like the α parameter distribution, could capture differences between cell lines. For example, MDA-MB-231s had a significantly higher average non-event α parameter than any of the other cell lines we examined (k2,3,4,5 Welch p-values = <0.01, <0.01, <0.01, <0.01; compared to 3T3 30 um k2 distribution) **(Fig. 4K-L)**. This means that MDA-MB-231s have a greater baseline shape variation than the other cell-lines tested, even when no events are occurring. Indeed, while MDA-MB-231s often had fewer and shorter events than other cell-lines (k2,3,4,5 Welch p-values = <0.01, <0.01, <0.01, <0.01; compared to 3T3 30 um k2 distribution), they nonetheless had the highest overall shape variation of any cell line we inspected. Interestingly, when MDA-231s did perform events, they generally polarized the cell strongly along the orientation of the micropattern structure (k2,3,4,5 Welch p-values = 0.02, 0.04, 0.813, 0.05; compared to 3T3 30 um k2 distribution) **(Fig. 4J)**. Thus, the statistical profile of MDA-MB-231s that emerges is one in which a high level of steady-state shape fluctuation is punctuated by highly polarized events. These observations are consistent with the behavior of MDA-231s grown on narrowly-connected two-island patterns[24], where they exhibit large shape fluctuations and high rates of translocation between the two islands.

Taken together, our results indicate that the morphology signals emitted by different cell-lines grown across different micropatterned INPUTS can generate statistical profiles that can be used to describe and distinguish the behaviors of different cell types. Although all the cells tested were derived from malignant triple-negative breast cancers, the statistics underlying their dynamic morphologies could nonetheless be markedly different. These differences manifested not only as changes in magnitude of some

common statistics, but also in terms of which parameters were specifically affected, and even in terms of which timescales (fast events versus slow meandering) were affected. We hypothesize that the underlying internal configuration inherent to each cell-type we tested can manifest as changes to a specific statistical axis underlying a cell's morphology signal, and careful analysis of these signals can identify the specific axes that are changed.

Discussion

Here, we have used cell-sized adhesive micropatterns as a platform for building statistical profiles describing the patterns of activity underlying a cell's emergent dynamics. We found that by biasing the cell's steady-state shape to a specific geometry, micropatterns provided a straightforward way to digitize the shape fluctuations about this steady-state shape for statistical analysis. By mapping these dynamics onto a polar coordinate description, we could treat a cell's morphology signal as a kymograph in the ($\mathbf{r}$,θ) reference frame and analyze its content in this space. This revealed a natural partitioning of the dynamics into short-timescale discrete "events" and a slower timescale meandering of shape between these events. We developed a set of metrics to describe the statistical features of these fast morphology events (event frequency, lifetime, span, alignment) and inter-event shape fluctuations (PCA-derived alpha distributions).

We used these metrics to ask how morphological signal was affected by the geometrical features of the pattern INPUT, using 3T3s as a test cell line. This revealed that 3T3 *event* statistics were strongly modulated by different INPUT patterns, but that the baseline shape fluctuations and global meandering were generally unaffected. We then extended this approach to build statistical profiles for members of a panel of triple-

negative breast cancer cell lines. This revealed that different metastatic breast cancer cell lines could exhibit aberrant dynamics with markedly different statistical underpinnings. For example, MDA-MB-231s showed large shifts to its global shape variation parameters, whereas MDA-MB-436s were largely defined by changes to the event structure, producing much longer and more infrequent events. Thus, our method provides a means by which the statistical features of single-cell behavior can be efficiently digitized, aggregated, and compared for analysis.

The approach we take here treats the emergent behavior of a cell–the dynamics to its shape envelope–as an OUTPUT arising from an extraordinarily complex set of internal molecular processes that can react to specific features of the pattern INPUT. By choosing metrics which are based on DIC microscopy and not rooted in fluorescence-based signals or detailed molecular markers, our approach avoids phototoxicity and can yield timeseries data constrained only by interference from cell-division events. In this way, our approach may be especially useful for building statistical profiles of cell-lines when only a small number of cells are available, or genetic modification is infeasible or unwanted; for example, in patient-derived samples or rare populations of primary cells.

At the same time, the lack of molecular detail explaining the biochemical origin for the statistical phenotypes we observe at present limits the scope of our interpretation of these data. For example, what is the molecular basis for longer event lifetimes in some cells versus changes to global shape fluctuation seen in others? While many specific hypotheses could be possible, such as RhoGEF activity(Pascual-Vargas et al., 2017; Rossman et al., 2005), integrin expression level and repertoire(Barczyk et al., 2010; Seetharaman & Etienne-Manneville, 2018), or metabolite availability and usage(Choo et

al., 2023; D'Anselmi et al., 2011), the number of genomic differences between the different cell lines we inspected is too great to pinpoint any specific cause at this stage(Kim et al., 2016; Vandin et al., 2011). However, the approach we have developed here will be well-suited to future studies aimed at identifying specific molecular drivers to each statistical axis we identify. For example, a CRISPRi/a screen(Bock et al., 2022; Doench, 2018) in an otherwise isogenic cell-line could be used to identify genes whose dysregulation is associated with higher rates of shape fluctuation, longer event lifetimes, or greater event frequencies.

Long-term, we anticipate this approach could be used to map statistical profiles built based only on morphology dynamics to an associated set of genetic legions that are commonly associated with that aberrant phenotype. Such knowledge could help pinpoint specific causal drivers of metastasis operating in patient-derived cell-lines that are often not immediately obvious from a catalog of genome mutations(Riquet et al., 2017; Urbach et al., 2012; Zhang et al., 2018). As such, a cell's own dynamic behavior may, through its statistics, have the potential to report out the anomalies and pathologies lurking within.

Acknowledgements.

We thank members of the Coyle Lab and Weeks Lab for advice, helpful discussions, and critical reading of the manuscript. Funding: This work was supported by a David and Lucille Packard Fellowship for Science and Engineering (SMC) and an NIH DP2 New Innovator Award (1DP2GM154329-01). Author contributions: JA and SMC conceived the overall project. The experimental plan was implemented by JA, and SMC. JA collected all

the data in the paper. JA and SMC prepared the figures and wrote the manuscript. SMC supervised all aspects of the work. Competing interests: None.

Experimental Procedures

Micropatterning. We employed the light-induced molecular adsorption (LIMAP) method for micropatterning (Strale et al., 2016). 35mm Glass bottom petri dishes (MatTek P35G-1.5-20-C) were exposed with oxygen plasma in preparation for passivation. For adsorption of the anti-fouling coating agent, 0.1 mg ml^{-1} PLL(20)-g[3.5]-PEG(2) (SuSoS CHF9,600.00) solution was added for 1 hour. The dish was washed five times with Milli-Q purified water. A 1:5 ratio of PLPP photoinitator gel to 70% ethanol (Alveole) was added to the microwell and dried at room temperature for 1 hour. To create the micropatterns, the well was exposed to UV light at a dosage of 30mJ mm^{-2}, and excess gel was washed away with 5 Milli-Q purified water washes and 5 Dulbecco's Phosphate Buffered Saline (DPBS) solution (VWR L0119-0500) washes, with the last volume of DPBS left to incubate for 5 minutes to rehydrate the substrate. The wells were then incubated with 10µg ml^{-1} fibronectin (Sigma-Aldrich F1141-5MG) and 10µg ml^{-1} NeutrAvidin (Invitrogen 84607) for five minutes and then washed 5 times with DPBS. PEGs were added at 0.1 mg ml^{-1} for another 1 hour incubation before being finally washed with water for 5 times.

Cell culture. 3T3 mouse fibroblast cells (ATCC CRL-1658) were cultured in Dulbecco's Modified Eagle's Medium (DMEM) (Sigma-Aldrich D6429) with 10% fortified calf bovine serum (Cytiva Life Sciences SH30396.03) and 1% penicillin-streptomycin (ThermoFisher 15140122). Cells were grown in a 5% CO_2 incubator at 37ºC up to 90% confluence before

being washed and passaged. Adherent cells were washed with PBS at each passage and detached from the flask surface by incubating with TrypLE (ThermoFisher Scientific 12604021) for 5-10 minutes at 37ºC. TrypLE was quenched with fresh DMEM media, and cells were resuspended and plated into new flasks with fresh DMEM. The following breast cancer cell lines were all cultured in DMEM with 10% fetal bovine serum (Fisher Scientific SH30396.03) and 1% penicillin-streptomycin in a 5% CO_2 atmosphere at 37ºC: MDA-MB-231 (ATCC HTB-26), MDA-MB-436 (ATCC HTB-130), Hs 578T (ATCC HTB-126), and BT-549 (HTB-122).

Microscopy. Measurements were obtained in time-lapse mode for up to 16 hours on a Nikon Eclipse Ti2 microscope. Throughout the measurements, samples were incubated in a Tokai Stage Top Incubator that maintained a temperature of 37ºC and an atmosphere of 5% CO_2. Bright-field images were acquired every 30, 40, or 60 seconds.

Image analysis. Custom python scripts for specific image-analysis workflows are outlined below.

Encoding polar descriptions of cell outlines. Binary masks of the cells were calculated using a canny filter from python OpenCV packages. The center point of each cell was identified, from which a 360º radial sweep was conducted, resulting in a 2D array of pixel intensities for each surveyed degree along the length of the pixel survey radius. From each surveyed 1D array of pixel intensities, the radius of the cell outline was calculated

based on a 95% threshold in which 95% of all the pixels with maximum intensities were located.

Kymograph analysis. 2D arrays of cell radii along theta values were collected for each point of time for each cell over the length of their microscopy time course. Heatmaps of these arrays were generated using the matplotlib.pyplot package, from which contours were identified using OpenCV packages. These contours were identified as morphological events and used to calculated parameters such as event frequency, lifetime, span, and more.

Principal component analysis. Deviations from the rolling mean value for each cell at each frame of time were collected for all the experimental conditions from the 3T3 cell experiments. These were compiled and used to calculate the shape modes using principal component analysis. The shape modes were then used to calculate scalar weights fits based on the cell outline radii.

Figures

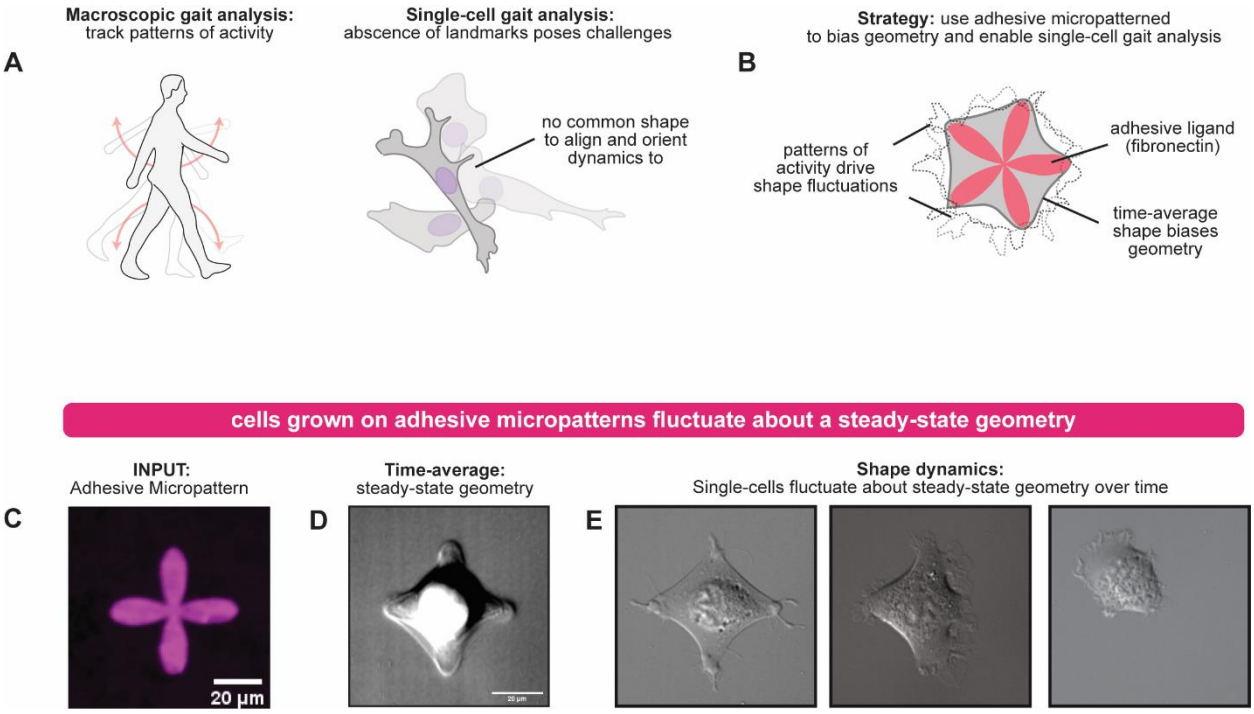

Figure 1. Cells grown on adhesive micropattern islands undergo dynamic shape fluctuations about an average cell shape.

(a) Schematic for how gait analysis is used to track patterns of activity in macroscopic biological systems but is difficult to extend to metazoan cells owing to a lack of landmarks and stereotyped geometry.

(b) Schematic for strategy of using adhesive micropatterns to bias cell geometry into a configuration suitable for single-cell shape analysis.

(c) Fluorescence microscopy image of a fibronectin adhesive micropattern used as a substrate for single-cell gait analysis. The intensity indicates the position on the substrate where the fibronectin ligand has adhered.

(d) Time-average image produced from an image stack of a 3T3 cell grown on the adhesive micropattern in (c) over a 12 hours period.

(e) Representative images from the time-series used to produce the time-average in (d). The cell geometry is observed to fluctuate substantially from the time-average shape throughout the timecourse.

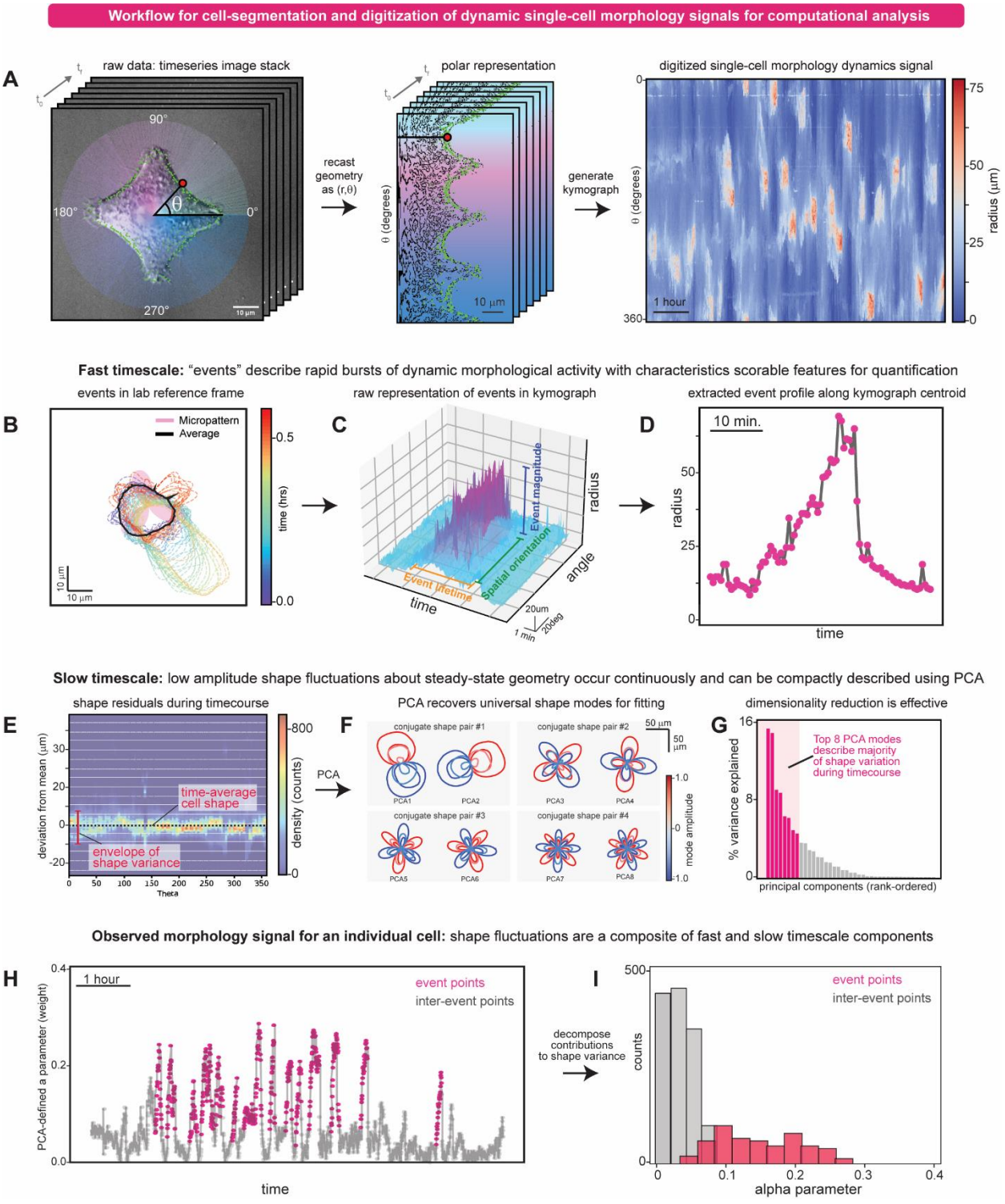

Figure 2. Digitization of single-cell morphology signals defines statistics for fast and slow timescale contributions to shape dynamics. Blablablabla.

(a) Workflow for digitization of cell morphology signals generated by cells grown on adhesive micropatterns, as applied to a representative cell. Using the center point of the micropattern as an origin, the cell shape is mapped from cartesian coordinates to an r,q description that describes the cell's radius at each possible angle from 0-360 degrees. By performing this for each image in the time-series, a compact description of the cell's geometry over time is obtained. The content of these timeseries can be intuitively viewed as a kymograph, which shows bursts of dynamic activity we term 'events', within the cell's morphological signal.

(b) Visualization of a single "event" from the kymogrpah shown in (a), showing the contour of the cell over time. For this event, it clearly corresponds to a large extension of the cell geometry followed by retraction.

(c) Structure of the event from (b) using the kymograph as a reference point. In the r,q reference frame the events appears as a burst of activity with an easily scored lifetime, amplitude, and orientation.

(d) Two-dimensional representation of the profile of the event from (c) by projecting the data along its central angle.

(e) Two-dimensional histogram depicting the distribution of shape residuals (observed shape – mean shape) for the cell from (a). Most observations fall within a 10 micron envelope about the cell's steady state geometry.

(f) Real-space depictions of the top 4 conjugate pair shape modes obtained by performing PCA analysis on the data in (e). Colors depict the effect on shape arising by adding (red) or subtracting (blue) the weighted shape mode from the average shape. Note that the PCA-derived shapes correspond to increasingly higher-order Fourier shape modes (1,2,3,4 order depicted).

(g) Histogram showing the percentage of shape variance explained by each individual shape mode obtained by PCA decomposition of the data in (e). The top 8 shape modes describe >80% of the observed shape variance in the dataset and were selected to use for weight calculation, fitting, and dimensionality-reduction.

(h) 1-dimensional representation of the morphological signal from (a) using only the weight amplitude (denoted as α) for the first conjugate pair of shape modes in (f). Points colored in pink correspond to time points associated with “events” from the kymograph in (a). Note that high amplitude shape mode usage appears to correspond to when events occur.

(i) Partitioning of the overall distribution of α values from (h) into “event” and “inter-event” timepoints. Inter-event distributions have low α values compared to a right-shifted distribution for the event distribution.

Profile statistics of morphology dynamics within a cell line for different geometries of adhesive micropatterned island

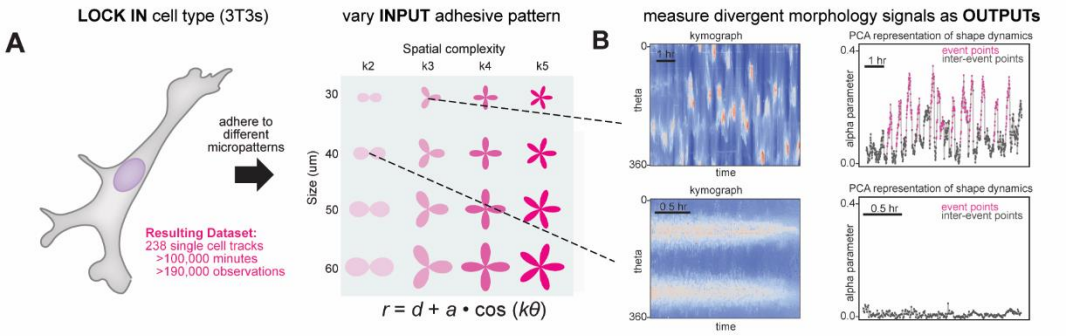

Fast timescale: how are *event statistics* modulated by the underlying geometry of the micropattern island?

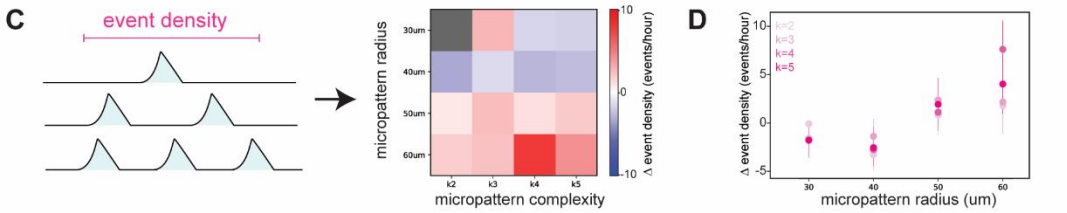

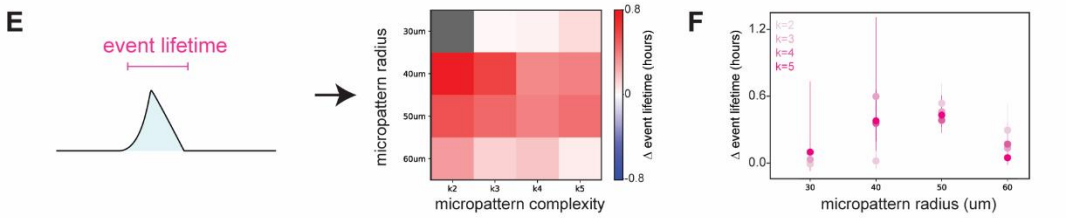

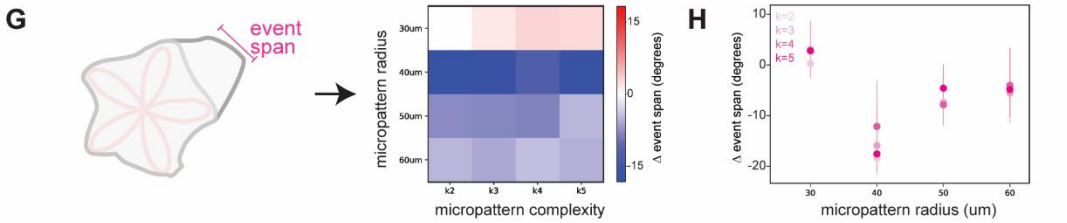

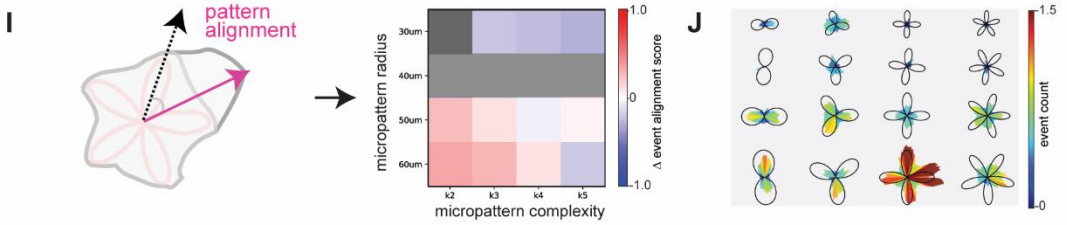

Slow timescale: how is global shape fluctuation modulated by the underlying geometry of the micropattern island?

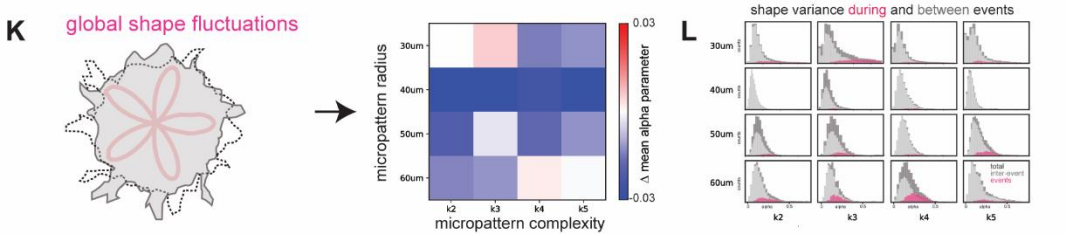

Figure 3. The spatial structure of a micropattern island modulates the statistical features of a cell's dynamic morphology signal.

(a) Schema depicting experimental design for interrogating effects of micropattern geometry on 3T3 morphology signals. 3T3 cells were imaged on different micropatterns defined by the harmonics of a circle, such that the spatial complexity and radius of the pattern were independently controlled. The resulting single-cell tracks were digitized for analysis using the workflow from Fig. 2 and aggregated by INPUT pattern for statistical comparison between different conditions.

(b) Examples of divergent morphological signals (presented both as kymographs and α time courses) observed when 3T3 cells were grown on different micropattern substrates. Top: a highly dynamic morphological signal observed from a cell grown on a 30um k3 pattern. Bottom: a cell with very little dynamic content from a cell grown on a 40 um k2 pattern.

(c) Relative "event density" statistics across the panel of INPUT patterns, using the 30 um k2 pattern as the reference for comparison by the "shared control bootstrapping" method.

(d) Plot of the data in (c) showing the trends observed when micropattern radius is varied for each level of spatial complexity (k2, k3, k4, k5). Values and error bars derived using the "shared control bootstrapping" method (see also Fig. S3).

(e) Relative “event lifetime” statistics across the panel of INPUT patterns, using the 30 um k2 pattern as the reference for comparison by the “shared control bootstrapping” method.

(f) Plot of the data in (e) showing the trends observed when micropattern radius is varied for each level of spatial complexity (k2, k3, k4, k5). Values and error bars derived using the “shared control bootstrapping” method (see also Fig. S3).

(g) Relative “event span” statistics across the panel of INPUT patterns, using the 30 um k2 pattern as the reference for comparison by the “shared control bootstrapping” method.

(h) Plot of the data in (g) showing the trends observed when micropattern radius is varied for each level of spatial complexity (k2, k3, k4, k5). Values and error bars derived using the “shared control bootstrapping” method (see also Fig. S3).

(i) Relative “pattern alignment” statistics for an event across the panel of INPUT patterns, using the 30 um k2 pattern as the reference for comparison by the “shared control bootstrapping” method.

(j) Plot of the data used to generate (i) projected onto the underlying shape of the micropattern for direct visualization of event-to-pattern alignment.

(k) “Global shape fluctuation” statistics (from α distributions) across the panel of INPUT patterns, using the 30 um k2 pattern as the reference for comparison by the “shared control bootstrapping” method.

(l) Partitioning of the overall distribution of α values from (k) into “event” and “inter-event” timepoints across the panel of different INPUT patterns.

Use morphological signals derived from adhesive micropatterns to define statisticals axes that distinguish cancer lines

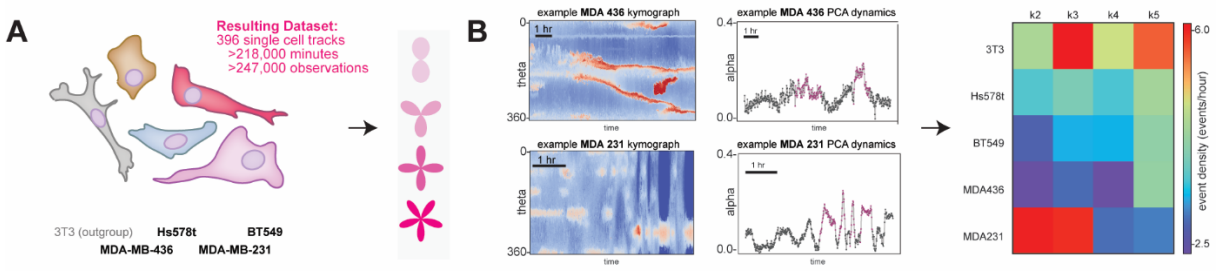

Fast timescale: how are *event statistics* modulated by the underlying internal configuration of a cancer cell line?

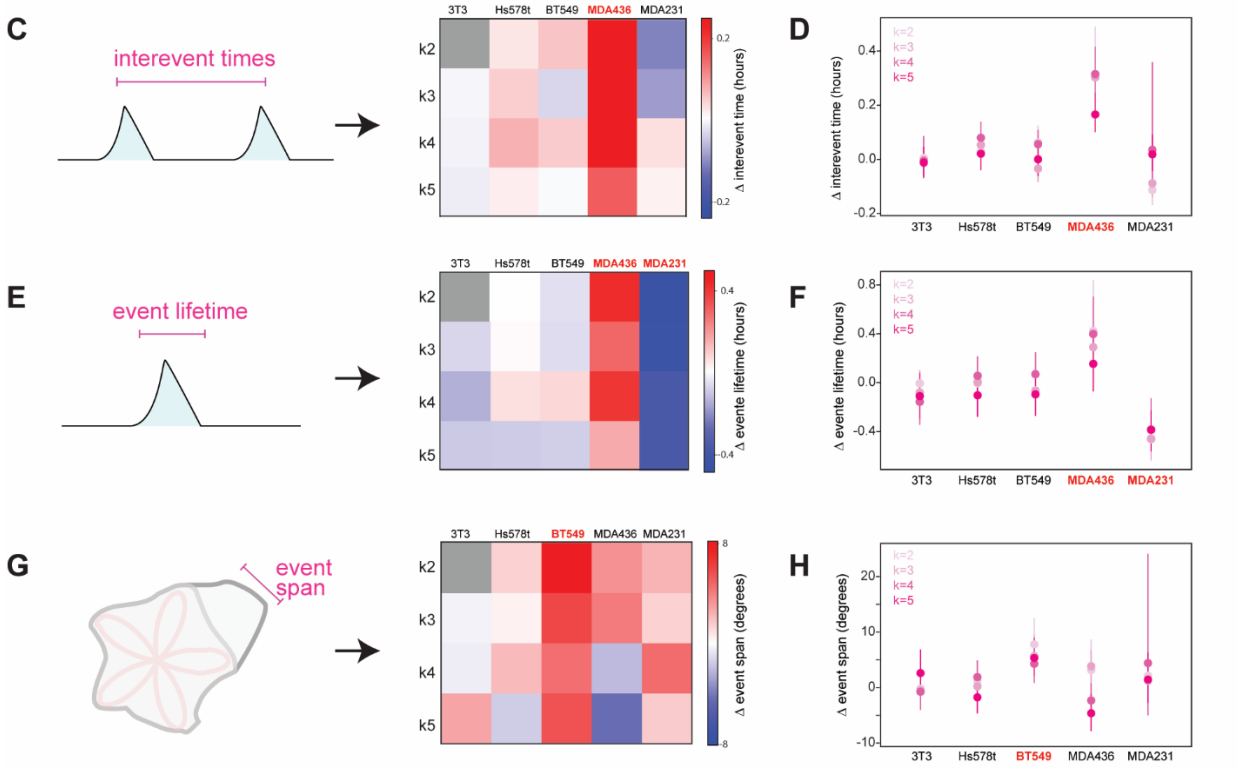

Slow timescale: how is global shape fluctuation modulated by the underlying internal configuration of a cancer cell line?

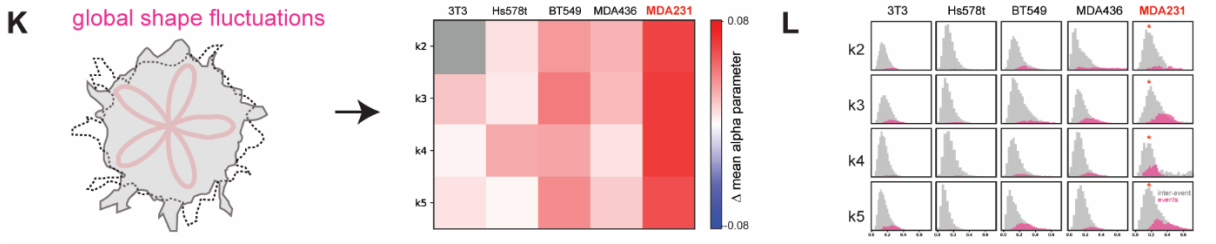

Figure 4. Profiling cancer-cell lines on micropatterned islands identifies different statistical axes associated with divergent morphological signals and cell dynamics.

(a) Schema depicting experimental design for building statistical profiles for different cancer cell lines based on the morphology signals they generate when adhered to different micropattern geometries. Cell lines were imaged on 50 um micropatterns across 4 levels of spatial complexity (k2, k3, k4, k5). The resulting single-cell tracks were digitized for analysis using the workflow from Fig. 2 and aggregated by cell-type and INPUT pattern for statistical comparison between different conditions.

(b) Examples of divergent morphological signals (presented both as kymographs and α time courses) observed when different cancer cells are grown on different micropattern substrates. Top: an example morphological signal observed from a MDA438 cell Bottom: an example morphological signal from an MDA231 cell.

(c) Relative “interevent time” statistics across the panel of cell lines and input patterns, using the k2 3T3 data as an outgroup reference for comparison by the “shared control bootstrapping” method.

(d) Plot of the data in (c) showing the trends observed when micropattern spatial complexity is varied for each cell line tested. Values and error bars derived using the “shared control bootstrapping” method (see also Fig. S4).

(e) Relative “event lifetime” statistics across the panel of cell lines, using the k2 3T3 data as an outgroup reference for comparison by the “shared control bootstrapping” method.

(f) Plot of the data in (e) showing the trends observed when micropattern spatial complexity is varied for each cell line. Values and error bars derived using the “shared control bootstrapping” method (see also Fig. S3).

(g) Relative “pattern alignment” statistics across the panel of cell lines, using the 3t3 k2 pattern as the reference for comparison by the “shared control bootstrapping” method.

(h) Plot of the data in (g) showing the trends observed when micropattern spatial complexity is varied for each cell line. Values and error bars derived using the “shared control bootstrapping” method (see also Fig. S3).

(i) Relative “pattern alignment” statistics for an event across the panel of cell lines, using the 3t3 k2 pattern data as the reference for comparison by the “shared control bootstrapping” method.

(j) Plot of the data used to generate (i) projected onto the underlying shape of the micropattern for direct visualization of event-to-pattern alignment across the different cell lines tested.

(k) “Global shape fluctuation” statistics (from α distributions) across the panel of INPUT patterns, using the 3t3 k2 pattern data as the reference for comparison by the “shared control bootstrapping” method.

(l) Partitioning of the overall distribution of α values from (k) into “event” and “inter-event” timepoints across the panel of different cell lines.

Supplemental Information

Comparative profiling of cellular gait on adhesive micropatterns defines statistical patterns of activity that underlie native and cancerous cell dynamics.

John C. Ahn[1,2], Scott M. Coyle[1,*]

Affiliations:

[1]Department of Biochemistry

[2]Integrated Program in Biochemistry Graduate Program

University of Wisconsin-Madison, Madison, Wisconsin 53706, USA.

*Correspondence to: smcoyle@wisc.edu

Contains:

Supplemental Figures S1-S4 and Legends.

A

Single-cell gait analysis:
abscence of landmarks poses challenges

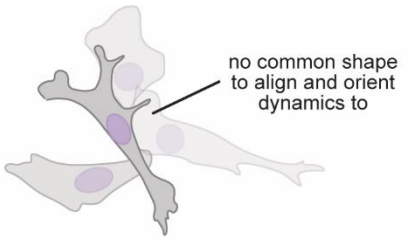

example images from timecourse of 3T3 dynamics on standard tissue culture plates

B

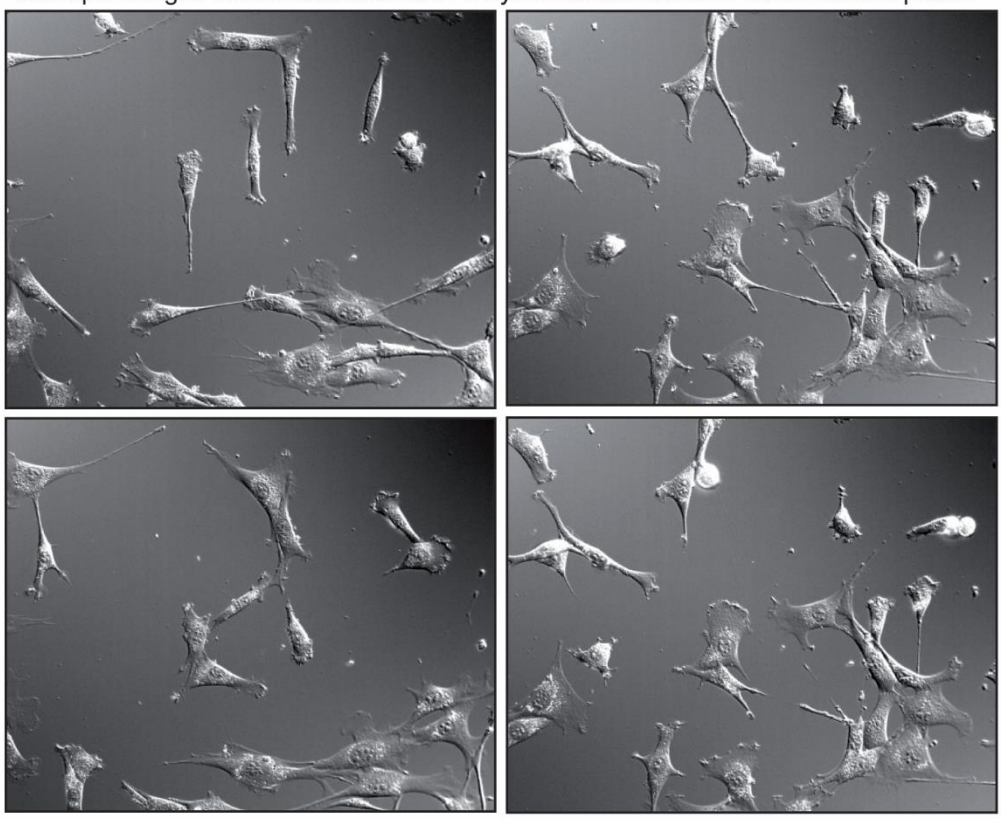

examples of cells on adhesive micropatterns fluctuating about a steady-state geometry

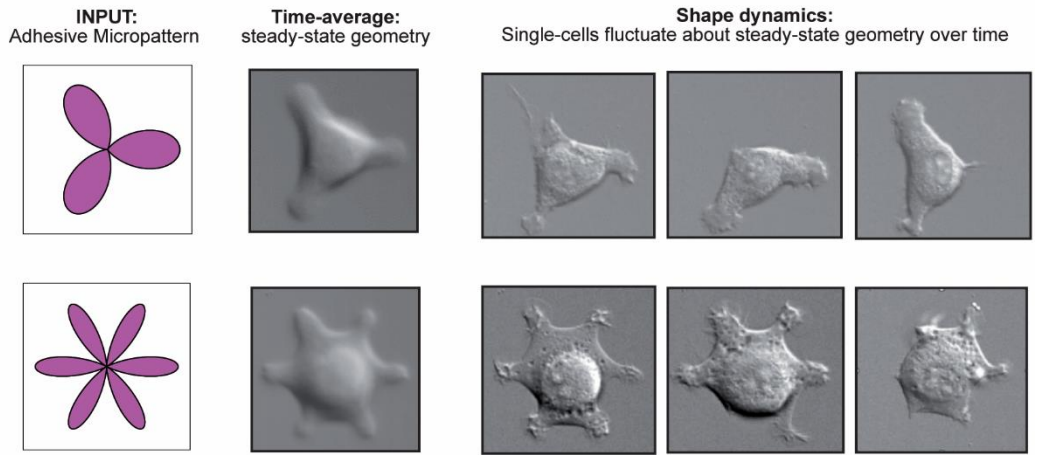

Figure S1. Additional data: cells grown on adhesive micropattern islands undergo dynamic shape fluctuations about an average cell shape.

(a) Schematic for how statistical gait analysis is difficult to apply to metazoan cells owing to a lack of landmarks and stereotyped geometry.

(b) Snapshots of 3T3 cells from an overnight imaging experiment. A wide array of shapes and morphologies are observed, making it difficult to quantify and align the dynamics between cells.

(c) Time-average image produced from an image stack of a 3T3 cell grown on a k3 fibronectin micropattern over a 12 hours period, and representative images from the time-series. The cell geometry is observed to fluctuate substantially from the time-average shape throughout the timecourse.

(d) Time-average image produced from an image stack of a 3T3 cell grown on a k6 fibronectin micropattern over a 12 hours period, and representative images from the time-series. The cell geometry is observed to fluctuate substantially from the time-average shape throughout the timecourse.

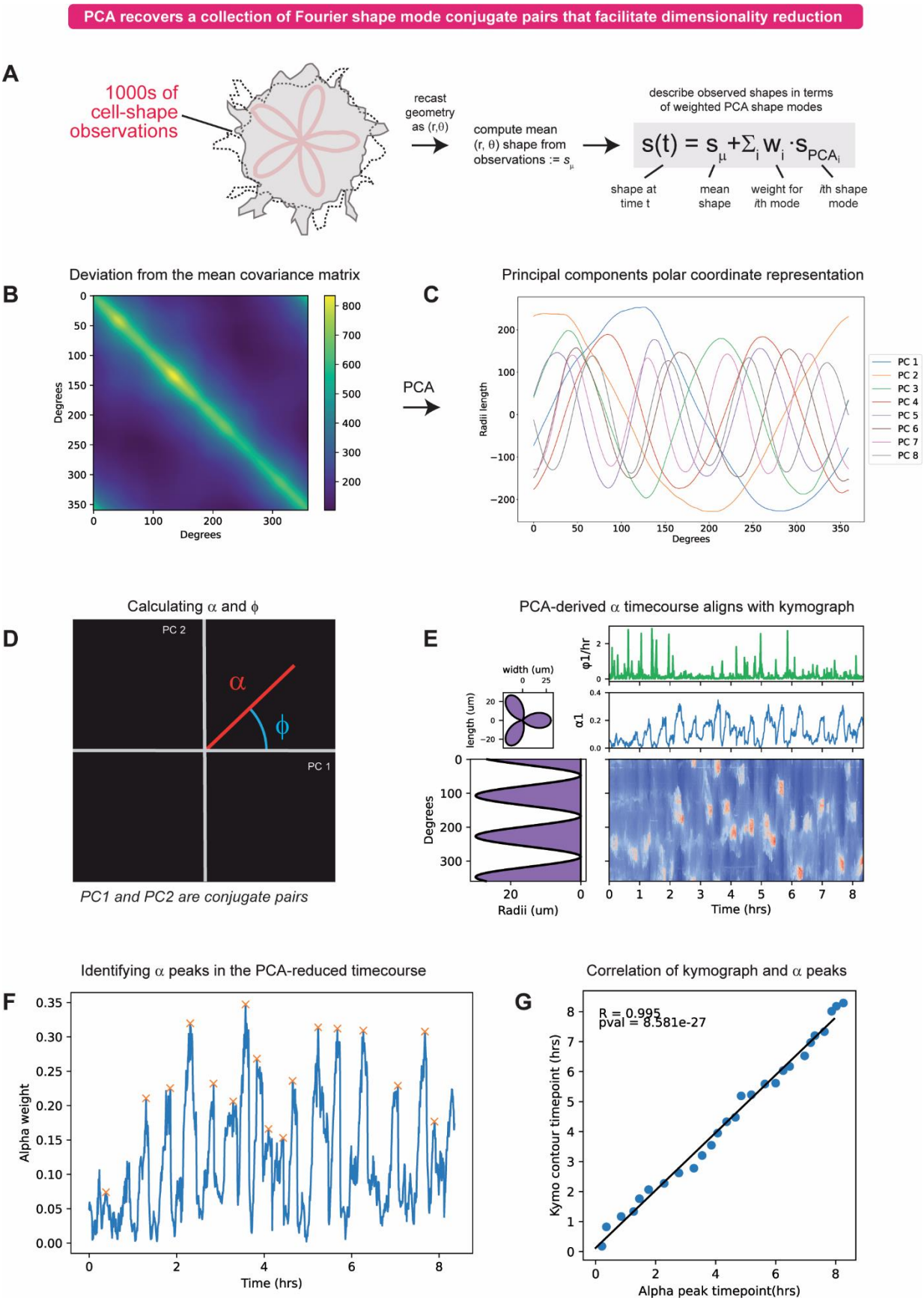
PCA recovers a collection of Fourier shape mode conjugate pairs that facilitate dimensionality reduction
A
1000s of cell-shape observations
recast geometry as (r,θ)
compute mean (r, θ) shape from observations := s_μ
describe observed shapes in terms of weighted PCA shape modes
$s(t) = s_\mu + \Sigma_i w_i \cdot s_{PCA_i}$
shape at time t
mean shape
weight for ith mode
ith shape mode
B
Deviation from the mean covariance matrix
Degrees
Degrees
PCA
C
Principal components polar coordinate representation
Radii length
Degrees
PC 1
PC 2
PC 3
PC 4
PC 5
PC 6
PC 7
PC 8
D
Calculating α and ϕ
PC 2
PC 1
α
ϕ
PC1 and PC2 are conjugate pairs
E
PCA-derived α timecourse aligns with kymograph
width (um)
length (um)
φ1/hr
α1
Degrees
Radii (um)
Time (hrs)
F
Identifying α peaks in the PCA-reduced timecourse
Alpha weight
Time (hrs)
G
Correlation of kymograph and α peaks
R = 0.995
pval = 8.581e-27
Kymo contour timepoint (hrs)
Alpha peak timepoint(hrs)

Figure S2. Additional data: PCA decomposition and shape-mode fitting.

(a) Schematic for how a cell's morphological shape dynamics will be described as a deviation from a mean shape in terms of the weights of a collection of shape modes.

(b) Covariance matrix derived from all morphological observations collected.

(c) r,θ representation of the top 8 PCA-derived shape modes. Note that pairs of conjugate shape modes occur suggesting one can treat these pairs as a fundamental shape mode with an associated magnitude α and phase ϕ.

(d) Schematic for how the magnitude α and phase ϕ are computed from a pair of conjugate shape modes. By treating their combination PCA1+PCA2 as a vector, its magnitude and phase are computed geometrically.

(e) Comparison of PCA-reduced transform of a representative cell's morphological signal to its higher-dimensional kymograph. Time courses for the α parameter, and phase ϕ are shown superimposed on the same timescale as the morphological signal kymograph. Note that when high shape mode usage occurs (high α parameter) this leads to a stabilization of the phase ϕ. Note also that the portions of the timecourse with high α parameter appear to correlate with events in the kymograph.

(f) Results of applying automated peak identification to the PCA-reduced a parameter timecourse. Peaks are denoted with an orange x.

(g) Correlation between appearance of PCA-derived peaks in the α parameter timecourse with events in the kymograph.

Raw statistics of morphology dynamics within a cell line for different geometries of adhesive micropatterned island

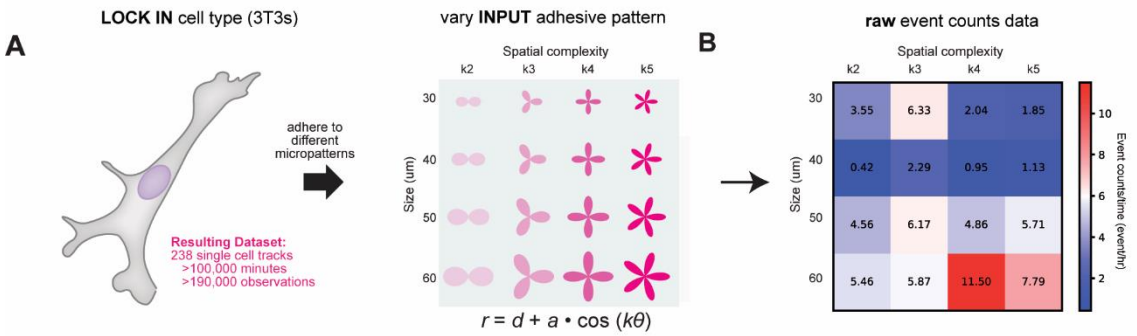

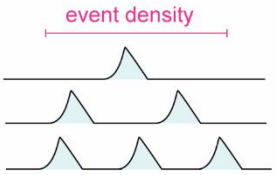

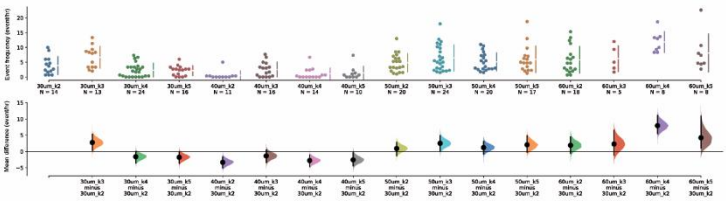

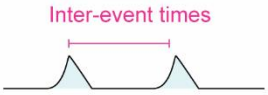

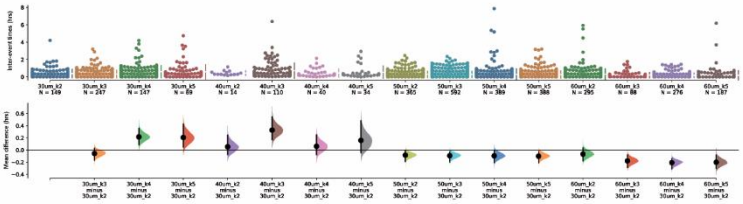

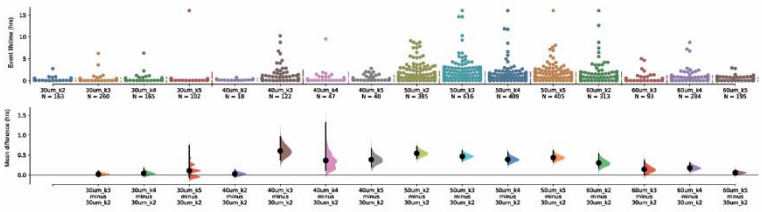

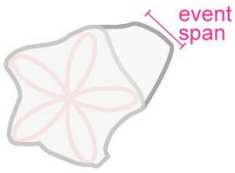

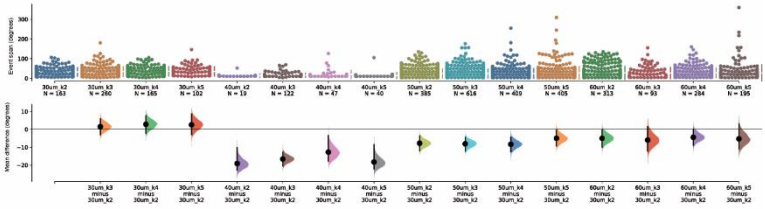

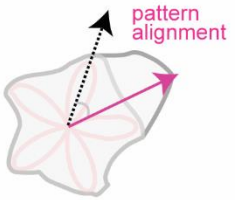

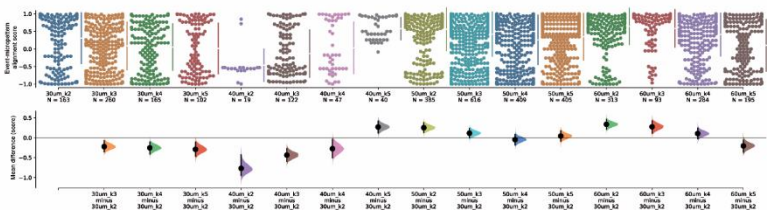

Figure S3. Additional data: the spatial structure of a micropattern island modulates the statistical features of a cell's dynamic morphology signal.

(a) Schema depicting experimental design for interrogating effects of micropattern geometry on 3T3 morphology signals. 3T3 cells were imaged on different micropatterns defined by the harmonics of a circle, such that the spatial complexity and radius of the pattern were independently controlled. The resulting single-cell tracks were digitized for analysis using the workflow from Main Text Fig. 2 and Fig. 2S and aggregated by INPUT pattern for statistical comparison between different conditions.

(b) Raw event count density (events per hour) derived from aggregating the data for each of the micropattern geometries tested.

(c) Additional raw data and visualizations of the "event density" distributions from Main Text Fig. 3. Top: raw "event density" distributions across the panel of INPUT patterns tested. Bottom: transformed distributions using the 30 um k2 pattern as the reference for comparison by the "shared control bootstrapping" method.

(d) Additional raw data and visualizations of the "inter-event time" distributions from Main Text Fig. 3. Top: raw "inter-event time" distributions across the panel of INPUT patterns tested. Bottom: transformed distributions using the 30 um k2 pattern as the reference for comparison by the "shared control bootstrapping" method.

(e) Additional raw data and visualizations of the “event lifetime” distributions from Main Text Fig. 3. Top: raw “event lifetime” distributions across the panel of INPUT patterns tested. Bottom: transformed distributions using the 30 um k2 pattern as the reference for comparison by the “shared control bootstrapping” method.

(f) Additional raw data and visualizations of the “event span” distributions from Main Text Fig. 3. Top: raw “event span” distributions across the panel of INPUT patterns tested. Bottom: transformed distributions using the 30 um k2 pattern as the reference for comparison by the “shared control bootstrapping” method.

(g) Additional raw data and visualizations of the “pattern alignment” distributions from Main Text Fig. 3. Top: raw “pattern alignment” score distributions across the panel of INPUT patterns tested. Bottom: transformed distributions using the 30 um k2 pattern as the reference for comparison by the “shared control bootstrapping” method.

Raw statistics of morphology dynamics for cancer cell lines grown on a panel of adhesive micropatterned islands

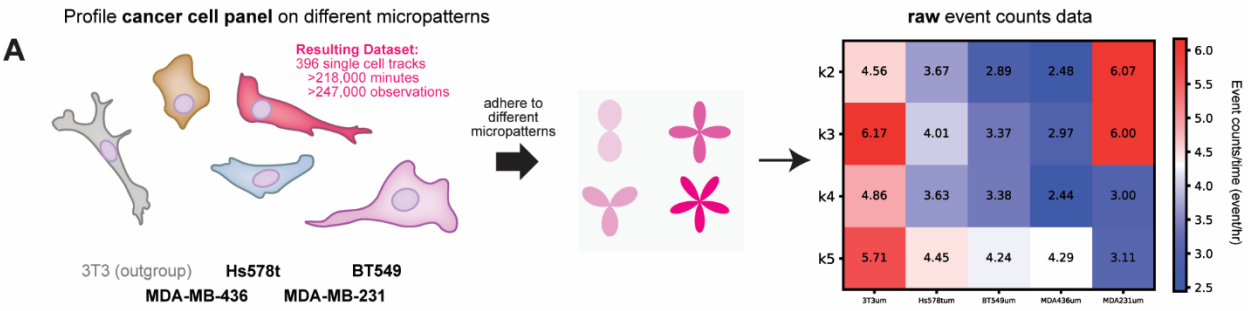

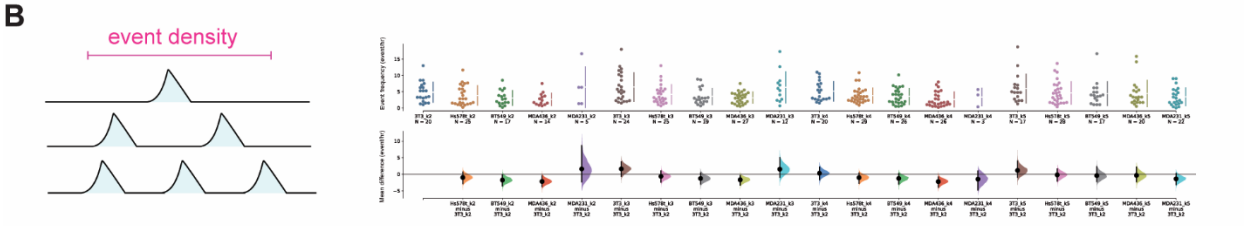

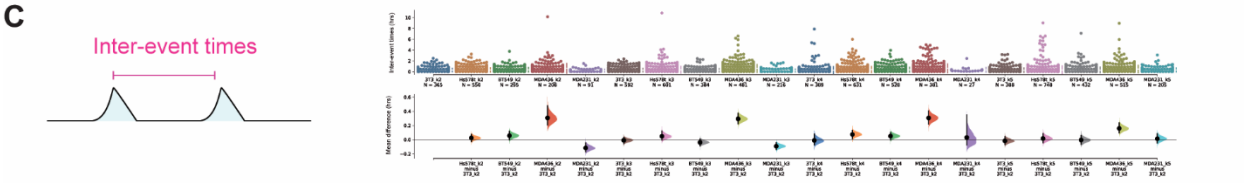

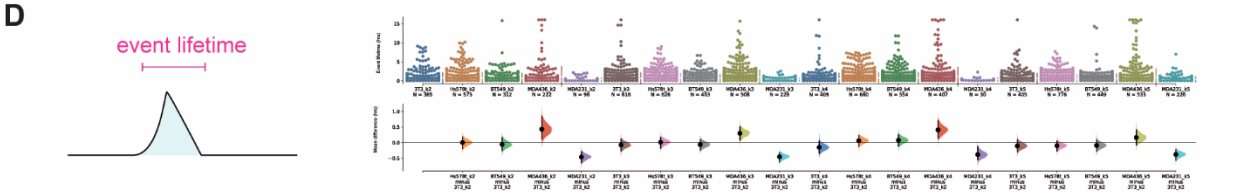

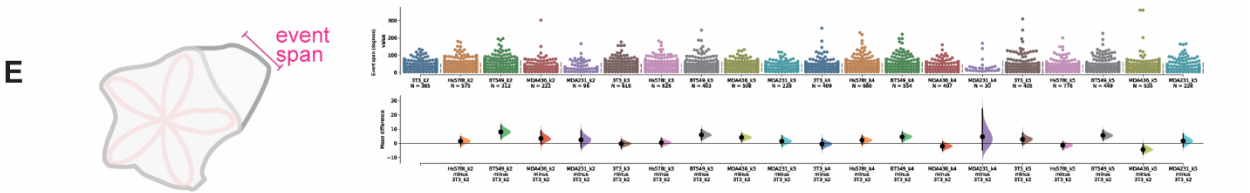

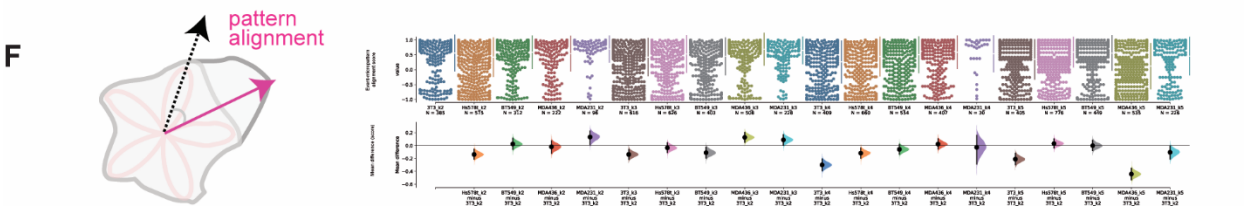

Figure S3. Additional data: profiling cancer-cell lines on micropatterned islands identifies different statistical axes associated with divergent morphological signals and cell dynamics.

(a) Left: schema depicting experimental design for building statistical profiles for different cancer cell lines based on the morphology signals they generate when adhered to different micropattern geometries. Cell lines were imaged on 50 um micropatterns across 4 levels of spatial complexity (k2, k3, k4, k5). The resulting single-cell tracks were digitized for analysis using the workflow from Fig. 2 and aggregated by cell-type and INPUT pattern for statistical comparison between different conditions. Right: raw event count density (events per hour) derived from aggregating the data for each of the micropattern geometries and cell lines tested.

(b) Additional raw data and visualizations of the “event density” distributions from Main Text Fig. 4. Top: raw “event density” distributions across the panel of INPUT patterns tested. Bottom: transformed distributions using the 30 um k2 pattern as the reference for comparison by the “shared control bootstrapping” method.

(c) Additional raw data and visualizations of the “inter-event time” distributions from Main Text Fig. 4. Top: raw “inter-event time” distributions across the panel of INPUT patterns tested. Bottom: transformed distributions using the 30 um k2 pattern as the reference for comparison by the “shared control bootstrapping” method.

(d) Additional raw data and visualizations of the “event lifetime” distributions from Main Text Fig. 4. Top: raw “event lifetime” distributions across the panel of INPUT patterns tested. Bottom: transformed distributions using the 30 um k2 pattern as the reference for comparison by the “shared control bootstrapping” method.

(e) Additional raw data and visualizations of the “event span” distributions from Main Text Fig. 4. Top: raw “event span” distributions across the panel of INPUT patterns tested. Bottom: transformed distributions using the 30 um k2 pattern as the reference for comparison by the “shared control bootstrapping” method.

(f) Additional raw data and visualizations of the “pattern alignment” distributions from Main Text Fig. 4. Top: raw “pattern alignment” score distributions across the panel of INPUT patterns tested. Bottom: transformed distributions using the 30 um k2 pattern as the reference for comparison by the “shared control bootstrapping” method.

References

Bachmann, M., Kukkurainen, S., Hytönen, V. P., & Wehrle-Haller, B. (2019). Cell adhesion by integrins. *Physiological Reviews*, *99*(4), 1655–1699. https://doi.org/10.1152/physrev.00036.2018

Barczyk, M., Carracedo, S., & Gullberg, D. (2010). Integrins. *Cell and Tissue Research*, *339*(1), 269–280. https://doi.org/10.1007/s00441-009-0834-6

Bock, C., Datlinger, P., Chardon, F., Coelho, M. A., Dong, M. B., Lawson, K. A., Lu, T., Maroc, L., Norman, T. M., Song, B., Stanley, G., Chen, S., Garnett, M., Li, W., Moffat, J., Qi, L. S., Shapiro, R. S., Shendure, J., Weissman, J. S., & Zhuang, X. (2022). High-content CRISPR screening. *Nature Reviews Methods Primers*, *2*(1). https://doi.org/10.1038/s43586-021-00093-4

Bravo-Cordero, J. J., Hodgson, L., & Condeelis, J. (2012). Directed Cell Invasion and Migration During Metastasis Jose. *Curr Opin Cell Biol.*, *24*(23), 277–283. https://doi.org/10.1016/j.ceb.2011.12.004.Directed

Brückner, D. B., Fink, A., Schreiber, C., Röttgermann, P. J. F., Rädler, J. O., & Broedersz, C. P. (2019). Stochastic nonlinear dynamics of confined cell migration in two-state systems. *Nature Physics*, *15*(6), 595–601. https://doi.org/10.1038/s41567-019-0445-4

Castellano, F., Chavrier, P., & Caron, E. (2001). Actin dynamics during phagocytosis. *Seminars in Immunology*, *13*(6), 347–355. https://doi.org/10.1006/smim.2001.0331

Choo, M., Mai, V. H., Kim, H. S., Kim, D. H., Ku, J. L., Lee, S. K., Park, C. K., An, Y. J., & Park, S. (2023). Involvement of cell shape and lipid metabolism in glioblastoma

resistance to temozolomide. *Acta Pharmacologica Sinica*, *44*(3), 670–679. https://doi.org/10.1038/s41401-022-00984-6

Cicirelli, G., Impedovo, D., Dentamaro, V., Marani, R., Pirlo, G., & D'Orazio, T. R. (2022). Human Gait Analysis in Neurodegenerative Diseases: A Review. *IEEE Journal of Biomedical and Health Informatics*, *26*(1), 229–242. https://doi.org/10.1109/JBHI.2021.3092875

Cooper, J. A. (1991). The role of actin polymerization in cell motility. *Annual Review of Physiology*, *53*(1), 585–605. https://doi.org/10.1146/annurev.ph.53.030191.003101

Coyle, S. M., Flaum, E. M., Li, H., Krishnamurthy, D., & Prakash, M. (2019). Coupled Active Systems Encode an Emergent Hunting Behavior in the Unicellular Predator Lacrymaria olor. *Current Biology*, *29*(22), 3838-3850.e3. https://doi.org/10.1016/j.cub.2019.09.034

D'Anselmi, F., Valerio, M., Cucina, A., Galli, L., Proietti, S., Dinicola, S., Pasqualato, A., Manetti, C., Ricci, G., Giuliani, A., & Bizzarri, M. (2011). Metabolism and cell shape in cancer: A fractal analysis. *International Journal of Biochemistry and Cell Biology*, *43*(7), 1052–1058. https://doi.org/10.1016/j.biocel.2010.05.002

Doench, J. G. (2018). Am i ready for CRISPR? A user's guide to genetic screens. *Nature Reviews Genetics*, *19*(2), 67–80. https://doi.org/10.1038/nrg.2017.97

Grada, A., Otero-Vinas, M., Prieto-Castrillo, F., Obagi, Z., & Falanga, V. (2017). Research Techniques Made Simple: Analysis of Collective Cell Migration Using the Wound Healing Assay. *Journal of Investigative Dermatology*, *137*(2), e11–e16. https://doi.org/10.1016/j.jid.2016.11.020

Hofman, M., Kolejewska, A., Greven, J., Andruszkow, H., Kobbe, P., Tolba, R., Hildebrand, F., & Poeze, M. (2020). Gait analysis and muscle weight analysis after lower extremity fractures in a small animal model. *Gait and Posture*, *77*(January), 207–213. https://doi.org/10.1016/j.gaitpost.2020.01.022

Holly, S. P., Larson, M. K., & Parise, L. V. (2000). Multiple roles of integrins in cell motility. *Experimental Cell Research*, *261*(1), 69–74. https://doi.org/10.1006/excr.2000.5040

Hums, I., Riedl, J., Mende, F., Kato, S., Kaplan, H. S., Latham, R., Sonntag, M., Traunmüller, L., & Zimmer, M. (2016). Regulation of two motor patterns enables the gradual adjustment of locomotion strategy in caenorhabditis elegans. *ELife*, *5*(MAY2016), 1–36. https://doi.org/10.7554/eLife.14116

Juliano, R. L., Reddig, P., Alahari, S., Edin, M., Howe, A., & Aplin, A. (2004). Integrin regulation of cell signalling and motility. *Biochemical Society Transactions*, *32*(3), 443–446. https://doi.org/10.1042/BST0320443

Keren, K., Pincus, Z., Allen, G. M., Barnhart, E. L., Marriott, G., Mogilner, A., & Theriot, J. A. (2008). Mechanism of shape determination in motile cells. *Nature*, *453*(7194), 475–480. https://doi.org/10.1038/nature06952

Kim, Y. A., Cho, D. Y., & Przytycka, T. M. (2016). Understanding Genotype-Phenotype Effects in Cancer via Network Approaches. *PLoS Computational Biology*, *12*(3), 1–15. https://doi.org/10.1371/journal.pcbi.1004747

Larson, B. T., Garbus, J., Pollack, J. B., & Marshall, W. F. (2022). A unicellular walker controlled by a microtubule-based finite-state machine. *Current Biology*, *32*(17),

3745-3757.e7. https://doi.org/10.1016/j.cub.2022.07.034

Lehmann, B. D., Bauer, J. A., Chen, X., Sanders, M. E., Chakravarthy, A. B., Shyr, Y., & Pietenpol, J. A. (2011). Identification of human triple-negative breast cancer subtypes and preclinical models for selection of targeted therapies. *Journal of Clinical Investigation*, *121*(7), 2750–2767. https://doi.org/10.1172/JCI45014

Luster, A. D., Alon, R., & von Andrian, U. H. (2005). Immune cell migration in inflammation: Present and future therapeutic targets. *Nature Immunology*, *6*(12), 1182–1190. https://doi.org/10.1038/ni1275

Marcon, L., Arqués, C. G., Torres, M. S., & Sharpe, J. (2011). A computational clonal analysis of the developing mouse limb bud. *PLoS Computational Biology*, *7*(2). https://doi.org/10.1371/journal.pcbi.1001071

Marques, J. C., Lackner, S., Félix, R., & Orger, M. B. (2018). Structure of the Zebrafish Locomotor Repertoire Revealed with Unsupervised Behavioral Clustering. *Current Biology*, *28*(2), 181-195.e5. https://doi.org/10.1016/j.cub.2017.12.002

McManus, M. F., & Golden, J. A. (2005). Neuronal migration in developmental disorders. *Journal of Child Neurology*, *20*(4), 280–286. https://doi.org/10.1177/08830738050200040301

Pascual-Vargas, P., Cooper, S., Sero, J., Bousgouni, V., Arias-Garcia, M., & Bakal, C. (2017). RNAi screens for Rho GTPase regulators of cell shape and YAP/TAZ localisation in triple negative breast cancer. *Scientific Data*, *4*, 1–13. https://doi.org/10.1038/sdata.2017.18

Riquet, F., Simon, A., & Bierne, N. (2017). Weird genotypes? Don’t discard them,

transmissible cancer could be an explanation. *Evolutionary Applications*, *10*(2), 140–145. https://doi.org/10.1111/eva.12439

Roberts, M., Mongeon, D., & Prince, F. (2017). Biomechanical parameters for gait analysis: a systematic review of healthy human gait. *Physical Therapy and Rehabilitation*, *4*(1), 6. https://doi.org/10.7243/2055-2386-4-6

Rossman, K. L., Der, C. J., & Sondek, J. (2005). GEF means go: Turning on Rho GTPases with guanine nucleotide-exchange factors. *Nature Reviews Molecular Cell Biology*, *6*(2), 167–180. https://doi.org/10.1038/nrm1587

Scarpa, E., & Mayor, R. (2016). Collective cell migration in development. *Journal of Cell Biology*, *212*(2), 143–155. https://doi.org/10.1083/jcb.201508047

Seetharaman, S., & Etienne-Manneville, S. (2018). Integrin diversity brings specificity in mechanotransduction. *Biology of the Cell*, *110*(3), 49–64. https://doi.org/10.1111/boc.201700060

Strale, P. O., Azioune, A., Bugnicourt, G., Lecomte, Y., Chahid, M., & Studer, V. (2016). Multiprotein Printing by Light-Induced Molecular Adsorption. *Advanced Materials*, *28*(10), 2024–2029. https://doi.org/10.1002/adma.201504154

Sun, N., Xu, H. N., Luo, Q., & Li, L. Z. (2016). Potential indexing of the invasiveness of breast cancer cells by mitochondrial redox ratios. *Advances in Experimental Medicine and Biology*, *923*, 121–127. https://doi.org/10.1007/978-3-319-38810-6_16

Théry, M. (2010). Micropatterning as a tool to decipher cell morphogenesis and functions. *Journal of Cell Science*, *123*(24), 4201–4213.

https://doi.org/10.1242/jcs.075150

Théry, M., Pépin, A., Dressaire, E., Chen, Y., & Bornens, M. (2006). Cell distribution of stress fibres in response to the geometry of the adhesive environment. *Cell Motility and the Cytoskeleton*, *63*(6), 341–355. https://doi.org/10.1002/cm.20126

Théry, M., Racine, V., Piel, M., Pépin, A., Dimitrov, A., Chen, Y., Sibarita, J. B., & Bornens, M. (2006). Anisotropy of cell adhesive microenvironment governs cell internal organization and orientation of polarity. *Proceedings of the National Academy of Sciences of the United States of America*, *103*(52), 19771–19776. https://doi.org/10.1073/pnas.0609267103

Trepat, X., Chen, Z., & Jacobson, K. (2012). Cell migration. *Comprehensive Physiology*, *2*(4), 2369–2392. https://doi.org/10.1002/cphy.c110012

Urbach, D., Lupien, M., Karagas, M. R., & Moore, J. H. (2012). Cancer heterogeneity: origins and implications for genetic association studies. *Trends Genet.*, *28*(11), 538–543. https://doi.org/10.1016/j.tig.2012.07.001.Cancer

Vandin, F., Upfal, E., & Raphael, B. J. (2011). Algorithms for detecting significantly mutated pathways in cancer. *Journal of Computational Biology*, *18*(3), 507–522. https://doi.org/10.1089/cmb.2010.0265

Vesperini, D., Montalvo, G., Qu, B., & Lautenschläger, F. (2021). Characterization of immune cell migration using microfabrication. *Biophysical Reviews*, *13*(2), 185–202. https://doi.org/10.1007/s12551-021-00787-9

Yu, J. S., & Bagheri, N. (2020). Agent-Based Models Predict Emergent Behavior of Heterogeneous Cell Populations in Dynamic Microenvironments. *Frontiers in*

Bioengineering and Biotechnology, *8*(June), 1–22. https://doi.org/10.3389/fbioe.2020.00249

Zemel, A., & Mogilner, A. (2009). Motor-induced sliding of microtubule and actin bundles. *Physical Chemistry Chemical Physics*, *11*(24), 4821–4833. https://doi.org/10.1039/b901646e

Zhang, J., Späth, S. S., Marjani, S. L., Zhang, W., & Pan, X. (2018). Characterization of cancer genomic heterogeneity by next-generation sequencing advances precision medicine in cancer treatment. *Precision Clinical Medicine*, *1*(1), 29–48. https://doi.org/10.1093/pcmedi/pby007

Chapter 3: Extending micropatterning and principal component analysis to the MinDE system in mammalian cells

John Ahn[1], Rohith Rajasekaran[1], Dennis Bolshakov[1], and Scott Coyle[1].

[1]Department of Biochemistry, University of Wisconsin-Madison, Wisconsin, USA

Author contributions

J.A., R.R., and S.C. conceptualization; J.A., R.R., D.B. methodology; J.A., R.R., D.B. formal analysis; J.A. and R.R. investigation; J.A. writing.

Abstract

The MinDE reaction diffusion system generates oscillations of spatiotemporal patterns, which in bacterial systems defines poles and the center of the cell for division. Previous work in the Coyle lab implanted the bacterial MinDE system in mammalian cells as a biosynthetic circuit, enabling for orthogonal control of generating spatiotemporal patterns that can be linked to native processes for engineering desired outputs. It was established how the ratio of MinDE and the biochemical structure of the active sites between the two proteins played a large role in modulating the frequency of the MinDE oscillations. However, it was never established how the shape of the cell could influence the patterns that arise. To fill that gap, we plated mammalian cells with transduced MinDE systems onto micropatterns to assess how defined cellular morphologies could influence the resulting oscillatory patterns. Cells on unbound glass substrates were also analyzed using principal component analysis to assess how certain geometries could bias the resulting MinDE patterns. Size and aspect ratio were found to influence the directionality of the vector flow fields, suggesting that the shape of the cell can direct the types of MinDE patterns that arise.

Introduction

Oscillatory spatiotemporal patterns are observed in biological organisms for a variety of processes, including signal transduction pathways, organ development, and skin pattern placement, with many of these phenomena captured by reaction-diffusion models, a commonly used theoretical model used to describe self-regulated pattern formation (Kondo & Miura, 2010). A canonical example of these types of reaction-diffusion models is that of the *E. coli* MinDE system (**Fig. 1A-C**), responsible for the location of the cytokinetic Z ring for division (Park et al., 2011). By oscillating waves of MinD and MinE proteins along the cell membrane from pole to pole, the system creates a time-averaged gradient of a third protein in the system, MinC, which inhibits FtsZ assembly (Raskin & de Boer, 1999; Wettmann & Kruse, 2018). Through these oscillations, the MinDE system concentrates MinC to the poles, preventing ring assembly for cytokinesis at the distal ends of the bacterial cell, but allowing for uninhibited assembly via FtsZ at the center of the cell, which is where MinC spends the least amount of time (Rowlett & Margolin, 2013).

Recent efforts in the Coyle lab have taken advantage of the MinDE system as a potential biosynthetic control knob for engineering specified, orthogonal spatiotemporal patterns in mammalian cell systems (**Fig. 1D**) that could be used to either readout or influence native processes (Rajasekaran et al., 2022). The frequency and power of these oscillations was found to be highly influenced by the ratio of MinE to MinD, along with mutations in MinE (**Fig. 1E-F**).

However, the parameter space required for generating even more frequencies or types of patterns remained largely unexplored. For example, individual cases of

standing protein oscillations or stationary protein patterns distinct from the dominating traveling protein waves were observed (Rajasekaran et al., 2022). To probe how to reproducibly and intentionally generate these patterns and even open up other pattern types, it was necessary to explore the impact of other parameters within this mammalian cell MinDE system.

A potential parameter for control was the size and shape of the cell, the container geometry for the MinDE reaction-diffusion system. In other organisms, it was observed that the shape and geometrical properties of the container of the system influenced the resulting types of spatiotemporal patterns that would arise, such as the skin color pattern of ocellated lizards (Fofonjka & Milinkovitch, 2021). Based on the ability of micropatterning to guide cellular shape and size for adhesive cells, we used that technique to ask how different MinDE patterns could arise based on changing cellular shapes. By changing the aspect ratio of the micropatterns, and thus also biasing the aspect ratio of the adhered cells, we found that the direction of the oscillatory vector field preferentially traveled along the long side of the cell. Increasing the size of the micropattern and resulting cell size resulted in a narrowing of MinDE ratio and frequency. When applying PCA to cell shapes on unbound glass, we found that different shape mode subpopulations exhibited different preferential phase angle distributions, suggesting that the shape of the cell plays a role in the directional flow of reaction-diffusion systems.

Results

Cell aspect ratio biases phase angle of MinDE traveling waves

On a pixel-by-pixel level, the frequency of the oscillating MinDE waves can be calculated using Fast Fourier Transform (FFT). As with any wave, the phase, at what point of the waveform cycle at a point in time is the agent at question located, can also be calculated. Thus, the phase angle of each pixel within a cell of interest can be calculated, as well as the vector field, thus showing the directional flow of the travel wave (**Fig. 2B**).

In order to assess how the shape of the cell could influence the direction of the MinDE traveling waves, we decided on using the dot product between vectors of the cell perimeter and the vectors of each pixel within the cell. While two vectors pointing in the same direction would yield higher positive values, two vectors pointing in opposite directions would yield more negative values, and perpendicular vectors would yield a product of zero, giving a simple numerical output for assessing the relative positions of two vectors (**Fig. 2A**). In order to determine the perimeter vectors for the dot product analysis, fluorescence microscopy timelapse videos of mCherry-MinD 3T3 cells were collected, the frequency of the oscillations were calculated using FFT, a binary threshold was set and subjected to denoising functions (**Fig 2C**). A polygon approximation of the resulting contour was used, adjusting epsilon values such that the enough sides of the perimeter would be collected for analysis. Once the perimeter sides of the cell contour were determined, they were multiplied by each of the vectors within the boundaries of the cell to calculate the dot product.

An example 3T3 MinDE cell was analyzed using this pipeline (**Fig. 2D**). Each of the four perimeter edges were multiplied against all of the flow vectors within the cell. Both of the edges along the long axis of the cell showed wider ranges within the dot product distributions in comparison to the dot products of the short axis edges. The shapes of the distributions were largely similar regardless of the axis, showing bimodal distributions with a dip centered around the zero point. The distributions were all fairly symmetrical between negative and positive values, suggesting that this particular cell had an even spread of directions flowing throughout the cell.

Several other cells with different kinds of MinDE pattern archetypes were explored using this analysis. Two cells (**Fig. 3A-B**) exhibited standing wave MinD patterns, meaning that instead of a traveling wave, only two patterns would flicker back and forth from each other in a binary state. Because there was no clear flow or directionality, the resulting vector fields showed phases pointing pretty uniformly across 360º, both seen on the vector map and reflected on the border-vector dot product distributions that were all centered around zero.

By contrast, some other cells demonstrated a clear direction of flow with traveling MinDE waves both visually and when represented on the vector fields (**Fig. 3C-D**). The dot product distributions also showed noticeably shifted distributions when compared to the standing wave cells (**Fig. 3A-B**). While the standing wave cell distributions suggested a more even distribution of phase angles across all 360º, the distributions of the traveling wave cells suggest that the population of vectors are biased in a certain direction, thus shifting the dot product distribution towards an either positive or negative magnitude.

In order to take these results a step further, we decided to select a systematic group of micropatterns that would change the aspect ratio of the cell, biasing its shape and potentially directing the flow of the MinDE patterns.

Changing the aspect ratio of the cell biases the direction of the MinDE vector field

With the goal of biasing the shape of mammalian cells expressing the MinDE system (**Fig. 4A**), we decided to seed the cells onto micropatterns. These micropatterns were kept at a constant area of 1800 μm^2, but their aspect ratios were: 1:1 as a control, 2:1, 4:1, and 8:1 (**Fig. 4B**). Preliminary results showed that the cells were able to adhere to the micropatterns and more or less adopt the aspect ratio imposed by the micropatterns (**Fig. 4C**).

In order to optimize the incubation time necessary for the cells to spread over as much area of the micropattern as possible and avoiding cell division as much as possible, four different incubation timepoints were chosen, and the percent composition of the types of spreading and number of cells present per micropattern were evaluated (**Fig. 4D**). The goal was to maximize the percent composition of total single cells that spread fully on the different aspect ratios while minimizing the percent composition of cells that either only partially spread or had more than one cell adhered to the micropattern. It was found that the 4- and 6-hour incubation times had the highest spreading of just one cell while avoiding a lot of the multiple cells per micropattern that was observed at 24-hours, which was well past the typical time necessary for a 3T3 cell to divide.

After optimizing the incubation times, 3T3 MinDE cells were played onto the four different aspect ratios, their frequencies, phase angles, and vector fields were all calculated (**Fig. 4E**). Density plots of the phase angle distributions showed that as the aspect ratio of the micropattern increased, the cells exhibited more of a bias in their vector field flow directions. For the most part, the 1:1 ratio micropattern cells had a fairly even distribution across all phase angles, suggesting that this kind of symmetrical shape of the cell results in a random distribution of directions for the traveling wave to flow in. Although the overall shape of the distribution doesn't change by much when increasing the aspect ratio to 2:1, the position of the peak shifts to around zero. Increasing the aspect ratio to 4:1 results in the distribution shifting into a more bimodal distribution, also showing a more oblong shape biased towards 0º and 180º when shown in polar coordinates (**Fig. 4F**). After increasing the aspect ratio to 8:1, this bias becomes even more pronounced both in the density plot and the polar coordinate representation of the phase angle distributions. What this suggests is that the phase angles of the MinDE vector field are biased towards the long axes of the cell, traveling along the length of the long cells rather than the width.

Increasing cell size influences the frequency of MinDE dynamics

After testing how the aspect ratio of the cell could influence the MinDE dynamics, we decided to explore how the size of the cell could also be a factor. As a simple way of assessing cell size, squares of four different areas were chosen to be the templates for the micropatterns: 2500μm^2, 5625 μm^2, 10,000μm^2, and 15,625μm^2 (**Fig. 5A**). The actual areas of the cells were calculated by thresholding via frequency and calculating

the size of the contours. Although the cells did not spread out across the larger micropattern sizes in entirety, the size of the micropattern did shift the distribution of cell sizes to be higher (**Fig. 5B**). Moving forward the MinDE ratio was calculated and compared to the area of the cell. When binning cells by their size, it appeared that the larger the cell, the tighter the range of MinDE (**Fig. 5C**). When binning the cells by the micropatterns they were grown on, the same trend appeared to hold true, with cells grown on the largest micropatterns appeared to have a narrower range of MinDE ratios (**Fig. 5D**). Because frequency was found to be largely reliant on the MinDE ratio, it followed that the frequencies of the cells followed a similar trend. Cells binned by size appeared to have a slightly narrower and higher shifted range of frequencies (**Fig. 5E**). Cells binned by the micropattern they were grown on showed a similar trend (**Fig. 5F**). Taken together, these results suggest that cells that are more spread out have a narrower set of frequencies expressed by their MinDE systems, while cells that are smaller in size have a wider set of frequency expressions.

These results showed cells constrained by micropatterns, restricting either their size or aspect ratio to certain limits. While it was useful in order to parse out the influence of different geometric parameters on the MinDE patterns, it was also limiting in analyzing how specific features of unconstrained cell shapes could play a role in MinDE dynamics. To expand the parameter space for the different kinds of sizes and shapes cells could exhibit, we also conducted experiments on unbound cells on glass substrates.

Relating unbound cell shape to MinDE oscillation parameters

Cells were grown on unbound glass substrates in order to unlock a full spectrum of possible morphologies the cells could exhibit (**Fig. 6A**). After taking fluorescence microscopy timelapse videos, the sizes of the cells were evaluated. There was a wide range of cell size, with most of the population between 0 and 4,000μm^2 (**Fig. 6B**). Binning the cells by their size revealed a narrowing of MinDE oscillation frequency, similar to the findings with the square micropattern experiments (**Fig. 6C**). To correlate the frequency results with the types of shapes that arose from the cells growing on unbound substrate, we conducted principal component analysis on the r,θ descriptions of the cells.

The top eight principal components extracted from the cell shape matrix containing the r,θ description of every cell in the entire experiment explained well over 70% of the variation in the data (**Fig. 6D**). Similar to the principal components that fell out of the analysis conducted in Chapter 3, the principal components for the unbound cell shapes resembled Fourier shape modes (**Fig. 6E-F**).

Each of the cells were fit with the top eight principal components to generate scalar weights of the shape modes that would approximate the shape of each cell. The cells were then binned based off the maximum percent contribution of principal components that could explain the cell shape. The vector field phase angle distributions were then compared to each other, demonstrating different phase angle preferences based on the types of principal component bins (**Fig. 6G**). This suggests that particular shape features that are prominent in a population of cells can change the directionality of the flow of the MinDE traveling waves. The phase angles were compared against the

frequencies of the MinDE oscillations, again comparing the binned principal component subpopulations against each other (**Fig. 6H**). It appears that different principal component subpopulations also exhibit different distributions of frequencies, suggesting that shape features can also modulate the frequencies of the MinDE system.

Discussion

Micropatterning and the image analysis pipeline outlined in Chapter 3 are versatile and can be used for different applications such as the MinDE system in mammalian cells. This reaction-diffusion system that produces spatiotemporal patterns can be potentially engineered to produce desired patterns and frequencies, which could then be used to modulate or monitor native cellular processes. While previous work established how the ratio of MinDE and mutations of the two proteins can change the range of accessible frequencies, we were able to demonstrate how the size and geometrical features of the cell itself can also play a role.

Standing waves or traveling waves can be detected by calculating the dot products of the perimeter edges versus the phase angles of each pixel within the cell. The aspect ratio of the cell can change the directionality of the traveling waves, biasing them towards the long axis. Increasing the area of the cell appears to tighten the range of frequencies expressed, while smaller area cells have a wider range. Finally, specific morphological features detected by principal component analysis appear to influence the range of frequencies and distributions of traveling wave trajectory directions. While this analysis mainly focused on traveling waves, future computational efforts could be devoted towards identifying and characterizing other types of patterns that cannot be detected by their frequency.

Experimental procedures

Cell culturing

3T3 mouse fibroblast cells (ATCC CRL-1658) expressing the MinDE system were obtained from Rohith Rajasekaran from the Coyle lab (Rajasekaran et al., 2022). The cells were cultured in Dulbecco's Modified Eagle's Medium (DMEM) (Sigma-Aldrich D6429) with 10% fortified calf bovine serum (Cytiva Life Sciences SH30396.03) and 1% penicillin-streptomycin (ThermoFisher 15140122). Cells were grown in a 5% CO_2 incubator at 37ºC up to 90% confluence before being washed and passaged. Adherent cells were washed with PBS at each passage and detached from the flask surface by incubating with TrypLE (ThermoFisher Scientific 12604021) for 5-10 minutes at 37ºC. TrypLE was quenched with fresh DMEM media, and cells were resuspended and plated into new flasks with fresh DMEM. The following cancer cell lines were all cultured in DMEM with 10% fetal bovine serum (Fisher Scientific SH30396.03) and 1% penicillin-streptomycin in a 5% CO_2 atmosphere at 37ºC: MDA-MB-453 (ATCC HTB-131) and H1395 (CRL-5868).

Micropatterning

We employed the light-induced molecular adsorption (LIMAP) method for micropatterning (Strale et al., 2016). 35mm Glass bottom petri dishes (MatTek P35G-1.5-20-C) were exposed with oxygen plasma in preparation for passivation. For adsorption of the anti-fouling coating agent, 0.1 mg ml^{-1} PLL(20)-g[3.5]-PEG(2) (SuSoS CHF9,600.00) solution was added for 1 hour. The dish was washed five times with Milli-Q purified water. A 1:5 ratio of PLPP photoinitator gel to 70% ethanol (Alveole) was added to the microwell and dried at room temperature for 1 hour. To create the micropatterns, the well was exposed to UV light at a dosage of 30mJ mm^{-2}, and excess gel was washed away with 5 Milli-Q purified water washes

and 5 Dulbecco's Phosphate Buffered Saline (DPBS) solution (VWR L0119-0500) washes, with the last volume of DPBS left to incubate for 5 minutes to rehydrate the substrate. The wells were then incubated with 10μg ml^{-1} fibronectin (Sigma-Aldrich F1141-5MG) and 10μg ml^{-1} NeutrAvidin (Invitrogen 84607) for five minutes and then washed 5 times with DPBS. PEGs were added at 0.1 mg ml^{-1} for another 1 hour incubation before being finally washed with water for 5 times.

Fluorescence imaging

Cells under observation were loaded onto either glass bottom plates (Cellvis P06-1.5H-N) or 35mm Glass bottom petri dishes (MatTek P35G-1.5-20-C). After an hour of incubation for cells to adhere, they were imaged on a Nikon Ti-Eclipse while incubated in a Tokai Stage Top Incubator maintaining a temperature of 37ºC and an atmosphere of 5% CO2.

Image analysis

Image analysis was conducted using techniques outlined by Rohith Rajasekaran and the Coyle lab (Rajasekaran et al., 2022).

Figures

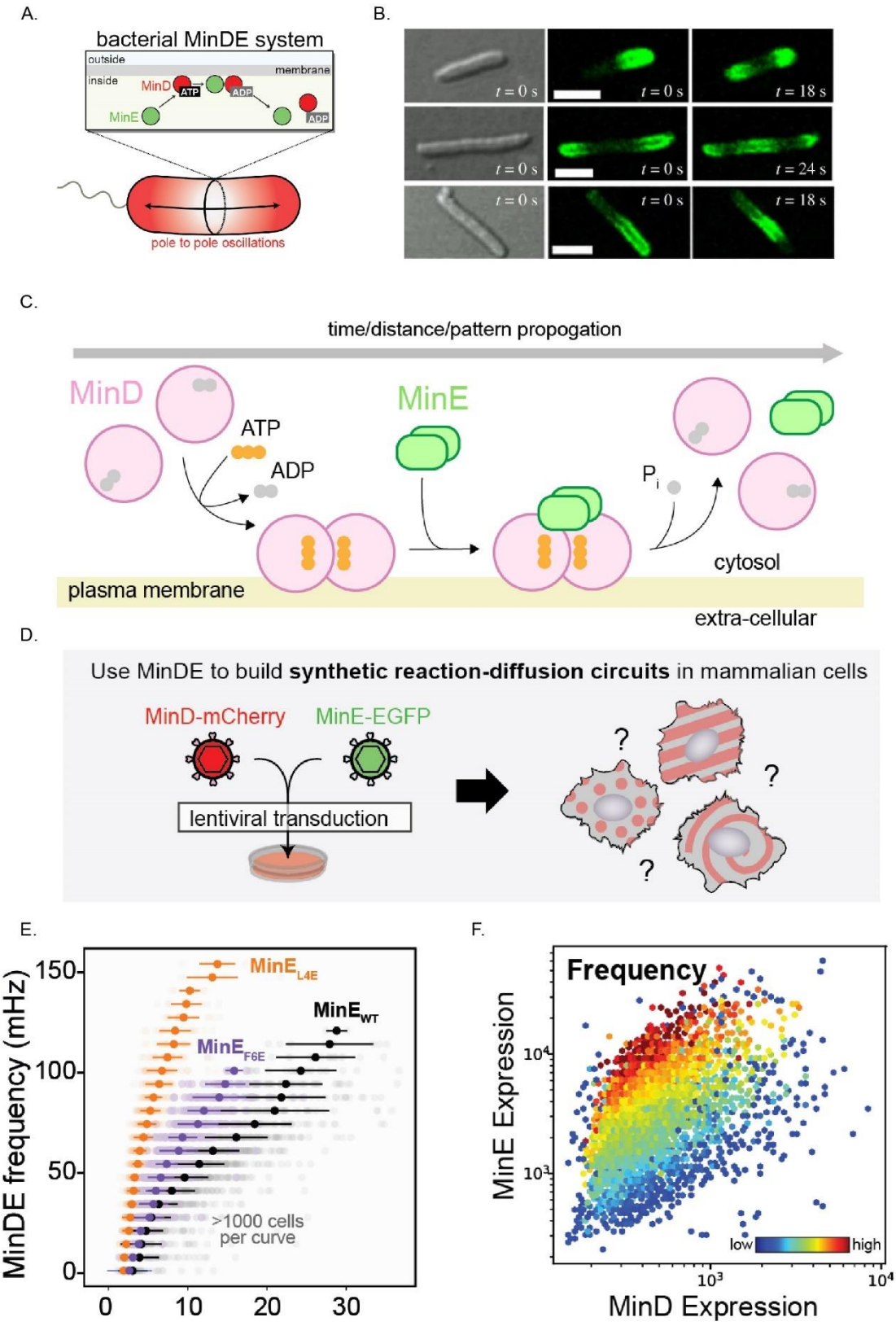
A.
bacterial MinDE system
outside
membrane
inside
MinD
ATP
ADP
MinE
ADP
pole to pole oscillations
B.
t = 0 s
t = 0 s
t = 18 s
t = 0 s
t = 0 s
t = 24 s
t = 0 s
t = 0 s
t = 18 s
C.
time/distance/pattern propogation
MinD
ATP
ADP
MinE
Pi
cytosol
plasma membrane
extra-cellular
D.
Use MinDE to build synthetic reaction-diffusion circuits in mammalian cells
MinD-mCherry
MinE-EGFP
lentiviral transduction
?
?
?
E.
MinE frequency (mHz)
150
100
50
0
0
10
20
30
MinE L4E
MinE WT
MinE F6E
>1000 cells per curve
F.
Frequency
MinE Expression
10^4
10^3
low
high
10^3
10^4
MinD Expression

Figure 1: The bacterial MinE-MinD reaction-diffusion circuit creates oscillating spatiotemporal patterns that can be used in mammalian cells.

A) The MinDE system primarily relies on the MinE protein stimulating hydrolysis of ATP by MinD, thus inhibiting its dimerization along the plasma membrane. This creates pole-to-pole oscillations in bacterial systems (Rajasekaran et al., 2022). B) Snapshots of oscillating MinD-GFP in *E. coli* cells (Sliusarenko et al., 2011). C) Hydrolysis reaction after MinE binds to MinD (Rajasekaran et al., 2022). D) Schematic for transducing the MinDE bacterial system into mammalian cells to induce spatiotemporal reaction-diffusion patterns (Rajasekaran et al., 2022). E) Modulating the frequency of the MinDE oscillations based on MinDE ratio and mutations (Rajasekaran et al., 2022). F) Frequency subpopulations of cells based on their ratio of MinDE (Rajasekaran et al., 2022).

A.

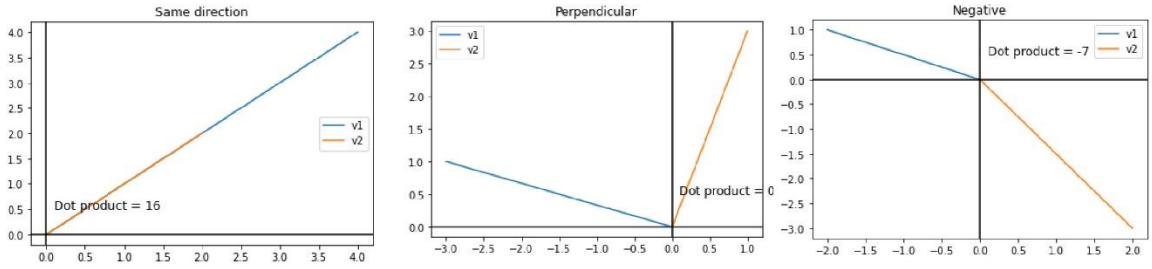
Same direction
Dot product = 16
v1
v2
Perpendicular
Dot product = 0
Negative
Dot product = -7

B.

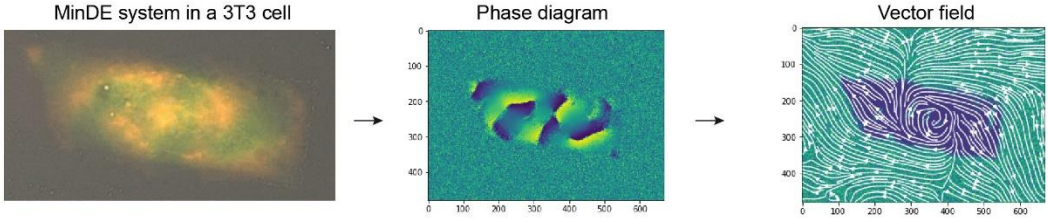
MinDE system in a 3T3 cell
Phase diagram
Vector field

C.

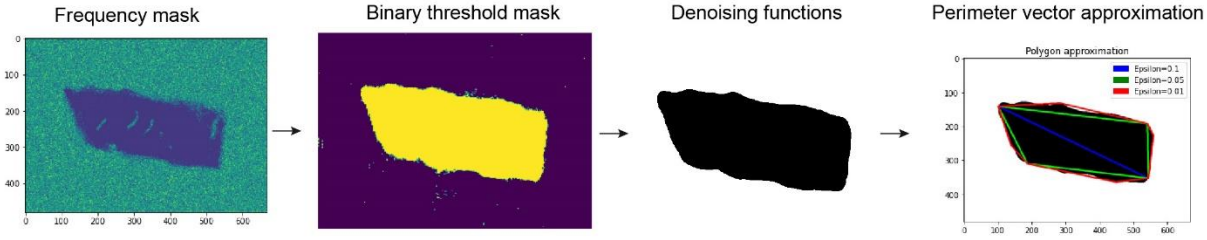
Frequency mask
Binary threshold mask
Denoising functions
Perimeter vector approximation
Polygon approximation

D.

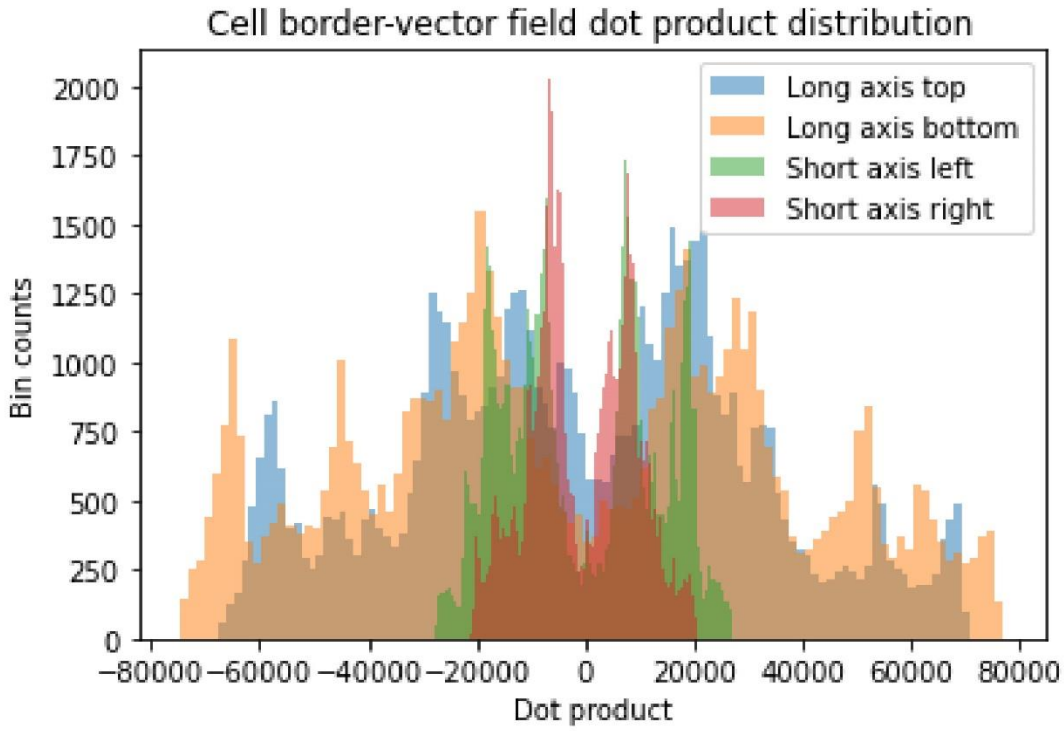
Cell border-vector field dot product distribution
Long axis top
Long axis bottom
Short axis left
Short axis right
Bin counts
Dot product

Figure 2: Surmising flow directionality from vector field dot product

A) Examples of different scenarios where dot product sign and value give insight on their relative orientations. B) Image processing from MinDE fluorescence signal oscillations from a 3T3 mouse fibroblast cell to phase diagrams via fast Fourier transform to vector fields. C) Isolating cell contours based on frequency and subjecting objects to binary thresholds and denoising to prepare for polygon approximation to extract perimeters of the cell as vectors. D) Distributions of dot products of pixel-level vectors within the cell against each of the four perimeter sides of the thresholded contour as vectors.

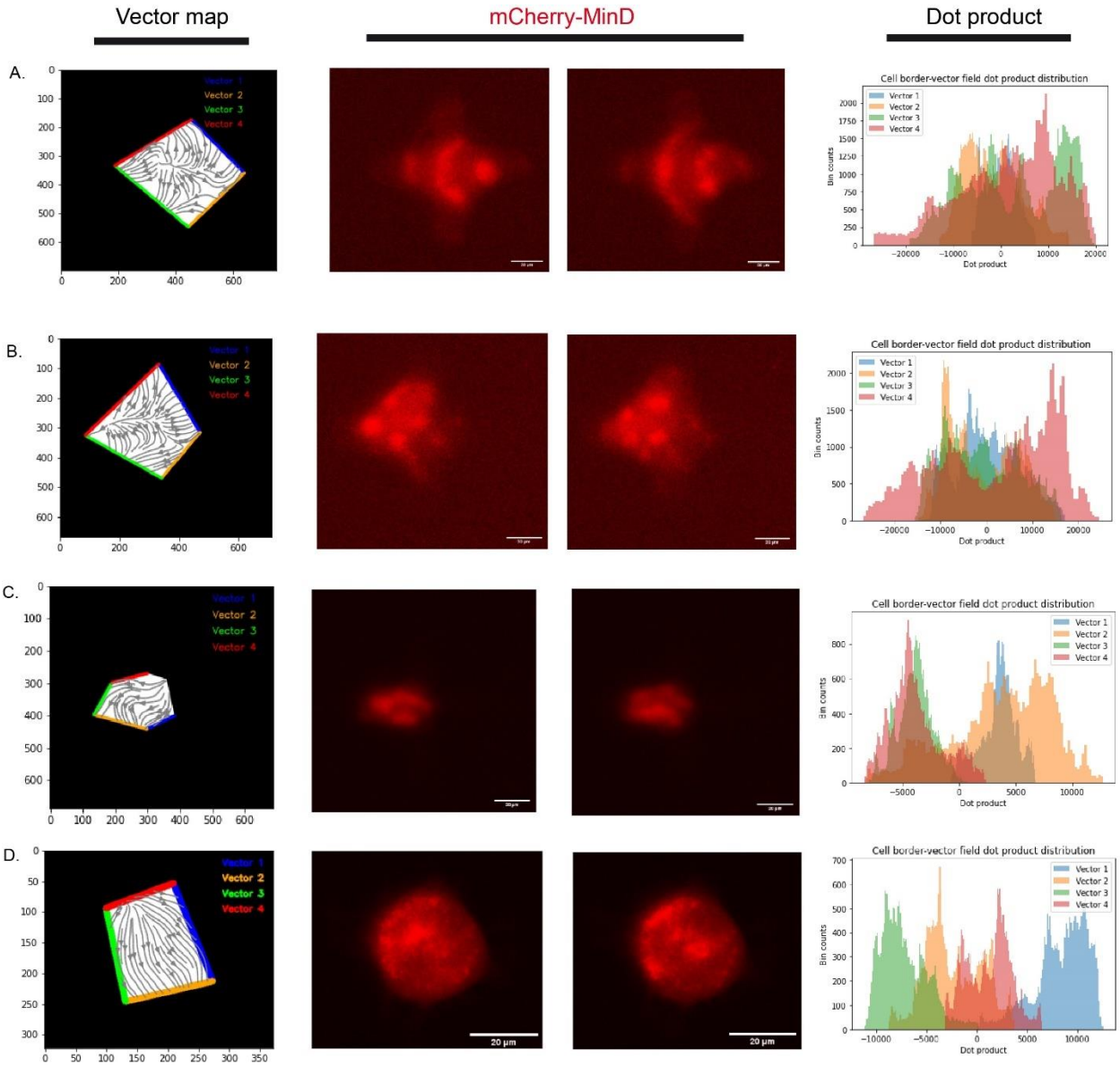
Vector map
mCherry-MinD
Dot product
A.
B.
C.
D.
Vector 1
Vector 2
Vector 3
Vector 4
Cell border-vector field dot product distribution
Bin counts
Dot product
20 µm

Figure 3: Dot product distributions of MinDE oscillating cell vector fields against their perimeters.

A) 3T3 mouse fibroblast cell with standing wave MinD oscillations, resulting in zero-centered distributions of vector field dot products with perimeters. B) Another example of a standing wave MinD oscillation pattern with a similar dot product distribution result. C) A cell exhibiting unidirectional MinD flow and vector field dot product distributions shifted away from zero. D) Another cell exhibiting unidirectional flow, with three out of the four vector field dot product distributions shifted away from zero.

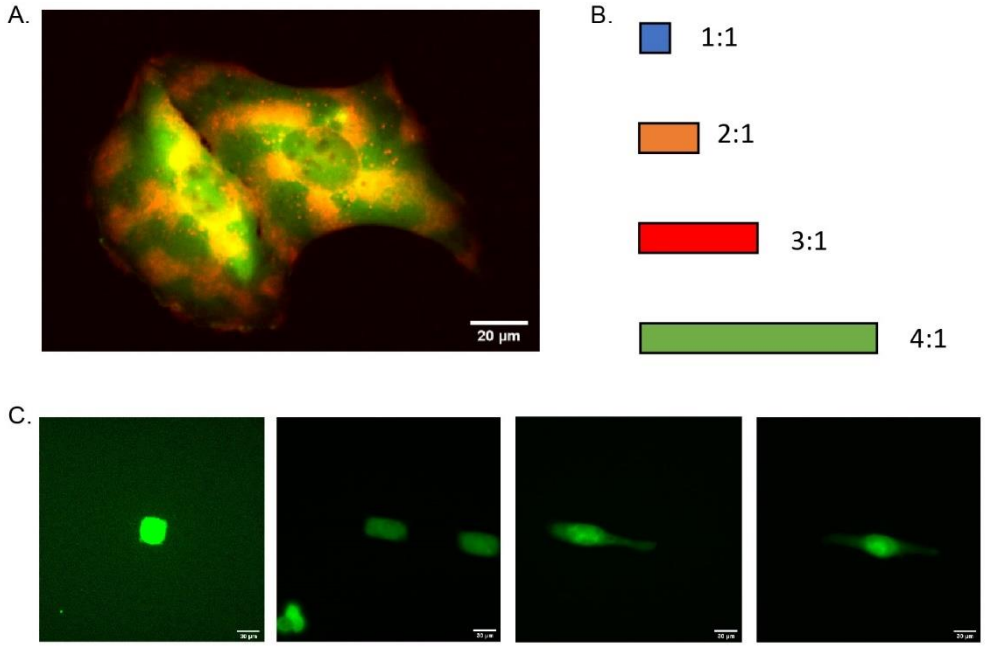
A.
20 µm
B.
1:1
2:1
3:1
4:1
C.

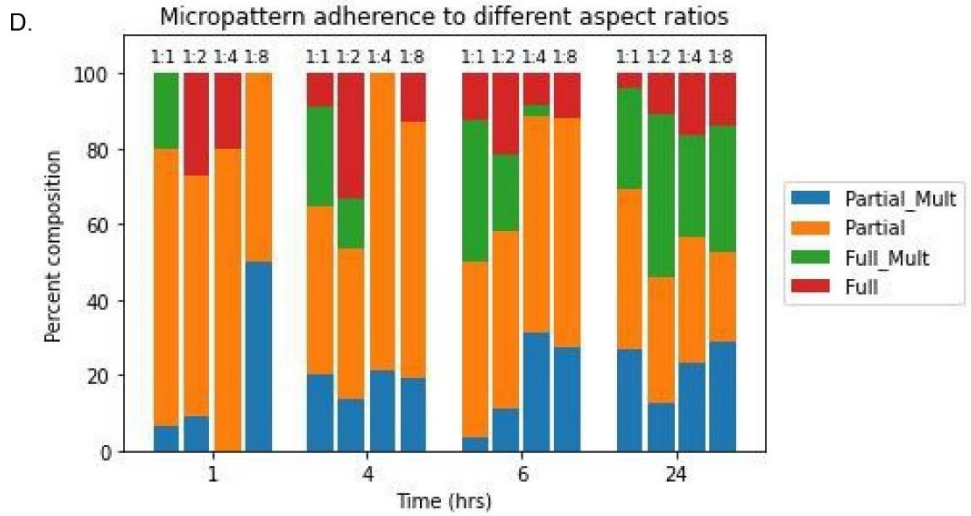
D.
Micropattern adherence to different aspect ratios
1:1 1:2 1:4 1:8
Percent composition
Time (hrs)
Partial_Mult
Partial
Full_Mult
Full

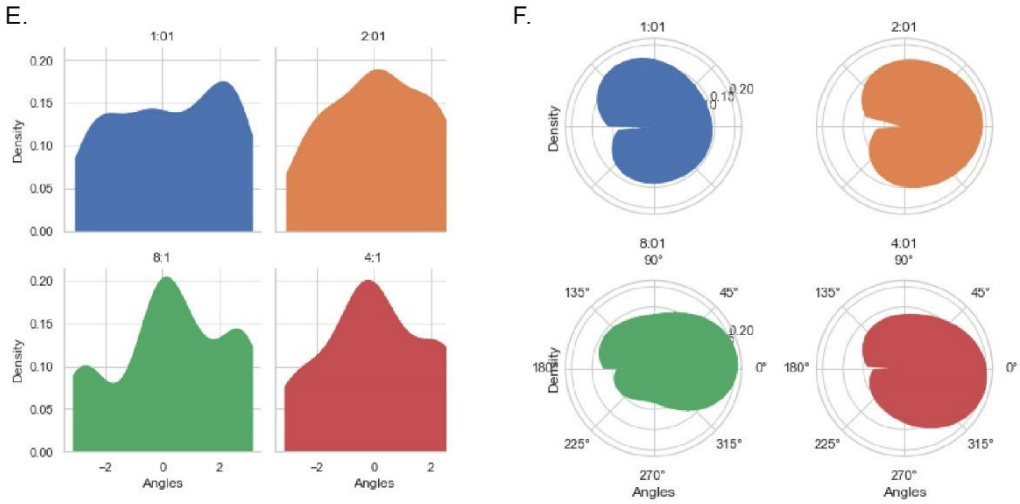
E.
1:01
2:01
8:1
4:1
Density
Angles
F.
8.01
4.01

Figure 4: MinDE 3T3 cells on different aspect ratio micropatterns

A) A mammalian cell oscillating with the MinDE system. MinE is visualized with a GFP reporter, and MinD is visualized with an mCherry reporter. B) Four different rectangular aspect ratios that will be used to create micropatterns with a constant area of 1800 μm^2. C) 3T3 MinDE cells on four separate micropatterns with the four different aspect ratios of 1:1, 2:1, 3:1, and 4:1. MinE is visualized with a GFP reporter. D) Percent composition of micropattern adherence to different aspect ratio micropatterns over the course of 24 hours. Partial_Mult refers to partial adherence of multiple cells to a micropattern. Partial refers to partial adherence of a single cell to a micropattern. Full_Mult references to multiple cells fully spreading over a micropattern. Full refers to one cell fully spreading over a micropattern. E) Density histogram plots of phase angles for cells grown on all four aspect ratios. F) Density histogram plots of phase angles in polar coordinates for cells grown on all four aspect ratios.

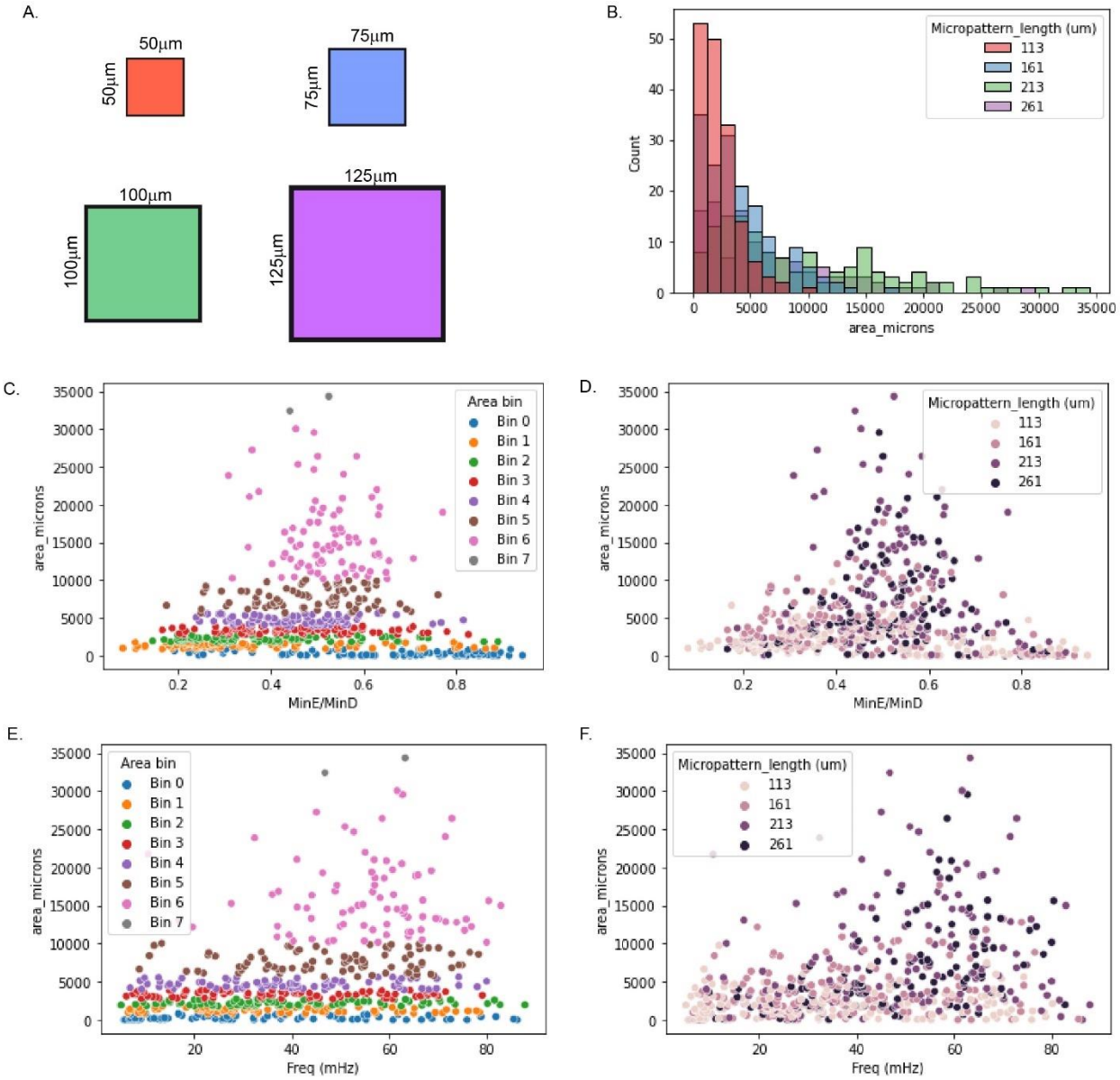
A.
50µm
50µm
75µm
75µm
100µm
100µm
125µm
125µm
B.
Micropattern_length (um)
113
161
213
261
Count
area_microns
C.
Area bin
Bin 0
Bin 1
Bin 2
Bin 3
Bin 4
Bin 5
Bin 6
Bin 7
area_microns
MinE/MinD
D.
Micropattern_length (um)
113
161
213
261
area_microns
MinE/MinD
E.
Area bin
Bin 0
Bin 1
Bin 2
Bin 3
Bin 4
Bin 5
Bin 6
Bin 7
area_microns
Freq (mHz)
F.
Micropattern_length (um)
113
161
213
261
area_microns
Freq (mHz)

Figure 5: Increasing area of square micropatterns influences spatiotemporal MinDE dynamics

A) A schematic of four different micropattern sizes, 50x50μm, 75x75μm, 100x100μm, and 125x125μm, to be used for adhering 3T3 MinDE cells. B) Distribution of cell areas based on the micropatterns cells were seeded on. C) MinDE ratios of cells binned by their area. D) MinDE ratios of cells binned by micropatterns cells were adhered to. E) Frequency of MinDE oscillations of cells binned by their area. F) Frequency of MinDE oscillations of cells binned by micropatterns cells were adhered to.

A.

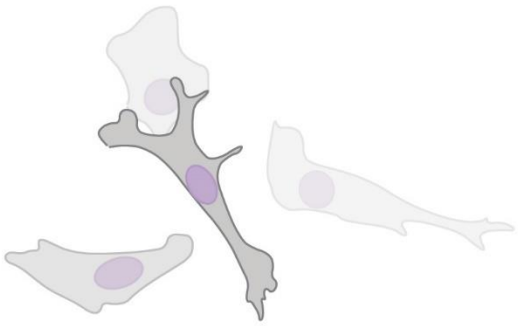

B.

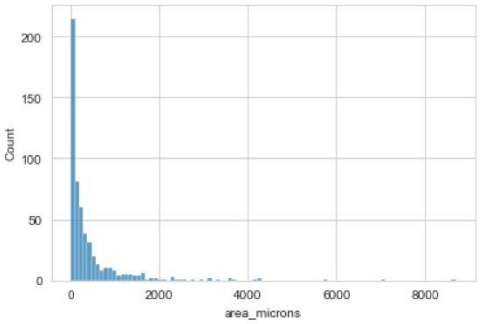
Count
area_microns

C.

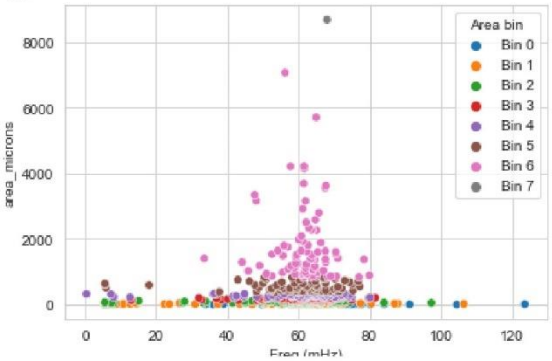
Area bin
Bin 0
Bin 1
Bin 2
Bin 3
Bin 4
Bin 5
Bin 6
Bin 7
area_microns

D.

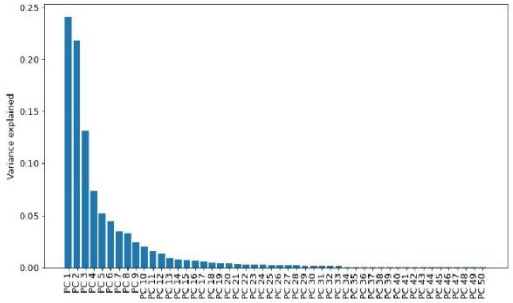
Variance explained

E.

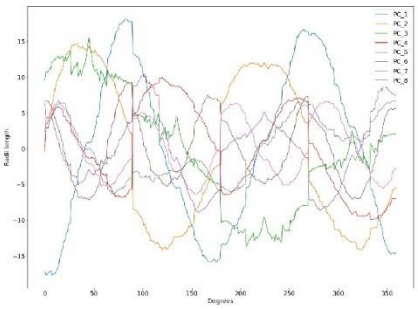

F.

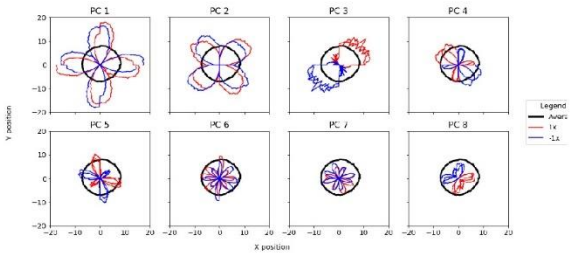
PC 1
PC 2
PC 3
PC 4
PC 5
PC 6
PC 7
PC 8
Y position
X position

G.

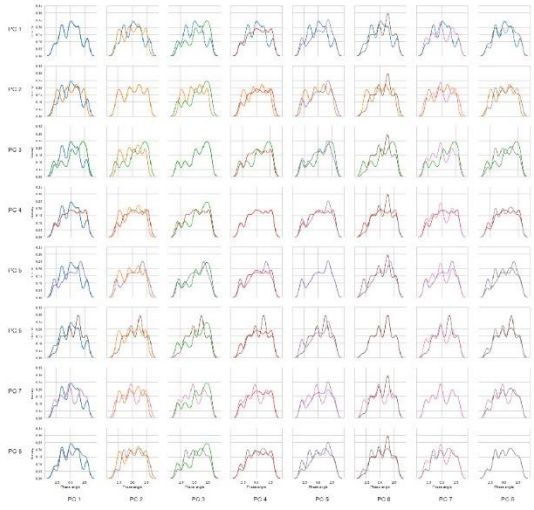

H.

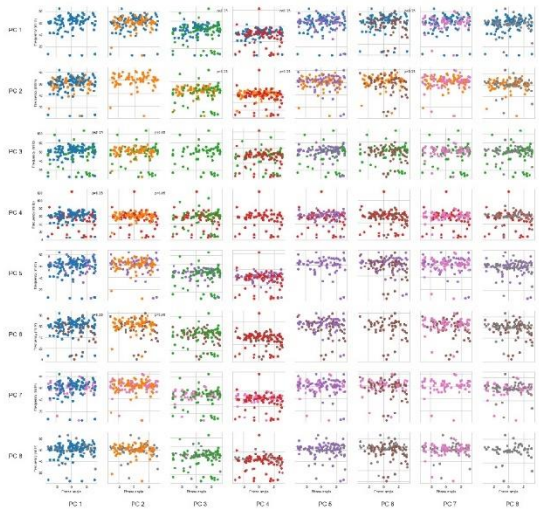

Figure 6: Relating unbound cell shape to MinDE oscillation parameters

A) Schematic of 3T3 cells growing on unbound glass substrate, displaying a wide variety of possible morphologies. B) Distribution of cell areas in μm^2 (n = 501). C) Frequency of MinDE oscillations of 3T3 cells binned by size. D) Variance in the deviation from the mean explained by the top 50 principal components from principal component analysis of the deviations from the cell shape mean for each cell. E) Polar coordinate representations of the top 8 shape modes. F) Cartesian coordinate representations of the top 8 shape modes multiplied by positive and negative scalars and added to the cell shape average. G) Vector field orientation distributions binned by maximum principal component. H) Phase angle against frequency of MinDE oscillation binned by maximum principal component.

References

Fofonjka, A., & Milinkovitch, M. C. (2021). Reaction-diffusion in a growing 3D domain of skin scales generates a discrete cellular automaton. *Nature Communications*, *12*(1), 1–13. https://doi.org/10.1038/s41467-021-22525-1

Kondo, S., & Miura, T. (2010). Reaction-Diffusion Model as a Framework for Understanding Biological Pattern Formation. *Science*, *329*(September), 1616–1620.

Park, K. T., Wu, W., Battaile, K. P., Lovell, S., Holyoak, T., & Lutkenhaus, J. (2011). The min oscillator uses MinD-dependent conformational changes in MinE to spatially regulate cytokinesis. *Cell*, *146*(3), 396–407. https://doi.org/10.1016/j.cell.2011.06.042

Rajasekaran, R., Chang, C.-C., Weix, E. W. Z., Galateo, T. M., & Coyle, S. M. (2022). A programmable reaction-diffusion system for spatiotemporal cell signaling circuit design. *BioRxiv*, 2022.11.15.516470. https://www.biorxiv.org/content/10.1101/2022.11.15.516470v1%0Ahttps://www.biorxiv.org/content/10.1101/2022.11.15.516470v1.abstract

Raskin, D. M., & de Boer, P. A. J. (1999). MinDE-Dependent Pole-to-Pole Oscillation of Division Inhibitor MinC in Escherichia coli . *Journal of Bacteriology*, *181*(20), 6419–6424. https://doi.org/10.1128/jb.181.20.6419-6424.1999

Rowlett, V. W., & Margolin, W. (2013). The bacterial min system. *Current Biology*, *23*(13), R553–R556. https://doi.org/10.1016/j.cub.2013.05.024

Sliusarenko, O., Heinritz, J., Emonet, T., & Jacobs-Wagner, C. (2011). High-throughput

subpixel precision analysis of bacterial morphogenesis and intracellular spatio-temporal dynamics. *Molecular Microbiology*, *80*(3), 612–627.

Strale, P. O., Azioune, A., Bugnicourt, G., Lecomte, Y., Chahid, M., & Studer, V. (2016). Multiprotein Printing by Light-Induced Molecular Adsorption. *Advanced Materials*, *28*(10), 2024–2029. https://doi.org/10.1002/adma.201504154

Wettmann, L., & Kruse, K. (2018). The min-protein oscillations in Escherichia coli: An example of self-organized cellular protein waves. *Philosophical Transactions of the Royal Society B: Biological Sciences*, *373*(1747). https://doi.org/10.1098/rstb.2017.0111

Chapter 4: Conclusion and future directions

Summary

Cell morphologies are essential to carry out important biological functions. For processes such as development, wound healing, and metastasis, specified polarizations and directed motility require certain morphologies that shift over time (Kulawiak et al., 2016; Poincloux et al., 2011; Théry & Bornens, 2006). Given the importance of morphological dynamics in biological processes, it is crucial to develop a generalizable method for quantifying these cellular shape changes.

I sought to optimize a micropatterning assay that would enable long periods of observation of single cell shape changes (**Appendix A**). I was able to determine concentrations of reagents, lengths of incubation periods, UV light intensities, and types of geometric patterns that would be ideal for this kind of analysis. While certain cell types and experimental conditions weren't compatible with the assay, a number of cell types and conditions had adherent cells that were compatible with the micropatterning assay.

Using this optimized micropatterning procedure, I was able to test how different sizes and spatial complexities of substrates affected the morphological dynamics of 3T3 mouse fibroblast cells and a panel of triple-negative breast cancer cells (**Chapter 2**). Subjecting the 3T3 cells to a range of sizes from 30 to 60μm resulted in a check-mark response where cells exhibited more frequent morphological events at 30μm and 60μm with a slight dip at 40μm. It was hypothesized that at lower sizes, the cell was unable to have ample space to spread out and was more morphologically unstable as a result. Meanwhile at the larger extremity, there was plenty of surface area of the substrate for

the cell to extend and contract frequently. Spatial complexity appeared to play a role in biasing the orientation of the morphological events relative to the micropattern, with large micropatterns with lower spatial complexity exhibiting higher alignment between the petal lobes of the micropattern and the centroid of the morphological event. Buoyed by these results, I applied the same micropatterning technique and image analysis pipeline to a panel of triple-negative breast cancer cells to see if the assay could parse out different axes of characteristic morphological dynamics between the different cell types. The frequency, span, and alignment of events were all found to have differing levels depending on the cell type. MDA-MB-231 cells, for example, were found to have higher frequency of events, along with higher event alignment with micropatterns.

Finally, to demonstrate the generalizability of the approach for adherent cells, I sought to apply micropatterning to other applications and evaluated how changing cell size and shape would affect the MinDE reaction diffusion system (**Chapter 3**). I found that the aspect ratio of cell shape can bias the directionality of traveling wave vector fields, and that increasing the size of a cell can narrow the range of frequencies. Additionally, unbound cells can be categorized by maximum principal component bins, demonstrating different frequencies depending on the principal component subpopulation. This work overall shows that micropatterning in concert with image analysis can be a powerful tool to study how cell shape changes are influenced by the spatial environment and how cell shape can change important internal cellular processes.

Future Directions

In **Appendix A**, we developed a micropatterning assay to isolate adherent cells for timelapse microscopy experiments. While we were able to successfully use the assay for adherent cells including 3T3 mouse fibroblast cells, there were experimental conditions including starvation and other cell types, such as the MDA-MB-453 and H1395 cells, that were unable to adhere to the micropatterns. In our assay, we only used commercially available fibronectin, but there exist a variety of different isoforms and types of fibronectin, as well as many different types of structural proteins in the ECM (Dalton & Lemmon, 2021). Future efforts could employ different kinds of fibronectin, such as plasma fibronectin, produced by hepatocytes, versus cellular fibronectin, produced by more cells such as chondrocytes and fibroblasts or fibronectin isoforms that are spliced along different domains (Dalton & Lemmon, 2021). Testing a panel of different substrates could expand the applicability of micropatterning by potentially enable adhesion even for cells that do not adhere to standard fibronectin.

In **Chapter 2**, we assessed morphological dynamics of 3T3 cells and a panel of triple-negative breast cancer cells against an array of micropatterns with varying size or spatial complexity. However, the biochemical origin of these different phenotypes was unexplored and has high potential for future investigation. Using a CRISPRi/a screen on potential candidates for cell shape regulation, such as RhoGEF, could yield insights on the molecular underpinnings responsible for these differences in morphological dynamics between cell lines and experimental conditions (Gilbert et al., 2013; Pascual-Vargas et al., 2017). The process of adhesion largely relies on focal adhesions,

multifunctional organelles comprised of over 150 different known proteins (Kuo et al., 2011). Many of these proteins serve a wide range of diverse functions, including GTPases, modulators of GTPases, kinases, phospholipases, phosphatases, adapter proteins, and cytoskeletal-binding proteins. The composition of focal adhesions are heterogeneous and dynamic, suggesting that different extracellular contexts either require or evoke these different compositions (Kuo et al., 2011). For nascent adhesions, integrin requires activation by talin, along with the recruitment of tyrosine kinase focal adhesion kinase and the adapter paxillin and the integrin-talin-actin link strengthening agent vinculin. Downstream pathways include actin bundling through accumulation of adapter proteins tensin and zyxin, along with elongation of actin through the mediation of formin (Kuo et al., 2011). Interestingly enough, the compositional changes of focal adhesions were found to be largely mediated through β-Pix, a Rac1 guanine nucleotide exchange factor (GEF), specifically through negatively regulation maturation of focal adhesions through Rac1 promotion of activation, along with increasing nascent adhesion turnover and the protrusion of lamellipodia (Kuo et al., 2011). Due to the mechanosensing function of focal adhesions providing the link between the spatial aspects of extracellular substrate and the internal architecture of the cell, it would be of high interest for future efforts to silence, upregulate, or downregulate expression of key players in focal adhesion formation and regulation. Through these efforts, future researchers could examine which agents appear to be most crucial for sensing geometric patterns in micropatterns, such as the spatial complexity through the number of lobes or even the size of the micropattern. Transcriptional screens of cells exposed to different micropatterns could also yield insights on the major players responsible for

processing spatial information and using that information to guide decisions on cell shape (Koenig et al., 2022).

In **Chapter 3**, we explored how the shape of the cell could influence the MinDE reaction-diffusion system. We were able to show how the aspect ratio could change the direction of traveling wave flow and how the size of the cell changes the range of oscillatory frequencies. However, we weren't able to detect if specific shapes or sizes of the cell could change the types of spatiotemporal patterns that arose. All of the analysis depended on isolating cells as contours if they displayed an oscillatory frequency, leaving out stationary MinDE islands or other kinds of non-oscillatory spatiotemporal patterns. A machine learning pipeline could be developed to identify cells and classify them based on the types of patterns that arise (Yonekura et al., 2021). It would require developing a training set of data, with preset classifications of different kinds of patterns. After the different classes of patterns are identified, then the machine learning pipeline can be used for future applications asking questions how the shape of the cell could change the types of MinDE patterns that are expressed.

Overall, the work in this thesis optimized techniques and generated new datasets and analysis pipelines that further our understanding of how the morphology of metazoan cells fluctuate depending on the spatial environment. We developed a micropatterning assay that could isolate single cells of adherent cells for long periods of observation (**Appendix A**). We used this assay to test how adhering a panel of metazoan cells on micropatterns of differing size and spatial complexity would yield characteristic event phenomenon statistics (**Chapter 2**). Finally, we used micropatterning to assess how the shape of cells could influence MinDE spatiotemporal

patterns. These findings will provide future researchers with tools to assess morphological dynamics of metazoan cells over time and hopefully lead to diagnostic tests that could aid the characterization of adherent cancer cells.

References

Dalton, C. J., & Lemmon, C. A. (2021). Fibronectin: Molecular structure, fibrillar structure and mechanochemical signaling. *Cells*, *10*(9). https://doi.org/10.3390/cells10092443

Gilbert, L. A., Larson, M. H., Morsut, L., Liu, Z., Brar, G. A., Torres, S. E., Stern-Ginossar, N., Brandman, O., Whitehead, E. H., Doudna, J. A., Lim, W. A., Weissman, J. S., & Qi, L. S. (2013). CRISPR-mediated modular RNA-guided regulation of transcription in eukaryotes. *Cell*, *154*(2), 442. https://doi.org/10.1016/j.cell.2013.06.044

Koenig, A. L., Shchukina, I., Amrute, J., Andhey, P. S., Zaitsev, K., Lai, L., Bajpai, G., Bredemeyer, A., Smith, G., Jones, C., Terrebonne, E., Rentschler, S. L., Artyomov, M. N., & Lavine, K. J. (2022). Single-cell transcriptomics reveals cell-type-specific diversification in human heart failure. *Nature Cardiovascular Research*, *1*(3), 263–280. https://doi.org/10.1038/s44161-022-00028-6

Kulawiak, D. A., Camley, B. A., & Rappel, W. J. (2016). Modeling Contact Inhibition of Locomotion of Colliding Cells Migrating on Micropatterned Substrates. *PLoS Computational Biology*, *12*(12). https://doi.org/10.1371/journal.pcbi.1005239

Kuo, J. C., Han, X., Hsiao, C. Te, Yates, J. R., & Waterman, C. M. (2011). Analysis of the myosin-II-responsive focal adhesion proteome reveals a role for β-Pix in negative regulation of focal adhesion maturation. *Nature Cell Biology*, *13*(4), 383–395. https://doi.org/10.1038/ncb2216

Pascual-Vargas, P., Cooper, S., Sero, J., Bousgouni, V., Arias-Garcia, M., & Bakal, C.

(2017). RNAi screens for Rho GTPase regulators of cell shape and YAP/TAZ localisation in triple negative breast cancer. *Scientific Data*, *4*, 1–13. https://doi.org/10.1038/sdata.2017.18

Poincloux, R., Collin, O., Lizárraga, F., Romao, M., Debray, M., Piel, M., & Chavrier, P. (2011). Contractility of the cell rear drives invasion of breast tumor cells in 3D Matrigel. *Proceedings of the National Academy of Sciences of the United States of America*, *108*(5), 1943–1948. https://doi.org/10.1073/pnas.1010396108

Théry, M., & Bornens, M. (2006). Cell shape and cell division. *Current Opinion in Cell Biology*, *18*(6), 648–657. https://doi.org/10.1016/j.ceb.2006.10.001

Yonekura, K., Maki-Yonekura, S., Naitow, H., Hamaguchi, T., & Takaba, K. (2021). Machine learning-based real-time object locator/evaluator for cryo-EM data collection. *Communications Biology*, *4*(1), 1–8. https://doi.org/10.1038/s42003-021-02577-1

Appendix A: Optimizing micropatterning to isolate adherent mammalian cells.

John Ahn[1] and Scott Coyle[1].

[1]Department of Biochemistry, University of Wisconsin-Madison, Wisconsin, USA

Disclaimer

This work was submitted to bioRxiv. J.A. is the sole first author of this publication.

Author contributions

J.A. and S.C. conceptualization; J.A. and S.C. methodology; J.A. and S.C. formal analysis; J.A. and S.C. investigation; J.A. and S.C. writing—original draft; J.A. and S.C. writing—review & editing.

Abstract

Cells on unbounded substrates dynamically move through a rich array of cellular morphologies. These diverse geometries can be difficult to analyze over time due to a lack of a common framework for comparison between different cells, as well as their constant motion. As a solution, micropatterning techniques fix cells to specific geometries patterned onto a glass substrate, providing both a physically constrained area for consistent observation and a reference point for comparison with an underlying shape for comparing the morphologies of cells between different trials and experimental conditions. We developed a micropatterning protocol for adherent cells, using a harmonics of a circle equation to generate shapes with varying spatial complexities that would approximate different directional axes a cell could polarize along *in vivo*. While 3T3 mouse fibroblast cells and breast cancer cell lines readily adhered to fibronectin micropatterns, other cell lines tested, such as lung cancer cells, did not selectively adhere to the micropatterns. For the adherent cells, over the course of time-lapse microscopy experiments, they demonstrated dynamic shape variations with an average shape closely resembling the underlying lobes of micropatterns. The development of this micropatterning technique provides a tool for analyzing morphologies of adherent cells over time, which can yield information about their dynamics and underlying biological processes.

Introduction

Cells adopt a diverse array of morphologies for a variety of biological applications. Different aspects of the extracellular environment, including shear stress, mechanical force, and substrate composition can also influence cellular shapes (Alvarez & Smutny, 2022; Gonzalez-Molina et al., 2019; Malek & Izumo, 1996). Due to their biological significance, many efforts have been undertaken to quantify cellular morphologies, in contrast to traditional qualitative statements made early in the field of microscopy. These mathematical techniques, paired with experimental techniques such as micropatterning, have enabled highly specified workflows for quantitatively assessing cellular morphologies over time.

Depending on the tissue, stage of development, location, and function, cells exhibit a wide range of different shapes. Neuronal cells in mammals have similar basic organizations but depending on their location in the brain layer, exhibit a variety in size and cilia. Humans have six general layers in the brain. Three major subclasses of glutamatergic excitatory neurons include pyramidal intracerebral projection neurons, which typically have one long extension pointing towards the first layer and three smaller extensions, spiny stellate cells, which localize in only one layer, are typically smaller in size, and have a horseshoe projection, and pyramidal subcerebral projection neurons, which are in the higher layers, are relatively larger, and can vary in number of large projections (Miller et al., 2019).

During neuronal development, the morphology of cells from progenitor cells to different kinds of neurons and astrocytes varies drastically. Spherical intermediate progenitor cells are derived from ventricular radial glia, which are characterized by their

elongated axons reaching from the ventricular zone all the way up to the choroid plexus (Miller et al., 2019). Later during their development stage, intermediate progenitor cells can further differentiate into deep layer and upper layer neurons with dendrites and axon terminals (Miller et al., 2019). These examples demonstrate how subclasses of cells can show drastically different morphologies depending on their biological function, location within tissue, and development stage.

Even cells that are the same type and are responsible for the same functions display a wide distribution of morphological shapes and sizes. Embryonic mouse fibroblast 3T3 cells are present in connective tissues, determining tissue architecture by producing macromolecules within the extracellular matrix (Plikus et al., 2021). Though the cells were passaged from the same NIH 3T3 cells, one study found heterogeneity in the types of morphologies that arose from the cells. Spindle-shaped fibroblasts with elongated and thin shapes were interspersed with more cub-shaped cells that appeared somewhat larger (Rahimi et al., 2022). Amongst the spindle-shaped fibroblast, many cells displayed different geometric parameters, varying in overall size, orientation, number of extensions, length of extensions, width of lamellipodia, roundedness, and angularity (Rahimi et al., 2022). With such varied morphologies, quantifying cell shape dynamics while they are migrating on unbound substrate can be a difficult endeavor. Additionally, on unbound substrate, the cells had essentially infinite directions in which to polarize or migrate, moving on top of or under each other, as well as in and out of frame of the microscope.

In order to circumvent these issues, many researchers turn to micropatterning to fix cells in one area and provide a common frame of reference for comparing the

morphologies of the cells. Micropatterning allows for the precise fabrication of micrometer scale spatial patterned substrate surfaces for cells to adhere to (Strale et al., 2016). Because the cells can only adhere to the micropatterned area, they are bound and cannot collide into other cells or move out of frame, greatly easing the burden of tracking the cell over time for dynamic shape studies. Furthermore, the shape itself is an effective frame of reference for comparing morphologies over time. A center point can be used to do a radial polar coordinate sweep to calculate the cell outline radii. Architecture of the shape, such as the number, location, or angle of apices can all be used as reference points to analyze how those kinds of spatial parameters could potentially have an effect on the cell polarity, types of extensions, and morphological features.

Given these findings from previous studies, we built a micropatterning pipeline for systematically assessing how spatial complexity and size could change morphologies of different cell lines. The spatial complexity was based on a polar equation of circular harmonics (Eq 1).

$$r = d + a \bullet \cos(k\theta) \qquad (1)$$

This equation produces flower-petal-like lobes that increase in number according to the ‘k’ parameter, which we harnessed as a proxy for a potential directional axis for cell polarization (**Fig. 1A**). Size could be modulated by concurrently increasing or decreasing the ‘d’ and ‘a’ parameters (**Fig. 1B**). After plating cells onto different micropatterns, we found that the average shape of the cell morphologies over the course of the entire experiment mostly approximated the shape of the underlying pattern, with variations deviating from that average shape occurring throughout the

experiment. While some cell lines, including the 3T3 cells and all of the breast cancer cell lines, some cell lines such as the NCI-H1395 lung cancer cells were not able to readily adhere to the micropatterns, demonstrating the limitations of the assay for cells that can adhere to the passivated PEG surface.

Results

Metazoan cells on unbound substrates exhibit highly varied morphologies and migratory trajectories

3T3 Mouse fibroblast cells were seeded onto unbound glass substrate and observed via DIC microscopy (**Fig. 2A**). Individual cells displayed an extensive repertoire of morphologies over the span of hours, extending filopodia and lamellipodia as they migrated across the surface, unimpeded (**Fig. 2B**). Keeping track of individual cell movement and shape changes over time from a qualitative point of view proved to be challenging. From a wider field of view, the 3T3 cells demonstrated even more variable behavior.

When observing groups of 3T3 cells, it was clear that future efforts for tracking and characterizing shape dynamics would be prove to be computationally challenging. Cells changed shape geometries on the scale of minutes, with no easily identifiable landmarks as a reference point for futures comparisons. Neighboring cells would frequently make contact, either traveling side-by-side, on top of, or below other cells as they moved across the glass (**Fig 2C**). Additionally, cells had a tendency to move in and out of frame, which would make tracking individual cells for future analysis difficult from a methodological perspective.

Actin cytoskeleton and nuclei staining revealed some of the molecular machinery required to contort the cell into such varied geometries and also enable locomotion. Stretched out cells showed long filamentous actin cables stretching across the extensions, along with focal adhesions dotted throughout the cell membrane in contact with the glass substrate to generate traction (**Fig. 2D**). These fluorescence images

illustrate the complicated coordination between intracellular agents, cell-membrane proteins, and extracellular environments required for the sensing of extracellular cues and subsequent morphological changes in response.

Growing cells on unbound substrate results in several disadvantages for potential analysis. Cells tend to move in and out of frame, overlap with neighboring cells, and also do not have a common frame of reference for morphological comparison. In order to circumvent these issues and simplify future quantification of cellular shape dynamics, we turned to micropatterning as a technique to isolate cells in a highly specified and systematic manner.

Optimization of the micropatterning methodology was necessary for successful cell adherence and subsequent microscopy observation.

Micropatterning involves the creation of micron-scale adhesive islands to which cells can adhere. For our application, we leveraged the high specificity of the technique to fabricate adhesive islands on the scale of typical 3T3 cell sizes in order to isolate them for analysis. The underlying micropattern provided a natural point of reference for morphological comparison.

The micropatterning technique involves several layering steps to create the adhesive islands (**Fig. 3A**). The anti-fouling coating agent prevents any proteins, exogenous materials, or cells from binding to the glass substrate. In order to create the desired micropatterns, a photoinitiator is added and activated by UV light that is shined through a DMD mirror array that will let light through in a highly specified manner on the

micron scale. Once activated in the desired geometries by the UV light, the photoinitiator will ablate the anti-fouling coating agent, creating a negative space in the shape of the desired geometry. An adhesive substrate, in our case we used fibronectin, is added to fill in that negative space, thus creating an adhesive island for cells to bind to, surrounded by anti-fouling coating agents that the cell cannot bind to. Micropatterning requires balancing concentrations between the anti-fouling coating PEG layer, photoinitiator required to ablate the PEG layer, UV light strength to activate the photoinitator, and fibronectin concentration for cell adherence.

In addition to UV light strength, one element of the UV light illumination that must be taken under consideration is the Z-axis level of illumination on the microscope when micropatterning. For example, when illuminating the UV light with a few dozen micron offset from the glass bottom of the plate, interference patterns arose, disrupting formation of the micropatterns (**Fig. 3B**). After adjusting the Z-axis to have 0 offset from the glass bottom, the interference patterns were mostly eliminated, and the micropatterns exhibited a crispness that for the most part resembled the desired micropattern geometries (**Fig. 3C**). Although the entire UV strength range from 30 mJ mm^{-2} to 120 mJ mm^{-2} resulted in noticeable micropatterns, we needed to test if the adherence of cells would change along this range.

In order to test cell adherence, we made k-value = 4 micropatterns using the same 30-240 mJ mm^{-2} UV light range and seeded 3T3 cells onto the resulting micropatterns (**Fig. 4A**). During this trial, it was difficult to see resulting micropatterns at 30 mJ mm^{-2} and 60 mJ mm^{-2}. Additionally, no cells adopted a spread phenotype, with all of them showing balled phenotypes. However, at 120 mJ mm^{-2} and 240 mJ mm^{-2}, the

micropatterns showed up clearly. The cells seeded on micropatterns created using these UV light intensities were also able to adhere to the micropatterns, showing spreading phenotypes. Cells that landed on areas outside of the micropattern mostly showed balled phenotypes, showing that the anti-fouling coating agent was working effectively.

If the PEG layer concentration is too high, then the photoinitator or UV light may not be strong enough to ablate the anti-fouling coat layer. If the fibronectin concentration is too low, the cell won't be able to easily form focal adhesions and gain traction on the micropattern. If the fibronectin concentration is too high, the protein may form polymer chains atop the anti-fouling coat layer, giving a layer of scaffolding for the cell to adhere to beyond the desired micropattern locations. The seeding of cells also requires a certain amount of precision in order to not overcrowd the micropatterns.

To address the fibronectin issue, different concentrations of the substrate were tested along with spin times and assessed using 3T3 adherence ratio. Spin times of fibronectin at 5,000 x g were tested because the protein had a tendency to crash out of solution and so the remaining supernatant was used for passivating substrate. Three spin conditions, 0, 5, and 60 minutes, were tested along with two concentrations for each, 10µg/ml and 100µg/ml (**Fig. 5A**). Regardless of spin condition, the 100µg/ml concentration almost always led to worse 3T3 adherence per micropattern. From then on, 10µg/ml was the standard concentration used to create the fibronectin micropatterns. Amongst the spin times, 5 minutes led to the best results for 3T3 adherence, with 60 minutes in the middle, and the 0 minute spin condition resulting in the worst adherence for 3T3 cells. The signal-to-noise ratios, based on the NeutrAvidin

fluorescence signal, were also assessed under the same conditions (**Fig. 5B**), and it was found that there was no difference based on the spin times or concentration of fibronectin, suggesting that the tracer molecule's ability to passivate to the glass surface was unaffected by the fibronectin concentration.

The number of cells seeded was also assessed. If too many cells are seeded, micropatterns can be overcrowded with multiple cells, complicating analysis and defeating the purpose of micropatterning as a single-cell isolation technique. One example image with k-value 3 micropatterns (**Fig. 6A**) and 3T3 cells (**Fig. 6B**) demonstrates how overseeding can lead to multiple cells adhered to the micropatterns. Micropatterns were incubated with either 20,000 cells or 40,000 cells (**Fig. 5C**). Although the 40,000 cell seeding number resulted in a higher number of attached and spread cells, it also resulted in more multiple cell adherence, and so 20,000 seeding number was used for standard procedure.

To get an idea for ideal k-value and pattern diameter size for cell adherence, an array of petal number and micropattern sizes were created and tested with 3T3 cells (**Fig. 5D**). Cell adherence at 10μm was extremely low, suggesting that was the lower limit for micropattern size for 3T3 cells, and that they would need a larger area of substrate to attach to the fibronectin. At 20μm and 30μm, 3T3 cells were much more able to adhere to the micropatterns, although there were a few k-value conditions where cells struggled to adhere to the micropatterns at the 30μm diameter size. Cell adherence was noticeably higher at 40μm than any of the other conditions across all of the k-values surveyed at k = 2, 3, 4, 10, and 12. Interestingly enough, within the 40μm

sized micropatterns, k-value 4 seemed to have the best adherence out of all the petal numbers, suggesting that spatial complexity could have an effect on cell adherence.

To assess whether or not characteristics of internal cytoskeletal structures of cells on unbound glass substrate were recapitulated on micropatterns, we transduced a LifeAct-GFP construct using a lentivirus into 3T3 cells. The fluorescently labeled LifeAct reporter binds to the cytoskeleton, giving a readout of the internal architecture of the cell (Riedl et al., 2008). When unbound, the cell forms large, fanned out morphologies, indicative of motility phenotypes, as well as a variety of different kinds of geometries (**Fig. 7A**). In addition to their overall morphologies, the cytoskeletal structures revealed through the LifeAct-GFP reporter demonstrated networks of actin fibers forming cables across the span of the entire cell. Cells with the fan-like morphologies indicative of a cell in motion tended to have fibers bunching together at the distal end away from the direction of motion and fanning out across the lamellipodia on the opposite side of the fibers. Cells that did not appear to be in motion tended to have stress fibers stretching across the perimeter of the cell edge. Puncta were also visible in a number of cells. Many of these characteristic cytoskeletal features were replicated in the cells adhered to micropatterns. LifeAct-GFP 3T3 cells grown on micropatterns also exhibited stress fibers stretching either across the center of the cell or along the edges or even in the fan-like configuration seen in the unbound cells (**Fig. 7B**). This suggests that many of the polarizations, extensions, and also contractions that are present in unbound cells would also be present in cells adhered to micropatterns, demonstrating that the technique is a useful proxy for extracellular matrix substrate geometries that allow for essentially limitless morphological possibilities.

Through optimizing different concentrations and intensities of different steps in the micropatterning process, we were able to successfully develop an assay for isolating and analyzing the morphological dynamics of adherent cells over long periods of time. Many of the morphological characteristics of interest seen in unbound cells were also seen in micropattern-adhered cells, suggesting it is a relevant proxy for recapitulating ECM environments. However, while cells like 3T3 mouse fibroblasts are prime candidates for micropatterning, certain cell lines and experimental conditions were found to disqualify micropatterning for some applications.

Micropatterning is not optimal for cell lines or experimental conditions

Although micropatterning is a powerful technique for isolating cells and subjecting them to highly specified substrate geometries, it is limited to cells that are able to preferentially adhere to the micropatterns. After some experimentation with different media conditions and different cell lines of interest, it was clear that not all cells can be used with micropattern to full effect.

As cells *in vivo* are exposed to all kinds of gradients in the extracellular environment, one experimental parameter of interest was looking at nutrient conditions and how cellular morphology would change as a result. In preliminary experiments where cells were grown in DMEM media with 0% serum, cells qualitatively displayed noticeably different morphologies (**Fig. 8A**). Compared to normal 3T3 cells, the extensions took on a more thin and ragged appearance, more resembling branched spiderwebs as opposed to the more full-bodied, round, and thicker extensions normally

seen on 3T3 cells. While this was an initially encouraging result, as it was clear that modulating the nutrient levels of the media resulted in an obvious change in phenotype, it was clear that the starved cells had a clear propensity to bind to the anti-fouling coating agent as well (**Fig 8A**). Cells were binding indiscriminately to both micropatterns and areas with just the anti-fouling coating agent, which would make any conclusions drawn about how the spatial complexity of the micropatterns could affect the morphology of the cell circumspect. This is due to the fact that if the starved cell can bind equally well to the anti-fouling coating agent and the micropatterns, then the micropattern is unlikely to be directly affecting the morphologies the cell is displaying, and instead the morphologies displayed can really only be attributed to the media conditions. It would also make isolating cells and preventing their movement in and out of frame over the course of an experiment into a challenging problem.

To check that the serum conditions were indeed responsible for the cells enhanced adherence to even the PEG layer, 3T3 cells were grown for 24 hours either with or without serum. When cells from both conditions were seeded onto micropatterns, cells grown with serum were able to bind to micropatterns, but they displayed a round phenotype on the PEG layer, unable to spread (**Fig. 8B**). In contrast, cells grown without serum were able to indiscriminately bind to both micropattern and PEG areas.

In an attempt to compensate for the increased adhesivity of the serum starved cells, we tested a range of PLL-g-PEG concentrations to see if higher concentrations of the anti-fouling coating agent could prevent serum-starved cells from non-specifically adhering to the substrate. Three different concentrations of PEGs were passivated at 0,

100, and 1000 µg/mL, and each of those PEG layers were seeded with either serum-starved or serum-exposed cells. Regardless of PEG concentration, the serum-exposed cells were unable to adhere to the surface while the serum-starved cells could adhere to the glass surface regardless of PEG concentration (**Fig. 9A**). Although the extent of how much the serum-starved cells spread qualitatively seemed to decrease as the PEG concentration increased, the ability to spread remained throughout.

Besides experimental conditions such as serum starvation, certain cell types were not amenable to micropatterning. For example, H1395 lung cancer cells were unable to even adhere to a glass substrate over the course of an hour when grown in DMEM media with 10% fetal bovine serum (**Fig. 10A**). When observed for 16 hours, the H1395 cells were still unable to adhere, proving to be a cell line that would not be ideal for micropatterning.

Another potential cell line of interest were MDA 453 breast cancer cells. These cells, when grown in DMEM with 10% fetal bovine serum, were passaged at extremely slow rates. When grown on micropatterns over the course of 6 days, the cells were still unable to adhere to the micropatterns, only displaying round phenotypes and growing in bunches (**Fig. 11A**). Not only would the cells be completely unaffected by the micropatterns, but they were not even able to produce a majority of single cells, which would not be conducive to the types of analysis of interest.

Discussion

Micropatterning can be a powerful technique for isolating adherent cells and testing how geometric idiosyncrasies in the substrate can affect cellular morphologies. Cells grown on unbound substrates present many challenges for quantitative analysis, including moving in and out of frame, overlapping with neighboring cells, and lacking a common frame of reference for analysis (**Fig. 2**). Micropatterning circumvents this issue by providing adhesive islands for individual cells, fixing them in place for long time course observations and preventing them from overlapping with different cells. The micropattern itself can also be a frame of reference for analysis, such as providing a center point, or in the case of the circular harmonic patterns (**Fig. 1**), several lobes from which deviations in distance and shape in the form of cellular extensions can be measured. We were able to optimize several aspects of the micropatterning process, including the Z-axis position of UV illumination (**Fig. 3**), the intensity of UV light (**Fig. 4**), the concentration of fibronectin, the cell seeding density, and the size of micropatterns (**Fig. 5**). Although the protocol was optimized for 3T3 cells, it was also found that some experimental conditions and other types of cells were not amenable to micropatterning and future analysis efforts.

Keeping in mind the kinds of chemical gradients present in *in vivo* environments, a 0% serum condition was attempted. As a result, cells grown in 0% serum DMEM media for 24 hours indiscriminately adhered to both micropatterns and the PLL-g-PEG surface, obviating any kind of advantages that micropatterning as a technique engenders under normal circumstances (**Fig. 8**, **Fig. 9**). The opposite issue arose with cell lines such as H1395 lung cancer cells (**Fig. 10**) and MDA MB 453 breast cancer

cells (**Fig. 11**), which both struggled to adhere to glass substrates, let alone the micropatterns themselves. Without the ability to adhere to the micropatterns in a timely manner, they were unable to be isolated for observation and for future analysis.

For cells, such as 3T3 mouse fibroblast cells, that are able to selectively adhere to the micropatterns, micropatterning is an effective technique for isolating single cells for long periods of observation. Future efforts using micropatterning will have to involve some preliminary evaluations to test the adherence capabilities and selectivity of adherence of any cell line of interest. Cells that either fail to adhere at all or do not selectively adhere to the micropattern and instead also bind to the passivated antifouling coating agent fail as ideal candidates for micropatterning assays. Moving forward, we identified cells that passed these qualifications and subjected them to an image analysis pipeline that tracked their morphological dynamics.

Experimental Procedures

Cell culture

3T3 mouse fibroblast cells (ATCC CRL-1658) were cultured in Dulbecco's Modified Eagle's Medium (DMEM) (Sigma-Aldrich D6429) with 10% fortified calf bovine serum (Cytiva Life Sciences SH30396.03) and 1% penicillin-streptomycin (ThermoFisher 15140122). Cells were grown in a 5% CO_2 incubator at 37ºC up to 90% confluence before being washed and passaged. Adherent cells were washed with PBS at each passage and detached from the flask surface by incubating with TrypLE (ThermoFisher Scientific 12604021) for 5-10 minutes at 37ºC. TrypLE was quenched with fresh DMEM media, and cells were resuspended and plated into new flasks with fresh DMEM. The following cancer cell lines were all cultured in DMEM with 10% fetal bovine serum (Fisher Scientific SH30396.03) and 1% penicillin-streptomycin in a 5% CO_2 atmosphere at 37ºC: MDA-MB-453 (ATCC HTB-131) and H1395 (CRL-5868).

Cell cytoskeleton and nuclei staining

Cell cytoskeleton and nuclei were visualized using the Actin Cytoskeleton and Focal Adhesion Staining Kit (Sigma-Aldrich FAK100). Cells were fixed with 4% paraformaldehyde, then washed with buffer. After permeabilizing with 0.1% Triton X-100, the cells were washed twice and applied with blocking solution. Anti-Vinculin was diluted and incubated before being subjected to several wash steps. Cells were subjected to secondary antibody with TRITC-conjugated Phalloidin. With three additional wash steps, the cells were ready for final incubation with DAPI for nuclei visualization.

Micropatterning

We employed the light-induced molecular adsorption (LIMAP) method for micropatterning (Strale et al., 2016). 35mm Glass bottom petri dishes (MatTek P35G-1.5-20-C) were exposed with oxygen plasma in preparation for passivation. For adsorption of the anti-fouling coating agent, 0.1 mg ml^{-1} PLL(20)-g[3.5]-PEG(2) (SuSoS CHF9,600.00) solution was added for 1 hour. The dish was washed five times with Milli-Q purified water. A 1:5 ratio of PLPP photoinitator gel to 70% ethanol (Alveole) was added to the microwell and dried at room temperature for 1 hour. To create the micropatterns, the well was exposed to UV light at a dosage of 30mJ mm^{-2}, and excess gel was washed away with 5 Milli-Q purified water washes and 5 Dulbecco's Phosphate Buffered Saline (DPBS) solution (VWR L0119-0500) washes, with the last volume of DPBS left to incubate for 5 minutes to rehydrate the substrate. The wells were then incubated with 10µg ml^{-1} fibronectin (Sigma-Aldrich F1141-5MG) and 10µg ml^{-1} NeutrAvidin (Invitrogen 84607) for five minutes and then washed 5 times with DPBS. PEGs were added at 0.1 mg ml^{-1} for another 1 hour incubation before being finally washed with water for 5 times.

Lentiviral transduction

To produce pantropic VSV-G pseudotyped lentivirus, 293T cells (ATCC CRL-3216) were transfected with a pLV-EF1a-IRES transgene expression vector, along with viral packaging plasmids pMD2.G and psPAX2 using Fugene HD (Promega #E2312). Virus-producing cells were grown in 6-well tissue culture treated plates (Corning 3335). Once 72 hours had passed, the viral supernatant was collected, filtered through a 0.45µM PES syringe filter, and added to 3T3 mouse fibroblast cells for transduction

using a 2µg/mL Polybrene transfection reagent (Sigma TR-1003-G). After 24 hours of exposure, the cells were subjected to antibiotic selection using puromycin. Surviving cells were assessed with fluorescence microscopy for successful transduction of the LifeAct-GFP reporter.

Fluorescence imaging

Cells under observation were loaded onto either glass bottom plates (Cellvis P06-1.5H-N) or 35mm Glass bottom petri dishes (MatTek P35G-1.5-20-C). After an hour of incubation for cells to adhere, they were imaged on a Nikon Ti-Eclipse while incubated in a Tokai Stage Top Incubator maintaining a temperature of 37ºC and an atmosphere of 5% CO2.

Figures

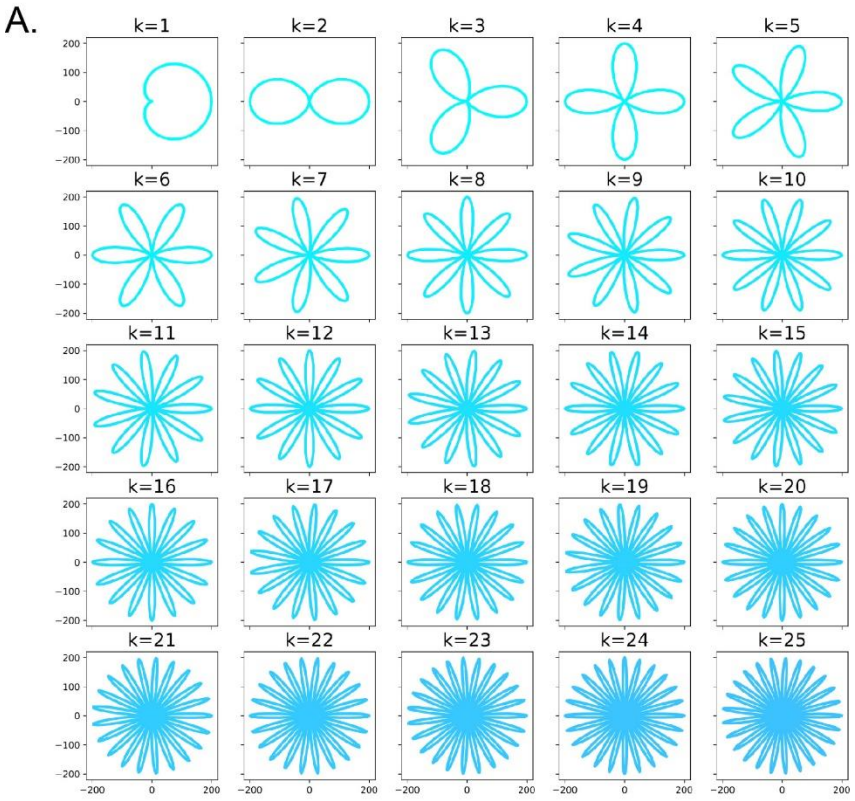
A.
k=1
k=2
k=3
k=4
k=5
k=6
k=7
k=8
k=9
k=10
k=11
k=12
k=13
k=14
k=15
k=16
k=17
k=18
k=19
k=20
k=21
k=22
k=23
k=24
k=25

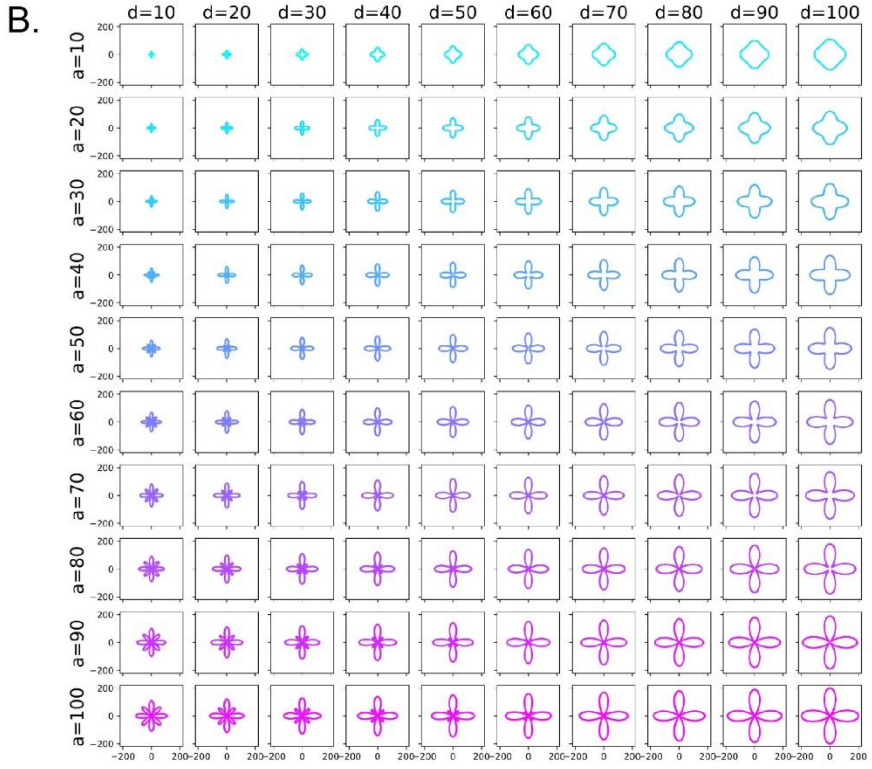
B.
d=10
d=20
d=30
d=40
d=50
d=60
d=70
d=80
d=90
d=100
a=10
a=20
a=30
a=40
a=50
a=60
a=70
a=80
a=90
a=100

Figure 1: Circular harmonics provide a tunable set of geometries to systematically assess size and spatial complexity.

A) Changing the ‘k’ parameter in Eq. 1 modulates the spatial complexity of the geometric patterns by changing the number of petals radiating out from the center point. Values k = 1 through k = 25 displayed. The y- and x-axes represent size on Cartesian coordinates. B) Changing the ‘a’ and ‘d’ parameters (Eq. 1) concurrently will increase the size of the geometric pattern. Values from a = 10 through a = 100 are iteratively applied to values d = 10 through d = 100.

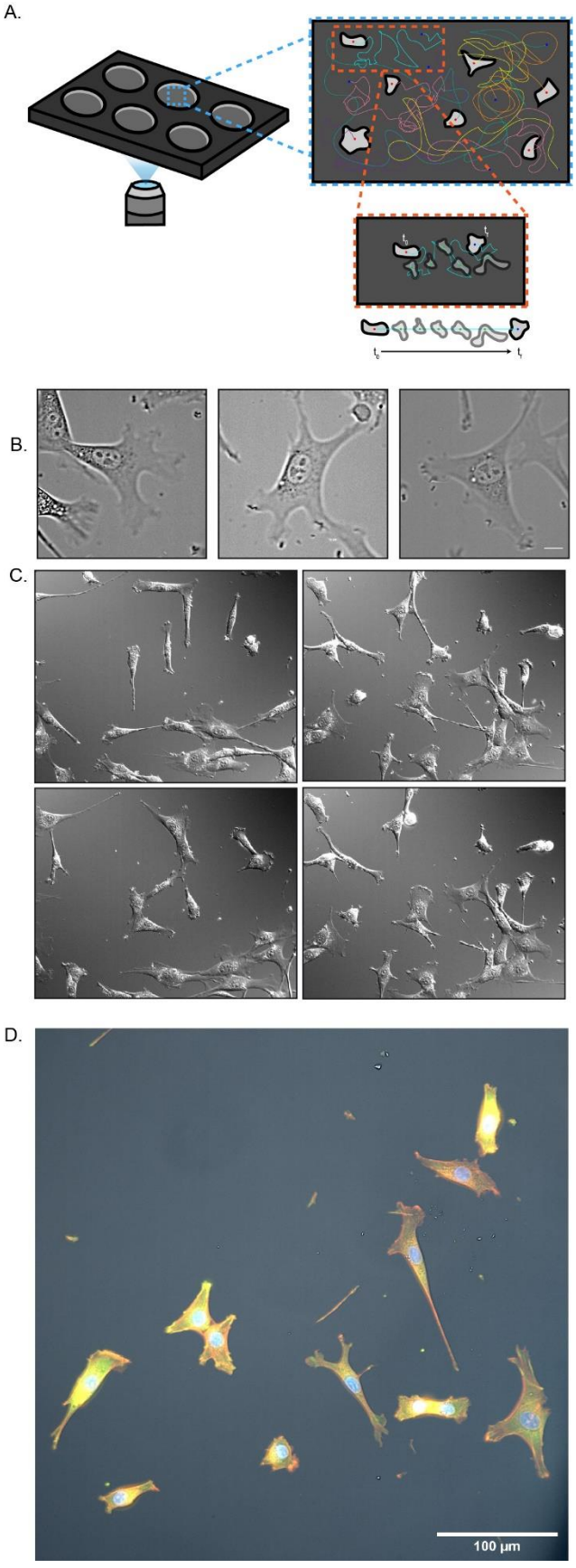
A.
B.
C.
D.
100 µm

Figure 2: 3T3 Cells on unbounded glass substrate

A) Schematic depicting cells on unbound substrates resulting in heterogeneous shapes over time B) Brightfield images of 3T3 mouse fibroblast cells displaying varied geometries C) DIC images of 3T3 mouse fibroblast cells on unbounded glass substrate D) Fluorescence microscopy images of 3T3 mouse fibroblast cells actin cytoskeleton and focal adhesions. TRITC-conjugated phalloidin was bound to F-actin, DAPI revealed nuclei with counterstaining, and anti-Vinculin monoclonal antibodies were used to locate focal contacts.

A.

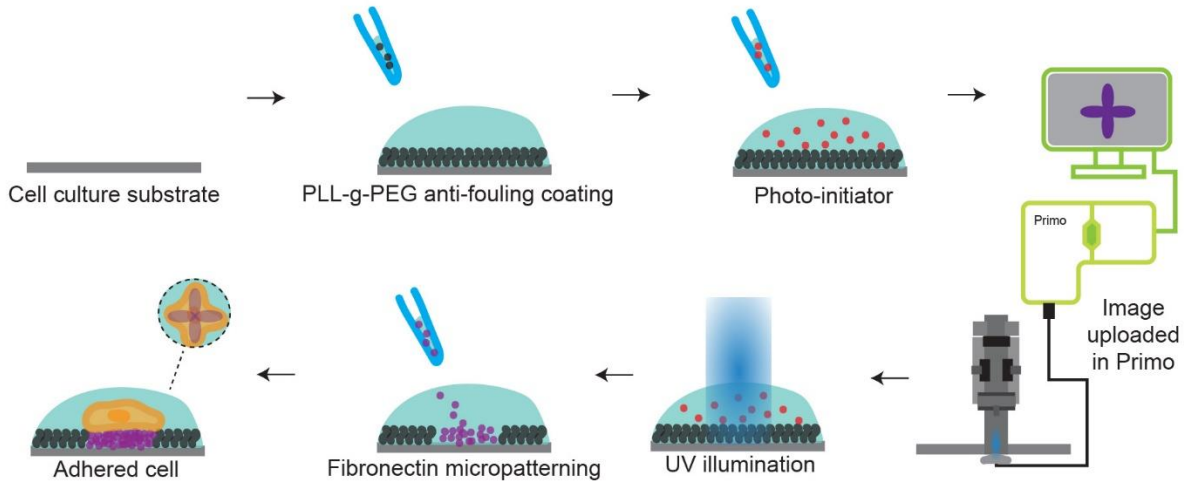
Cell culture substrate
PLL-g-PEG anti-fouling coating
Photo-initiator
Primo
Image uploaded in Primo
UV illumination
Fibronectin micropatterning
Adhered cell

B.

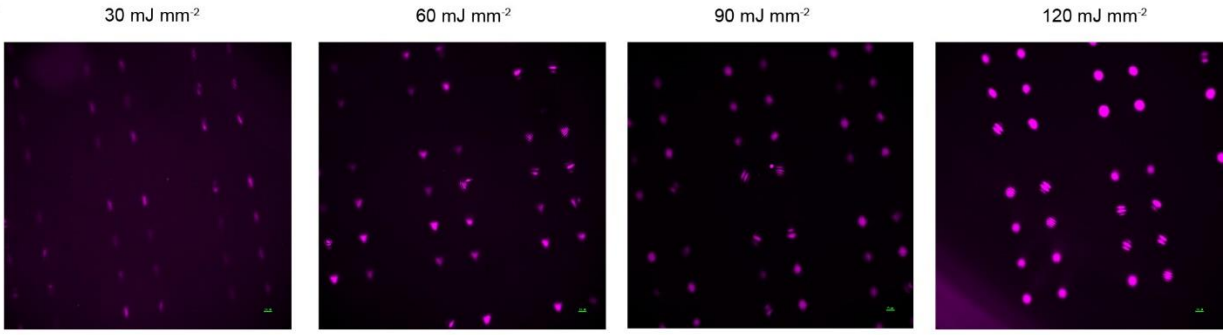
30 mJ mm-2
60 mJ mm-2
90 mJ mm-2
120 mJ mm-2

C.

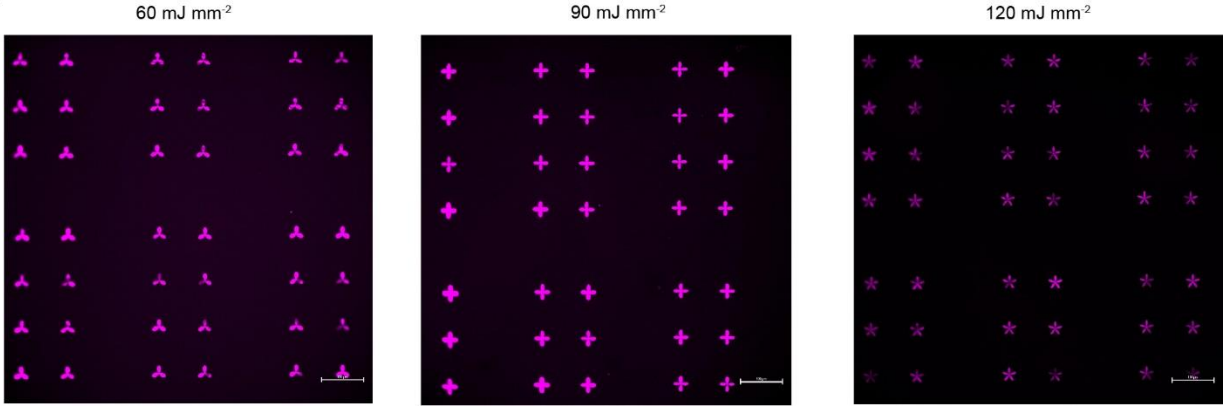
60 mJ mm-2
90 mJ mm-2
120 mJ mm-2

Figure 3: Micropatterning workflow using varying UV dosages

A) Schematic of workflow to generate micropatterns for cells to adhere to. B) Range of UV dosages to create micropatterns with Z-axis offset. C) Range of UV dosages to create micropatterns without any Z-axis offset.

A.

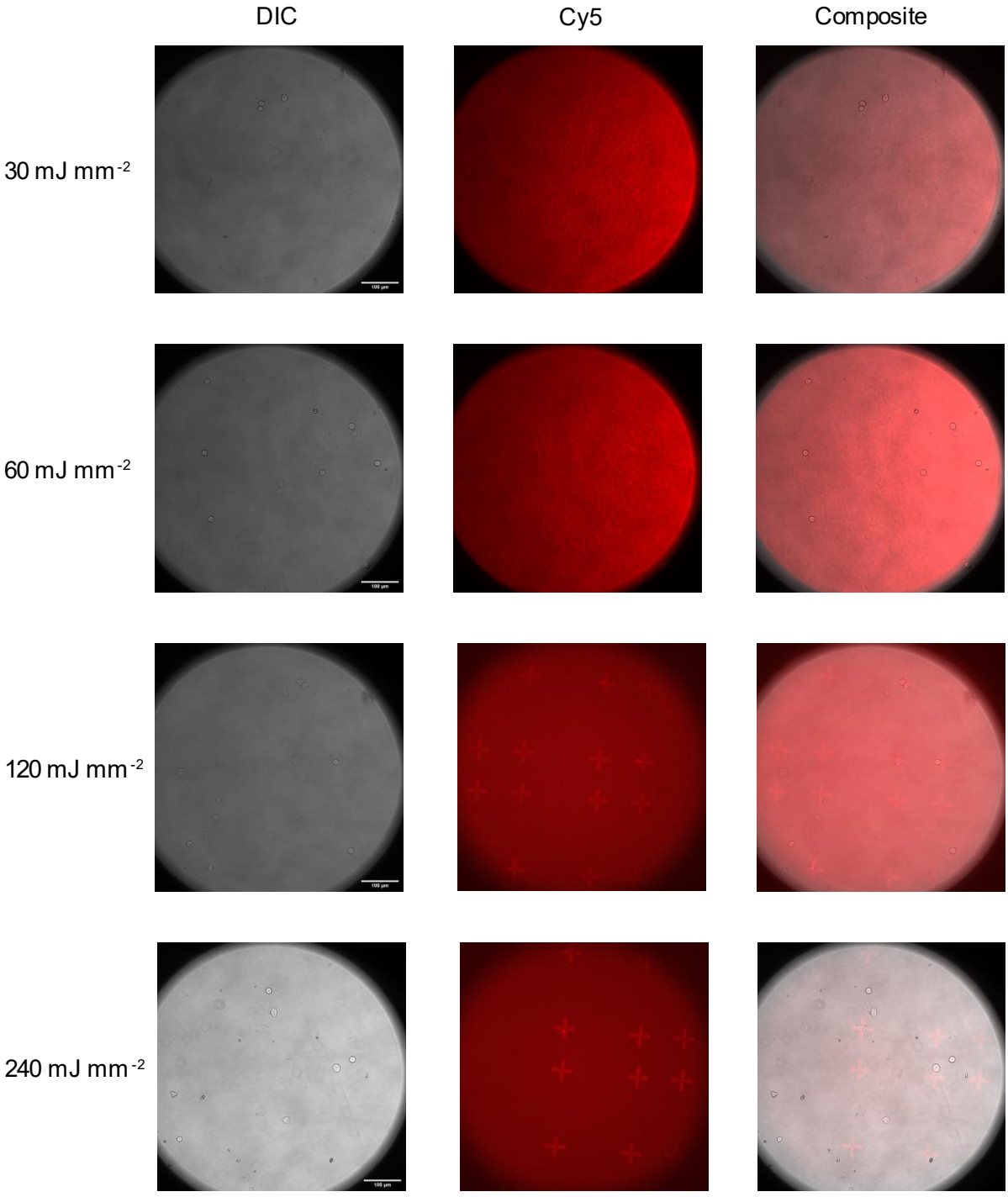

Figure 4: Titrating UV dosage on PLPP photoinitiator for creating micropatterns

A) A range of UV dosages from 30mJ mm^{-2} to 240 mJ mm^{-2} were used with the PRIMO device to ablate the PEG layer.

A.

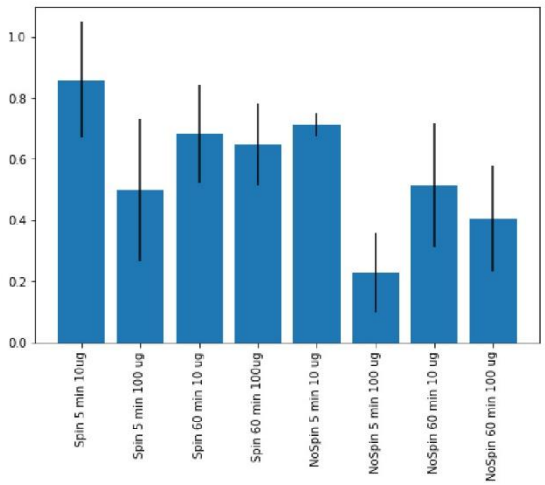
1.0
0.8
0.6
0.4
0.2
0.0
Spin 5 min 10ug
Spin 5 min 100 ug
Spin 60 min 10 ug
Spin 60 min 100ug
NoSpin 5 min 10 ug
NoSpin 5 min 100 ug
NoSpin 60 min 10 ug
NoSpin 60 min 100 ug

B.

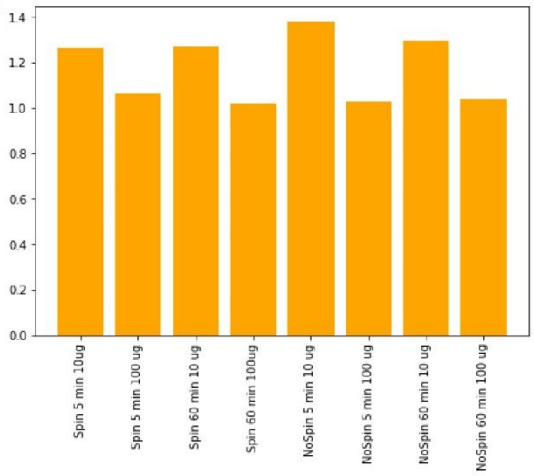
1.4
1.2
1.0
0.8
0.6
0.4
0.2
0.0
Spin 5 min 10ug
Spin 5 min 100 ug
Spin 60 min 10 ug
Spin 60 min 100ug
NoSpin 5 min 10 ug
NoSpin 5 min 100 ug
NoSpin 60 min 10 ug
NoSpin 60 min 100 ug

C.

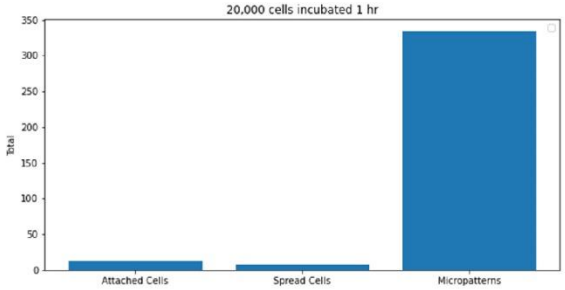
20,000 cells incubated 1 hr
Total
350
300
250
200
150
100
50
0
Attached Cells
Spread Cells
Micropatterns

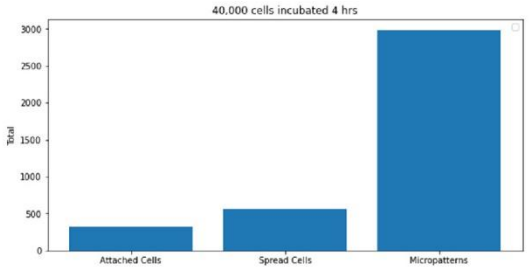
40,000 cells incubated 4 hrs
Total
3000
2500
2000
1500
1000
500
0
Attached Cells
Spread Cells
Micropatterns

D.

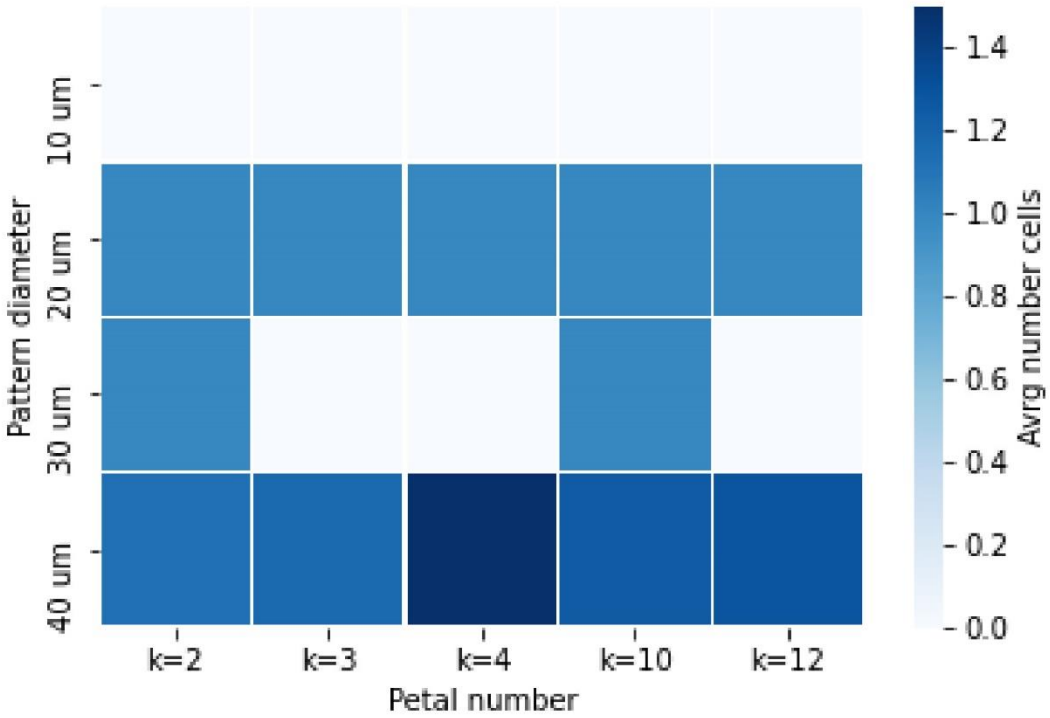
Pattern diameter
10 um
20 um
30 um
40 um
k=2
k=3
k=4
k=10
k=12
Petal number
Avrg number cells
1.4
1.2
1.0
0.8
0.6
0.4
0.2
0.0

Figure 5: Optimizing parameters for the micropatterning assay:

A) 3T3 adherence ratio for cells based on spin preparation of fibronectin. B) Fluorescence signal-to-noise ratio for cells based on spin preparation of fibronectin. C) Count of attached vs spread cells on micropatterns after seeding 3T3 cells in a 35 mm dish with different population sizes. D) Assessing cell occupancy based on a screen of petal number and micropattern size.

A.

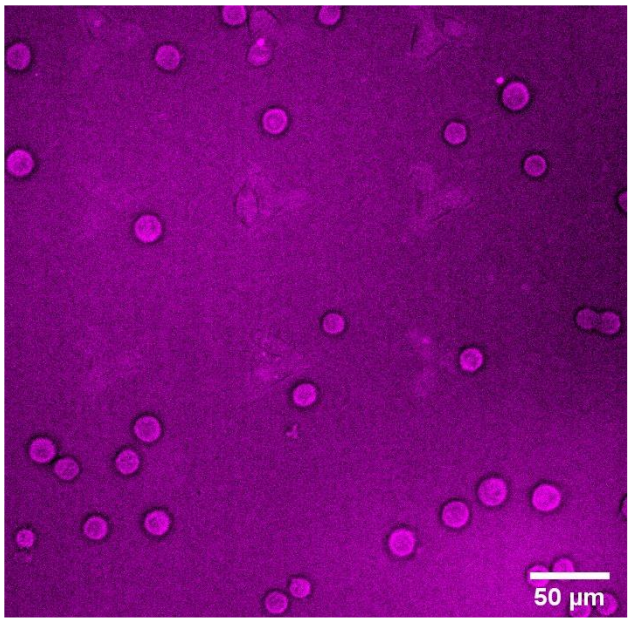

B.

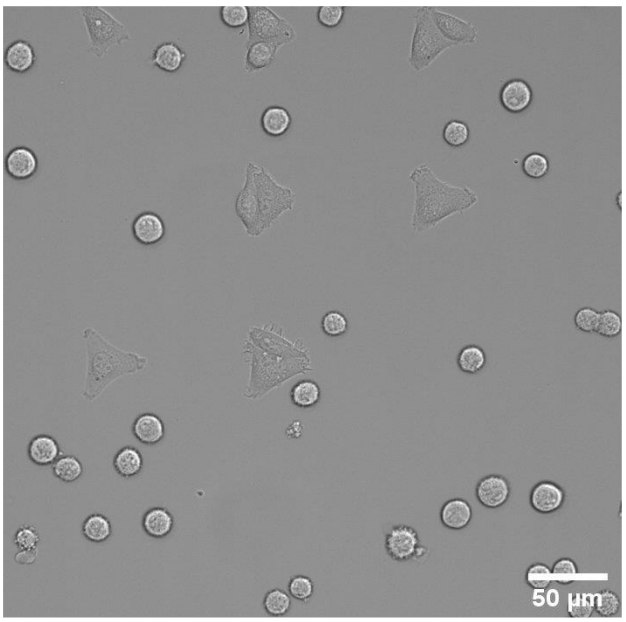

Figure 6: Overseeding micropatterns results in multiple cell adherence.

A) Fluorescence microscopy image of Neutravidin Cy5 fibronectin micropatterns with k3 spatial complexity. B) DIC image of 3T3 mouse fibroblast cells on micropatterns and PEG passivated substrate.

A.

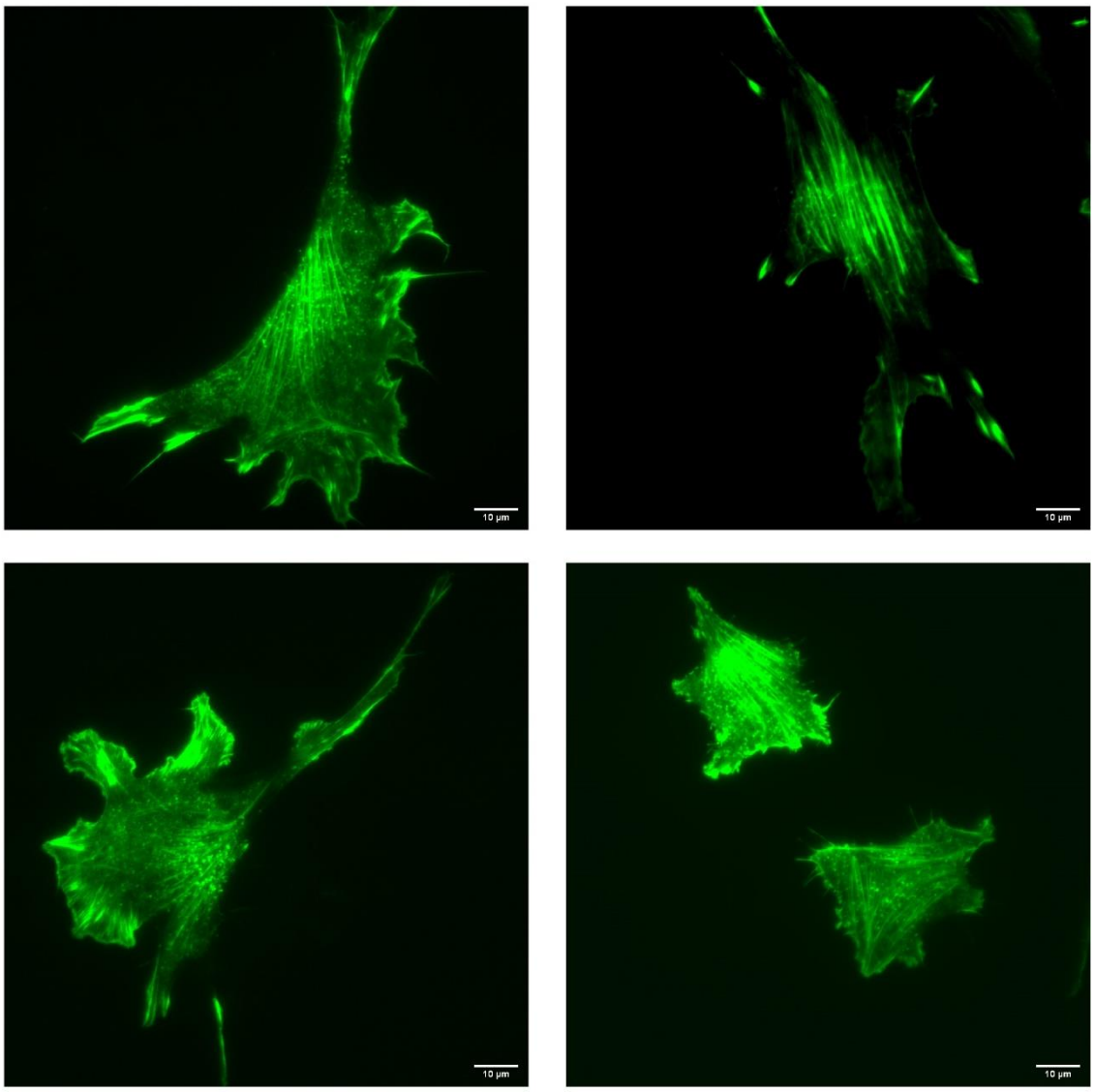

B.

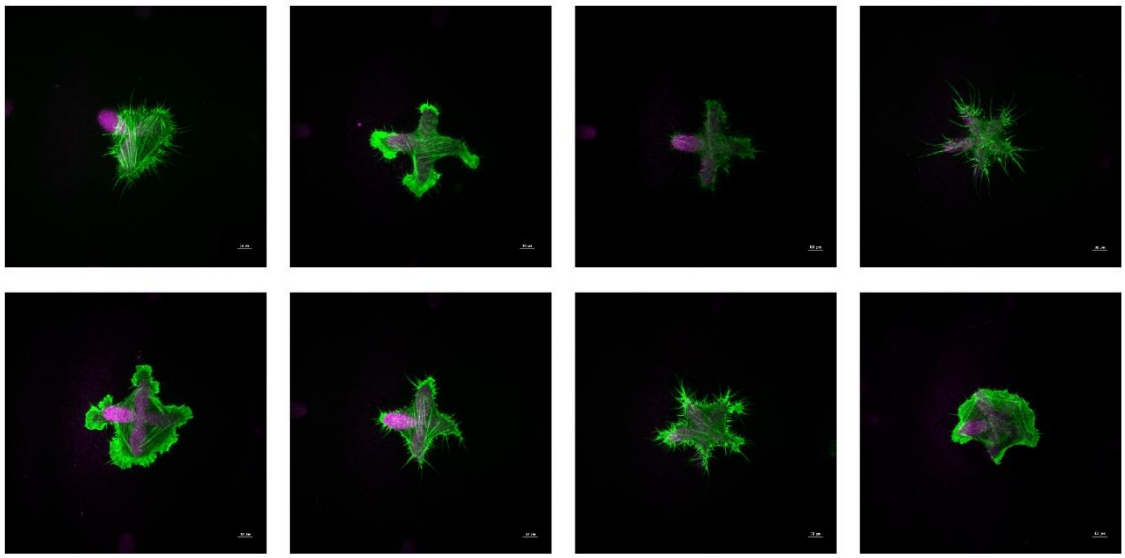

Figure 7: Fluorescence microscopy images of LifeAct-GFP reporter in 3T3 cells

A) LifeAct-GFP 3T3 cells on unbound glass substrate. B) LifeAct-GFP 3T3 cells on fibronectin-NeutrAvidin micropatterns.

A.

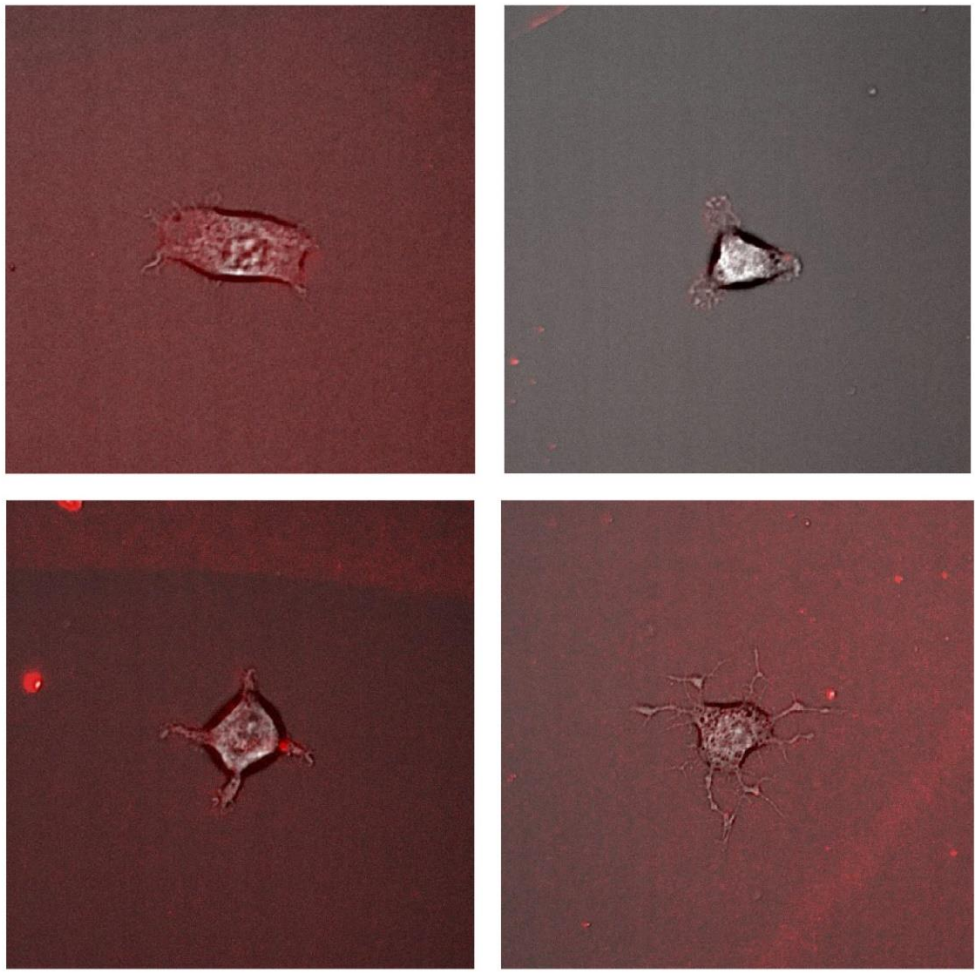

B.

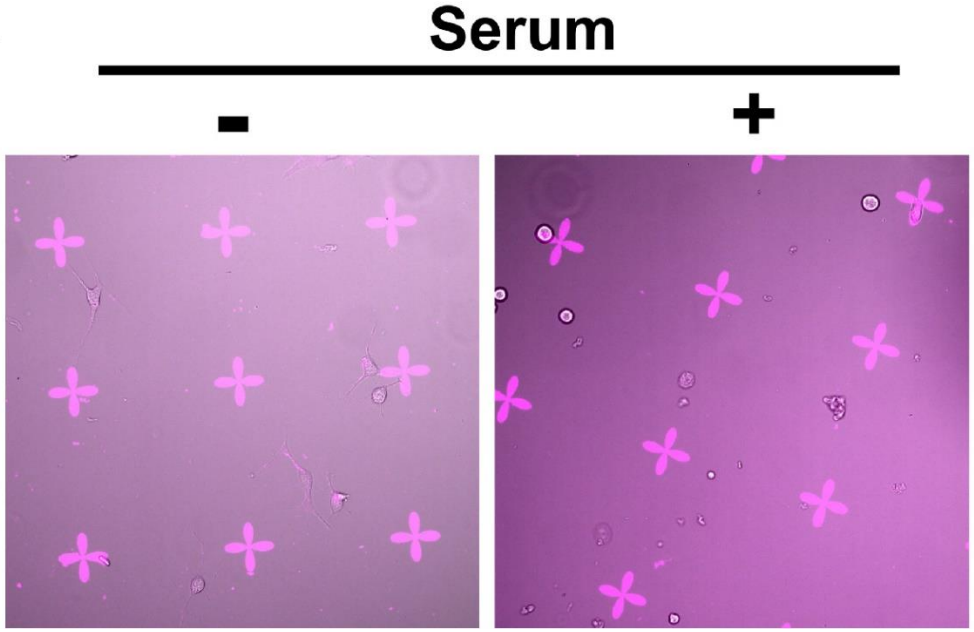

Figure 8: 3T3 cells grown on micropatterns without serum in media

A) 3T3 cells grown on k2, 3, and 4 fibronectin-NeutrAvidin micropatterns. B) 3T3 cells grown on k4 fibronectin-NeutrAvidin micropatterns either with CS present or absent in DMEM media.

A.

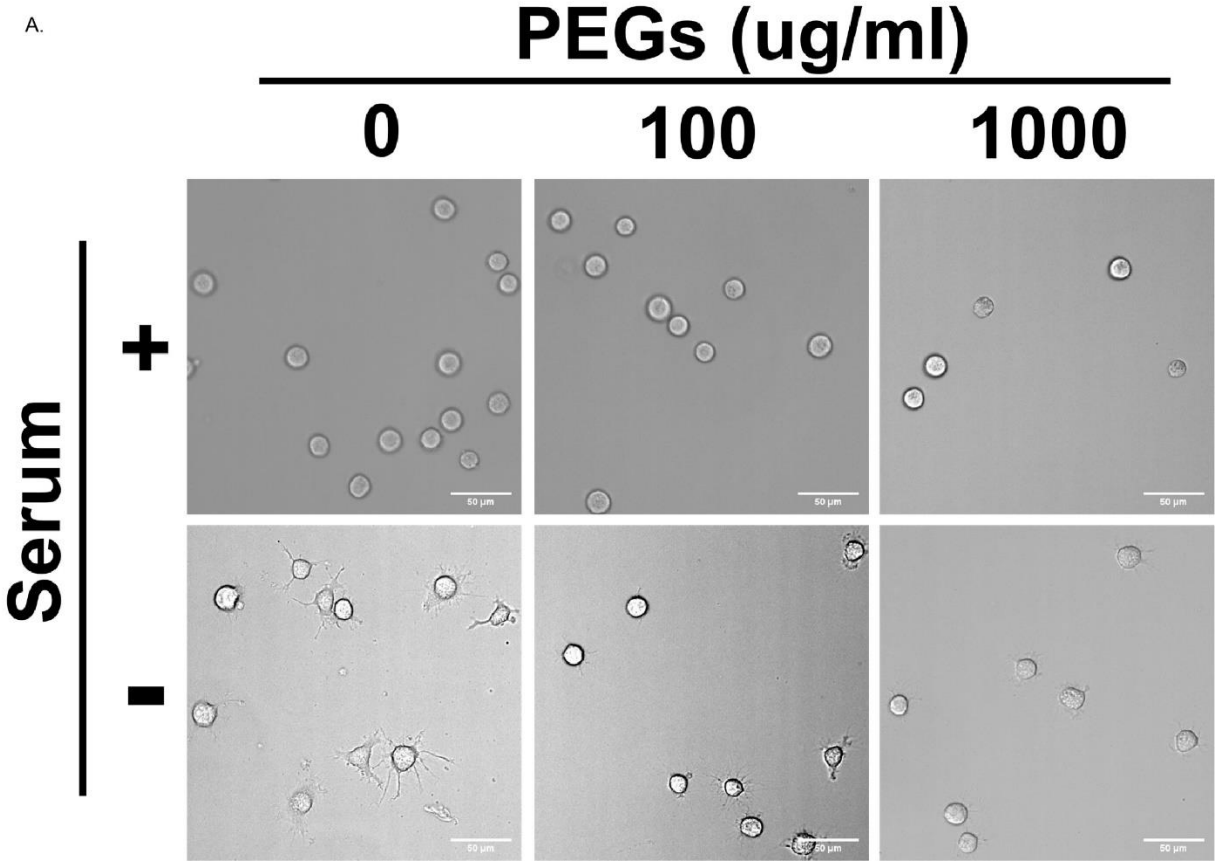

Figure 9: 3T3 Cells grown on PEG-passivated substrate with or without serum

A) 3T3 cells were grown on increasing concentrations of PLL-g-PEG passivated glass substrate from 0 to 1000μg/ml. Cells were either grown with or without 10% calf serum in DMEM media.

A.

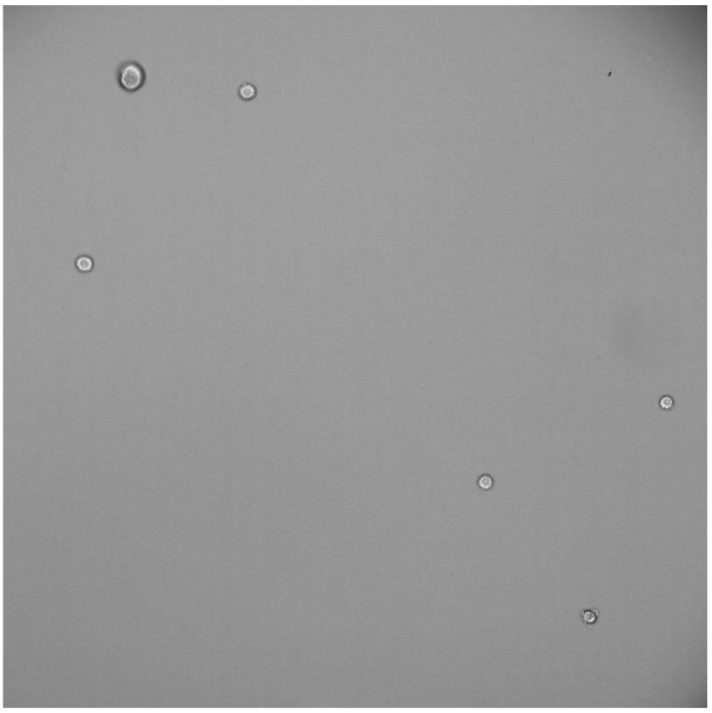

B.

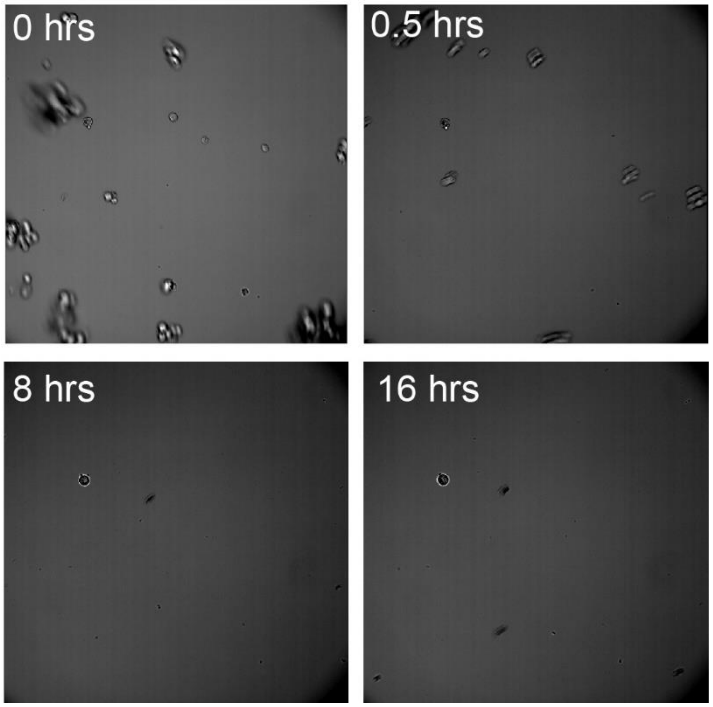

Figure 10: H1395 lung cancer cells grown on glass substrates

A) H1395 incubated on glass substrate for 1 hour in DMEM media with 10% fetal bovine serum and 1% penicillin/streptomycin. B) H1395 grown in the same conditions with timepoints taken at four different intervals.

A.

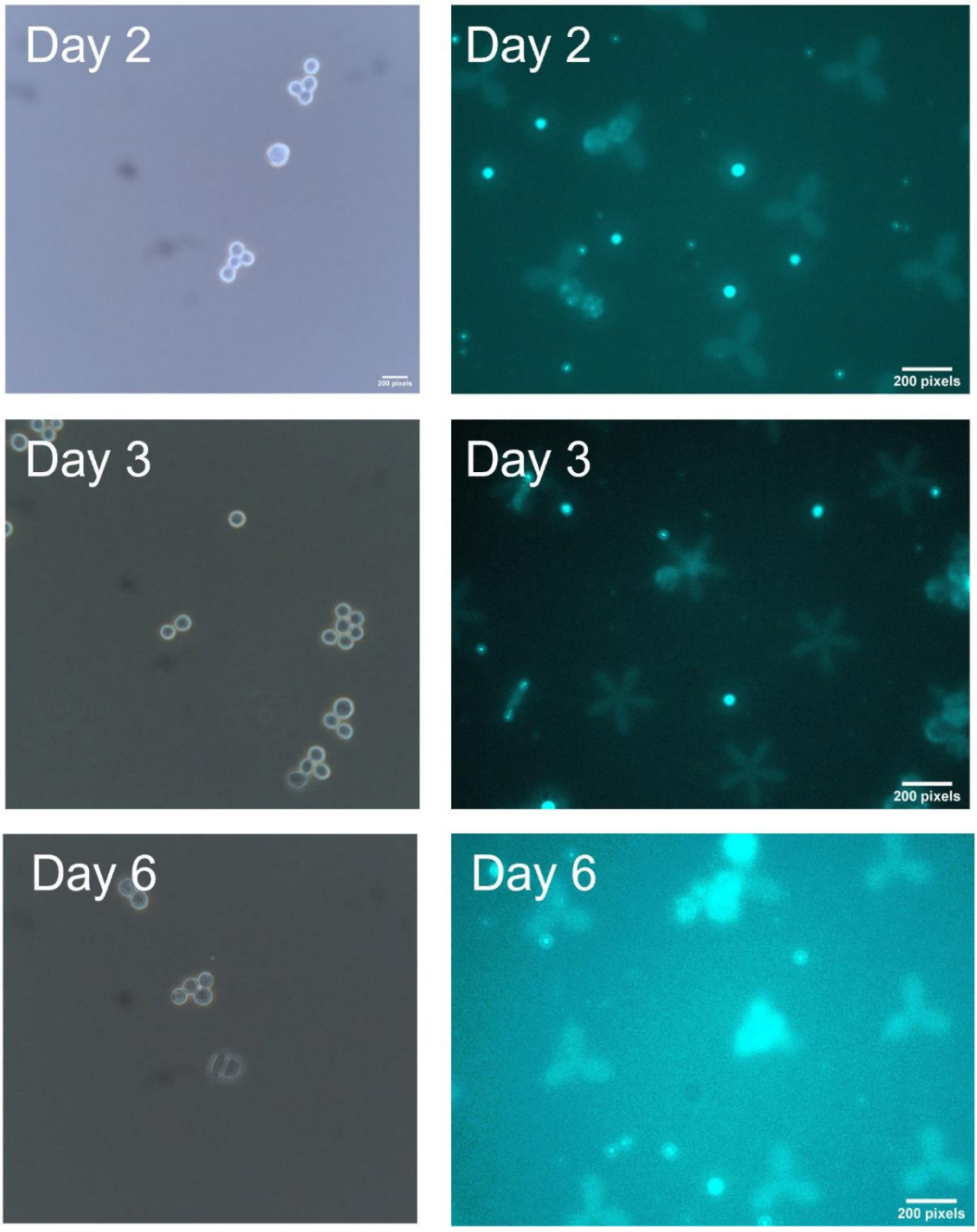
Day 2
Day 2
200 pixels
Day 3
Day 3
200 pixels
Day 6
Day 6
200 pixels

Figure 11: MDA 453 breast cancer cells grown on micropatterns

A) MDA 453 breast cancer cells grown in DMEM media with 10% fetal bovine serum and 1% penicillin/streptomycin over the course of 6 days on fibronectin-Neutravidin micropatterns.

References

Alvarez, Y., & Smutny, M. (2022). Emerging Role of Mechanical Forces in Cell Fate Acquisition. *Frontiers in Cell and Developmental Biology*, *10*(May), 1–7. https://doi.org/10.3389/fcell.2022.864522

Gonzalez-Molina, J., Mendonça da Silva, J., Fuller, B., & Selden, C. (2019). The extracellular fluid macromolecular composition differentially affects cell-substrate adhesion and cell morphology. *Scientific Reports*, *9*(1), 1–12. https://doi.org/10.1038/s41598-019-44960-3

Malek, A. M., & Izumo, S. (1996). Mechanism of endothelial cell shape change and cytoskeletal remodeling in response to fluid shear stress. *Journal of Cell Science*, *109*(4), 713–726. https://doi.org/10.1242/jcs.109.4.713

Miller, D. J., Bhaduri, A., Sestan, N., & Kriegstein, A. (2019). Shared and derived features of cellular diversity in the human cerebral cortex. *Current Opinion in Neurobiology*, *56*, 117–124. https://doi.org/10.1016/j.conb.2018.12.005

Plikus, M. V., Wang, X., Sinha, S., Forte, E., Thompson, S. M., Herzog, E. L., Driskell, R. R., Rosenthal, N., Biernaskie, J., & Horsley, V. (2021). Fibroblasts: origins, definitions, and functions in health and disease. *Cell*, *184*(15), 3852–3872. https://doi.org/10.1016/j.cell.2021.06.024.Fibroblasts

Rahimi, A. M., Cai, M., & Hoyer-Fender, S. (2022). Heterogeneity of the NIH3T3 Fibroblast Cell Line. *Cells*, *11*(17). https://doi.org/10.3390/cells11172677

Riedl, J., Crevenna, A. H., Kessenbrock, K., Yu, J. H., Neukirchen, D., Bista, M.,

Bradke, F., Jenne, D., Holak, T. A., Werb, Z., Sixt, M., & Wedlich-Soldner, R. (2008). Lifeact: a versatile marker to visualize F-actin. *Nat Methods*, *5*(7), 605. https://doi.org/10.1038/nmeth.1220.Lifeact

Strale, P. O., Azioune, A., Bugnicourt, G., Lecomte, Y., Chahid, M., & Studer, V. (2016). Multiprotein Printing by Light-Induced Molecular Adsorption. *Advanced Materials*, *28*(10), 2024–2029. https://doi.org/10.1002/adma.201504154